FUSION ENERGY SCIENCE
JOINT FACILITIES AND THEORY RESEARCH
TARGET 2011

Final Report for the period
October 1, 2010 through September 30, 2011

by
PROJECT STAFF

Prepared for the
U.S. Department of Energy

DATE PUBLISHED: OCTOBER 2011

DISCLAIMER

FUSION ENERGY SCIENCE
JOINT FACILITIES AND THEORY RESEARCH
TARGET 2011

Final Report for the period
October 1, 2010 through September 30, 2011

by
PROJECT STAFF

Prepared for the
U.S. Department of Energy

DATE PUBLISHED: OCTOBER 2011

FUSION ENERGY SCIENCE JOINT FACILITIES AND THEORY RESEARCH TARGET 2011

R.J. Groebner, C.S. Chang, P.H. Diamond, J.W. Hughes, R. Maingi, P.B. Snyder, X.Q. Xu

Research Contributors:

GA: E.A. Belli, B.D. Bray, J. Candy, T.M. Deterly, N.M. Ferraro, R.J. Groebner, J.E. Kinsey, A.W. Leonard, C. Liu, T.H Osborne, D.M. Ponce, R. Prater, S.P. Smith, P. B. Snyder, G.M. Staebler, R.E. Waltz

Georgia Tech: W.M. Stacey

LLNL: M.E. Fenstermacher, I. Joseph, C.J. Lasnier, M.V. Umansky, E. Wang, X. Xu

Lodestar: D.A. Baver, D.A. D'Ippolito, J.R. Myra, D.A. Russell

MIT: R.M. Churchill, I. Cziegler,[1] E. Davis, A.E. Hubbard, J.W. Hughes, B. LaBombard, B. Lipschultz, Y. Ma, J.C. Rost, L. Sugiyama, J.L. Terry, J. Walk, A.E. White, D.G. Whyte, S. Wolfe

ORNL: J. Canik, J.D. Lore, R. Maingi, A.C. Sontag

PPPL: D.P. Boyle, C.S. Chang, A. Diallo, S. Zweben

SNL: J.G. Watkins

Tech-X: A.Y. Pankin

U. Calif. Irvine: D. Fulton, Z. Lin

UCLA: E.J. Doyle, T.L. Rhodes, L. Schmitz, L. Zeng

UCSD: J.A. Boedo, P.H. Diamond, D. Eldon

U. Colo. Boulder: S.E. Parker, W. Wan

U. Toronto: J.D. Elder

U. Wisconsin: J.D. Callen, G.R. McKee, Z. Yan

[1]Currently at UCSD.

ANNUAL TARGET

Experiment:

Improve the understanding of the physics mechanisms responsible for the structure of the pedestal and compare with the predictive models described in the companion theory milestone. Perform experiments to test theoretical physics models in the pedestal region on multiple devices over a broad range of plasma parameters (e.g., collisionality, beta, and aspect ratio). Detailed measurements of the height and width of the pedestal will be performed augmented by measurements of the radial electric field. The evolution of these parameters during the discharge will be studied. Initial measurements of the turbulence in the pedestal region will also be performed to improve understanding of the relationship between edge turbulent transport and pedestal structure.

Theory:

A focused analytic theory and computational effort, including large-scale simulations, will be used to identify and quantify relevant physics mechanisms controlling the structure of the pedestal. The performance of future burning plasmas is strongly correlated with the pressure at the top of the edge transport barrier (or pedestal height). Predicting the pedestal height has proved challenging due to a wide and overlapping range of relevant spatiotemporal scales, geometrical complexity, and a variety of potentially important physics mechanisms. Predictive models will be developed and key features of each model will be tested against observations, to clarify the relative importance of various physics mechanisms, and to make progress in developing a validated physics model for the pedestal height.

Quarter 4 Milestones

Complete experiments and simulations. Compare key features of relevant theoretical models against observations to clarify the relative importance of various physics mechanisms.

Submit a report documenting completion of these activities, which includes summary data, simulation results, implications for future work, and a brief, preliminary assessment of the implications for ITER.

Completion of 4th Quarter Milestone

The goals for this quarter have been achieved, as documented in the remaining sections of this report.

1. **Complete experiments and simulations:**
   a. During the 4th quarter, DIII-D successfully completed all planned pedestal experiments for FY11.
   b. C-Mod and NSTX have successfully completed all planned pedestal experiments earlier in the fiscal year.
   c. Simulations have been completed with a number of numerical codes, including BOUT++, EPED, XGC0, ELITE, M3D-C1, NEO, SOLPS, GYRO, GEM, GTC, FACETS, SOLT and 2DX.
   d. Model-experiment comparisons have also been performed for two analytic models: one based on paleoclassical transport and one on a solution of the first four moments of the Boltzman transport equation.

2. ***Compare key features of relevant theoretical models against observations to clarify the relative importance of various physics mechanisms:*** Such comparisons have been performed for several physics mechanisms, including neoclassical transport, paleoclassical transport, electron temperature gradient modes, kinetic ballooning modes, neutral fueling, peeling-ballooning stability and others. An overview of this work is provided in the executive summary and more detail is provided in the research contributions.
3. ***Submit a report documenting completion of these activities, which includes summary data, simulation results, implications for future work, and a brief, preliminary assessment of the implications for ITER:*** This report documents the completion of these activities. Summary data and simulation results are shown in the research contributions to the report. Additional detail can be found in the bibliographies and references that accompany several of these contributions. Implications for future work and a brief summary of the implications for ITER are presented in the executive summary.

EXECUTIVE SUMMARY

Briefly stated, the goal of this combined experiment/theory milestone was to improve our knowledge of the physics processes that control the H-mode pedestal by applying models of these mechanisms to experimental data. A concerted and coordinated effort of experimental, theory and modeling activities has examined several physics mechanisms of interest and has met the goals of the milestone. A few noteworthy results will be noted here. The activity has applied peeling-ballooning theory to all three machines and increased confidence that the theory predicts the ultimate limits to pedestal height in an ELMing plasma. The activity has expanded the range of conditions for testing of the EPED model and increased confidence in the ability of the model to compute the pedestal pressure height in medium aspect ratio tokamaks. Kinetic neoclassical models have been used to verify that an important analytic model for the pedestal bootstrap current has good accuracy in many regimes of interest but needs correction at high collisionality. A benchmarking effort between electromagnetic gyrokinetic codes has provided increased understanding of how to use these codes in the pedestal and has laid the groundwork for using these codes to study linear stability of gyrokinetic modes in and on top of the pedestal. Comparisons of data and models have led to successful simulations of a quasi-coherent mode in C-Mod and to the tentative identification of a high frequency mode in DIII-D. A kinetic neoclassical model qualitatively agrees with some features of pedestal density profiles. A paleoclassical transport model quantitatively predicts some features of the electron temperature profiles in NSTX and DIII-D.

The milestone activity also laid the groundwork for future advancements in understanding and predicting the pedestal. All three machines obtained a wealth of pedestal data under a wide variety of operating conditions. Some of these data have been analyzed already and the analysis and comparison with models will provide important results over the next year or two. Many codes were improved in significant ways in order to model data under the challenging conditions of the pedestal. In addition, new and strengthened collaborations were established between experiment, modeling and theory, and these efforts include providing mechanisms for sharing experimental data. All of these efforts will continue to provide major benefits to future pedestal studies.

Much of the experimental and modeling work performed to support this milestone is reported in detail in the research contributions to this report. Here, a summary of results from the various contributions, as they pertain to several proposed pedestal physics processes, is discussed here. Emphasis is placed on mechanisms for which there are results from one or more machines or one or more models. Work from preceding quarterly reports is used for some of this summary. At the end of this summary, a brief summary of implications for ITER and implications for future work will be presented.

Overview of results for physics processes

- **Neoclassical Transport:** The XGC0 code has been used to examine the combined effect of neoclassical transport and neutral fueling on the density pedestal. The code qualitatively reproduces several features of the experiments, including the steep density gradients observed in the H-mode pedestal. Quantitative comparisons to data from C-Mod and DIII-D show that neoclassical transport by itself produces density pedestals that are narrower than observed. Thus,

some anomalous particle transport is required in addition to neoclassical transport to explain the observations.

- **Paleoclassical Transport:** An analytic model for paleoclassical transport in the pedestal exists and has been used to predict features of pedestal electron temperature and density profiles in NSTX and DIII-D. The model has made good predictions of the electron thermal diffusivity and the shape of the pedestal density profile in NSTX discharges with significant lithium injection. In a range of discharges in DIII-D, the ratio of predicted pedestal electron temperature gradient to observed gradient is 1.62 ± 0.81. Thus, for some of the data, the model predicts the minimum observed electron thermal diffusivity. In other cases, additional electron thermal transport must be invoked to explain the results. The model predicts densities that are typically about 2 times larger than observed in DIII-D. Thus, some additional particle transport must be invoked to explain the observations.
- **Electron Temperature Gradient (ETG) Modes:** Short scale turbulence due to electron temperature gradient modes has been proposed both as a process to drive electron thermal transport in the steep gradient region of the pedestal and on top of the pedestal. There are qualitative and quantitative observations that have features expected for ETG modes. For instance, the ratio of the electron density scale length to the electron temperature scale length (η_e) in the pedestal has been observed in all three machines to be of a magnitude that is expected to drive ETG modes. In addition, short wavelength fluctuations, in a range expected for ETG modes, have been observed at the edge of both NSTX and DIII-D. Finally, a number of ETG models have been evaluated for DIII-D-like pedestal profiles and the models all predict significant electron thermal transport on the pedestal top. So far, though, there is no clear measurement of the amount of transport driven by ETG modes. Thus, they remain as candidates for important pedestal processes.
- **Peeling-Ballooning (PB) Stability:** Medium-n peeling ballooning modes are proposed as the MHD stabilities which cause Type I ELMs. Peeling-ballooning stability has been studied with BOUT++, ELITE and M3D-C1. The ELITE code, which treats PB modes in the ideal limit, has been applied to data from all three machines and it has provided a good description of the pedestal operating point achieved just before a Type I ELM. These and numerous other studies provide high confidence that the ideal peeling-ballooning theory provides a very good description of the ultimate pedestal limits in an ELMing H-mode discharge. There are some open issues. For one, the threshold condition for ELM onset in NSTX may be different than in C-Mod or DIII-D. This difference could be related to physics associated with the low aspect ratio of NSTX and this issue is under study. Another important issue is that the theory relies on knowledge of the edge current density, which has a large component due to bootstrap current in the pedestal. The bootstrap current is very difficult to measure directly and is routinely calculated from theory. This procedure gives reasonable results, but it is not known if this is always a good approximation. In addition, there are new results from XGC0 and NEO modeling, discussed below, suggesting that the standard theory is incorrect by 15-30% at high collisionality.

  Non-ideal modeling of linear peeling-ballooning eigenmodes and nonlinear ELM dynamics have been examined with both BOUT++ and M3D-C1. Calculations of diamagnetic stabilization of peeling-ballooning modes using BOUT++ and M3D-C1 find a significant stabilizing effect,

particularly at high-n. A model of this stabilization has been developed and implemented in routine peeling-ballooning stability analysis with ELITE, and in the EPED model. The BOUT++ peeling-ballooning ELM model has studied non-ideal effects, such as electron inertia and resistivity, in modeling of results from all three devices. Depending on the collisionality regime of a tokamak pedestal plasma, these calculations show that either collisionless (electron inertia) or resistive ballooning modes can be unstable at beta values below the threshold for the onset of peeling-ballooning modes. Thus, these modes might be responsible for H-mode turbulence transport when the pedestal is stable to peeling-ballooning modes.

- **Neoclassical Bootstrap Current:** XCG0 and NEO have been used to examine the accuracy of existing analytic formulas in calculating the pedestal bootstrap current. Calculations with XGC0 find that for pedestals in the banana-plateau collisionality regime, the analytic Sauter formula calculation of bootstrap current agrees well with the numerical calculations. However, when the pedestal electrons are in the collisional regime, the numerical simulation yields approximately 15-20% lower bootstrap current in a conventional tokamak, and approximately 30% higher bootstrap current in a tight aspect ratio tokamak. Calculations with NEO including the full linearized Fokker-Planck collision operator and a carbon impurity find small but significant (~10-20%) differences in the bootstrap current from that calculated in simplified models such as NCLASS or Sauter, and also note that the full collision operator is needed to accurately calculate the impurity and electron heat flux, as well as the main ion and impurity poloidal flow, particularly at high collisionality. The results from these codes may have implications for peeling-ballooning analysis in NSTX, which has been previously discussed. Existing peeling-ballooning calculations find that NSTX lies at the kink/peeling boundary but that the growth rates are low. If the pedestal bootstrap current was 20-30% higher than is calculated from the analytic theory, then the growth rates would be higher and a more unified theoretical understanding of ELM onset in low and medium aspect ratio devices might follow. Clearly, this is an important open issue.
- **Kinetic Ballooning Modes (KBM):** Long scale fluctuations due to kinetic ballooning modes have been proposed to limit the total pressure gradient in the pedestal. This pressure gradient is comparable to what would be predicted for infinite-n ideal ballooning modes (when not in the 2nd stable domain). A calculation of this gradient using ballooning theory has been used to develop a quantitative pedestal width model, which predicts that the pedestal width (average of the T_e and n_e widths) scales approximately as $(\beta_\theta^{ped})^{1/2}$, where β_θ^{ped} is the pedestal beta poloidal. This scaling is a good description of width scaling observed in systematic parameter scans in all three devices. The proposed KBM width scaling data is in reasonable (~20% or better) quantitative agreement with DIII-D and C-Mod. The observed width on NSTX also exhibits a $(\beta_\theta^{ped})^{1/2}$ dependence, but with a flux space width about 2.5 times wider than DIII-D or C-Mod. KBM calculations are highly challenging at low aspect ratio, and it remains under investigation whether the NSTX pressure gradient is limited by KBMs or another mechanism. Fluctuation measurements in DIII-D have shown that coherent modes exist in near QH-mode conditions and that these modes have characteristics expected for linear KBMs. These characteristics include propagation direction and frequency, poloidal mode number and decorrelation rate. If these modes were in fact KBMs, there are some important outstanding issues. Is the commonly observed long wavelength turbulence in

the pedestal due to turbulent KBMs and do KBMs drive sufficient transport to affect the pedestal structure?

- **EPED Model:** The EPED model combines calculated constraints from both KBM physics and PB physics to simultaneously predict pedestal width (average of Te and ne widths) and pedestal height (for pressure) for Type I ELMing discharges. This model has been applied to a number of recent discharges from C-Mod and DIII-D in which the measured pedestal pressure varied by a factor of about 20. The quantitative agreement of the predictions with these measurements is typically within 20% or better, with a strong correlation (r>0.8) between predicted and observed pedestal height.
- **Neutral Fueling:** Fueling of the pedestal by neutral deuterium atoms has been proposed as a mechanism for controlling the shape of the electron density pedestal, particularly its width. An alternative hypothesis is that plasma transport, such as a particle pinch or neoclassical physics, plays the dominant role in controlling the structure of the density pedestal. At least three modeling activities discussed within this report support the latter hypothesis: analysis of DIII-D data with a model that combines constraints set by particle and momentum balance, analysis of NSTX and C-Mod data with the paleoclassical model and self-consistent modeling of neoclassical transport and neutral fueling in C-Mod and DIII-D with XGC0. On the other hand, there are at least two experimental observations which suggest that neutral fueling might play an important role. Lithium deposition in NSTX reduced the deuterium wall re-cycling coefficient and provided a control for markedly increasing the width and decreasing the density gradient in the pedestal; an experiment to produce pedestals in C-mod and DIII-D with the same dimensionless parameters was able to match the Te profiles but the density profile in DIII-D was somewhat broader than in C-Mod. A tentative conclusion from all of these studies is that more than one physics process may be setting the density pedestal structure and the contributions of these processes could vary with experimental conditions.

Other significant physics results

- **Benchmarking Activity for Electromagnetic Gyrokinetic Codes:** Careful comparisons have been performed of GYRO (a continuum code), GEM and GTC (particle-in-cell codes) of the linear gyrokinetic stability of one well-diagnosed DIII-D pedestal. These comparisons helped to identify important issues for running these codes in the pedestal. For instance, plasma geometry was found to be very important. These studies predict that the dominant gyrokinetic modes are an electron drift mode in the steep gradient region of the pedestal and an ion temperature gradient mode on the pedestal top. A kinetic ballooning mode was found to be a sub-dominant mode with an onset condition in agreement with expectations from ballooning theory.
- **Study of QC-mode in C-Mod:** Simulations of Enhanced D-alpha (EDA) discharges in C-Mod with the BOUT++ code predict that unstable modes exist in the pedestal when the resistivity is high. These modes have several characteristics of the quasi-coherent (QC) modes observed in the C-Mod pedestal in these discharges. A possible interpretation of this result is that the QC mode is a resistive analogue of the kinetic ballooning mode, and that it limits pedestal gradients in the pedestal in a similar fashion as the KBM. This is supported by the experimental facts that the appearance of the QC mode is favored by high collisionality and that the pedestal pressure

gradient has a qualitatively similar scaling with plasma current as would be predicted by the KBM model. The SOLT and 2DX codes have also been used to study the EDA regime and provide evidence that nonlinear physics plays an important role in controlling the wavenumber and spectral character of the QC mode.

- **Study of I-Mode in C-Mod:** The I-mode regime was studied extensively in C-Mod and a wealth of data obtained to clarify the parameter ranges in which it exists and to document the physics of this mode. A key advancement was the extended characterization of a weakly coherent mode in the pedestal, an edge relaxation mechanism which is believed to regulate particle and impurity content while being compatible with H-mode like thermal transport suppression at the edge.
- **Study of Lithiated Discharges in NSTX:** Application of lithium to successive discharges in NSTX has produced a regime of operation with no ELMs. Significant understanding of the physics of this regime was obtained under the JRT. The application of lithium leads to a dramatic reduction of the wall recycling rate which in turn enables broadened pedestal density profiles with reduced gradients as compared to standard ELMing discharges. These profile changes lead to improved stability against kink/peeling modes, which would be expected to trigger ELMs, by increasing the separation of the peak of the bootstrap current and the separatrix.
- **Study of 3D Field Effects in DIII-D:** Modeling with the extended MHD code M3D-C1, using two-fluid physics, shows that the plasma rotation profile is very important in determining the plasma response to an externally applied n=1 error field in DIII-D. This modeling shows that the component of the electron rotation perpendicular to the magnetic field controls the tearing mode stability, as opposed to ion rotation or parallel flows. XGC0 has been used to study the effect of an applied n=3 magnetic perturbation on a DIII-D plasma. With a self-consistent treatment of the plasma response to the perturbation, the simulated pedestal profiles (density, temperature and radial electric field) show qualitative changes similar to those observed experimentally when the perturbation is applied.

Implications for ITER

The research reported here has implications for ITER in at least three areas: predictions for limits set by ELMs, predictions for pedestal height and modeling of the pedestal density profile.

- **ELM Threshold:** The peeling-ballooning model has provided a good description for the operational limits to the pedestal pressure set by Type I ELMs for discharges studied in the JRT. These results provide additional confidence that we can predict limits to the ITER pedestal set by Type I ELMs. However, the work reported here says nothing about predictions for the size of ELMs in ITER. Such predictions require advances in non-linear simulations of ELMs, work which is being performed outside this JRT.
- **Pedestal Height:** The EPED pedestal height model has provided good predictions of pedestal pressure height in new discharges in C-Mod and DIII-D. The new data has extended the range over which EPED has been tested. C-Mod provides significantly higher pressures than those tested previously and DIII-D has significantly increased the data set of large widths. Based on these and previous results, this model provides a reasonable basis for predicting the pedestal pressure height in ITER. Application of EPED to 5 tokamaks has provided predictions of pedestal height within

~20-25% of the measurements. Thus, this accuracy should be considered a reasonable estimate of the accuracy for application to ITER at this time. An important issue is to validate the KBM physics in the EPED model.

- **Density Pedestal:** Edge modeling of fueling in ITER predicts that neutrals will not penetrate into the pedestal under the assumption of diffusive particle transport. This result raises questions and concerns about whether the required density pedestal can be obtained in ITER. More than one modeling study within the JRT provides substantial evidence that additional physics is very important in forming the density pedestal. In particular, these results indicate that a particle pinch is present and more important than the fueling profile in controlling the density pedestal structure. Although there have been empirical studies which suggest that a pinch might be present, there is no definitive experimental measurement of a pinch. This remains an important open experimental issue.

Implications for future work

The research performed for this milestone has addressed and made significant progress on many pedestal issues. Many important pedestal issues remain open. Based on the results of this milestone, there are some crucial issues for advancing pedestal understanding and these are briefly noted here.

- **Maintain Modeling/Theory/Experiment Connections:** The JRT has significantly increased the interaction between the US modeling, theoretical and experimental communities in the area of pedestal physics. This interaction must be maintained and even strengthened if pedestal physics is going to develop the validated predictive capabilities desired for application to ITER and other future devices. A crucial issue for this interaction is the need for manpower to perform the activities of evaluating theory-based models and comparing the results to experiment. During this JRT, there was significant increase of manpower to do this task, particularly from junior scientists. This was a very healthy development for pedestal physics and it is highly desirable that it be maintained.
- **More than one Physics Process Likely to be Important:** Several physics processes, which are proposed to be important for pedestal structure, were studied as part of this milestone. With the results available at this time, it is plausible that most of these processes could be important in the pedestal, at least under appropriate conditions. In addition, these processes might not be cleanly separable in experiments. Thus, simultaneous consideration of multiple processes may be necessary to increase the probability for success in both modeling and experiment.
- **Gyrokinetic Benchmarking:** The linear gyrokinetic code benchmarking activity discussed elsewhere in this report has been a very significant accomplishment of the JRT. Given that gyrokinetic modes are proposed to be important for controlling pedestal structure both on top of and across the pedestal, it is crucial that gyrokinetic models be available as tools for interpreting pedestal measurements. This is a challenging task, due to numerous requirements imposed by pedestal physics. The benchmarking activity has been an important step in learning how to use existing gyrokinetic models in the pedestal and provides confidence in the results. This activity should be continued to completion and should be applied to a range of pedestal conditions.

- **Determine if Fluctuations Drive Important Transport In or On the Pedestal:** Measuring fluctuations was a significant part of this milestone activity because fluctuation-driven transport has been proposed to be important on top of and in the pedestal. However, interpreting these data and determining if the fluctuations drive transport is very difficult and advances in codes or diagnostic techniques are probably needed in order to accomplish this important task. For instance, the question could be addressed either by measuring the fluctuation-driven transport directly or with code calculations that could be used to compute profiles and turbulence characteristics. Significant efforts are required to make these advances.
- **Definitive Measurement that a Pinch Does or Does Not Exist:** As noted previously, modeling activities have strongly suggested that there is a particle pinch in the pedestal. From the standpoint of understanding the density pedestal structure and to provide input for ITER concerns, it is important to show definitively from experiment that a pinch either does exist or does not exist.
- **Pedestal Temporal Evolution:** Much of the experimental and modeling effort, performed in the JRT and elsewhere, focuses on the fully evolved pedestal structure and its stability. This work is providing an increasing understanding of how to project the pedestal structure, limited by Type I ELMs, to ITER conditions. In addition, some experimental studies are addressing the timescales for the pedestal gradients to form and for the pedestal widths to be established. These timescales are important issues for ITER modeling, which needs to know how fast the temperature and density pedestals will develop. Thus, there is an important need to improve our understanding of these timescales from experimental and modeling studies. This type of research will also provide an important tool to address questions about the physics processes in the pedestal, such as whether there is a particle pinch.

TABLE OF CONTENTS

I. EXPERIMENTAL CAMPAIGN FY11

1. ALCATOR C-MOD FINAL FY11 JRT REPORT (J.W. Hughes)

Pedestal studies on the Alcator C-Mod tokamak span three primary confinement regimes: ELMy H-Mode, EDA H-mode and I-mode. The ELMy H-mode is the typical high-power operating regime on most tokamaks, and provides a common mode of operation which all three devices involved in the JRT may access. A significant body of theory and modeling also has been built up around the ELMing pedestal, which makes it a good test case for predictive modeling. In addition to the ELMy H-mode, in which the pedestal relaxes via discrete events, C-Mod accesses EDA H-mode [1-1] and I-mode [1-2], regimes in which the pedestal gradients are limited by continuous relaxation mechanisms. The physics governing these benign relaxations is of interest because of the increasingly urgent need for ELM avoidance in ITER, and the difference in pedestal relaxation may have added implications for pedestal structure. There is therefore some degree of JRT work ongoing in all three confinement regimes.

1.1. Summary of Progress in Earlier Quarters

1.1.1. Experimental campaign

Prior to the beginning of FY11, an initial set of H-mode discharges from the C-Mod database were identified and evaluated for their suitability for pedestal modeling activities. The discharges included EDA H-modes, ELMy H-modes and I-modes. All were chosen to have well-diagnosed profiles of electron temperature and density from Thomson scattering, and some cases had sufficient information from charge exchange recombination spectroscopy on the B^{+5} impurity to produce well-resolved profiles of radial electric field. Some of these data sets were shared with modelers for initial analysis, using magnetics-only equilibrium reconstructions (EFITs), until improved reconstructions, constrained by kinetic profiles, could be generated. Gaps were identified in the data set, which informed the design of new pedestal experiments that directly supported the JRT. Using the results of group discussions among theorists and experiments, including the September 2010 C-Mod/NSTX Pedestal Workshop [1-3], new experimental proposals were generated, and significant run time was allotted for these in the FY11 run campaign.

Experimental run time on C-Mod in FY11 began in October 2010, continuing a run campaign that had actually been initiated late in FY10. Operations continued through early April, at which point a machine opening with manned access was planned which would last through the end of FY11. As a consequence of this scheduling, the C-Mod contribution to the JRT was “front-loaded” with experimental efforts, to be followed in the second half of the fiscal year with in-depth data analysis and modeling efforts. The campaign was very productive, with over 15 run days devoted to experiments related to the edge pedestal. These experiments, combined with earlier experiments that were developed in anticipation of the JRT, have provided an extensive data set for use in both scaling studies and modeling activities.

In collaboration with P. Snyder (GA), we obtained a new data set in ELMy H-mode, which has been used to test the EPED class of models for pedestal structure [1-4]. A planned plasma current scan was mostly completed, and we examined the effects of elongation and triangularity on the pedestal and ELMs. Atypical shaping is generally required to access ELMy H-mode on C-Mod [1-5]. One important finding of this experiment was that the ELMy H-mode could be accessed at values of elongation more in line

with usual operation (κ=1.55 rather than 1.45), although high lower triangularity and weak shaping of the plasma crown do appear to be important, even at the higher elongation. Figure 1-1 shows some example separatrix contours in which ELMy H-mode were obtained, and for comparison a more typical shape in which EDA H-mode is made. Helium H-modes, with and without ELMs, have also been accessed. In addition to these scans at the normal C-Mod toroidal field of 5.4T, new ELMy H-mode data were obtained in a field scan that reached values of 3.5T and 8.0T.

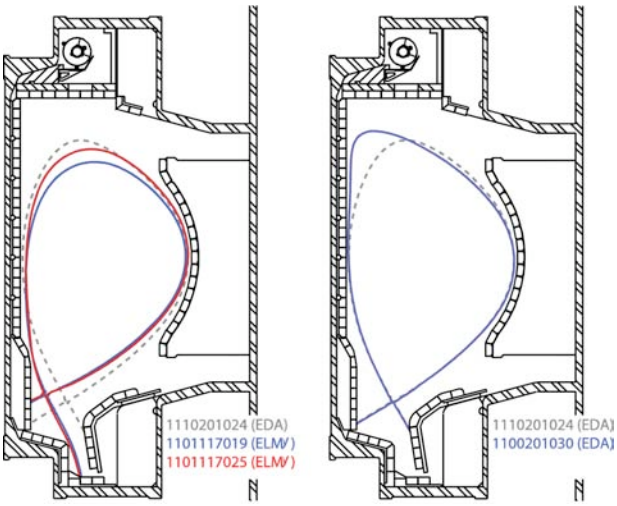

Fig. 1-1. (Left) Extremes of elongation in which ELMy H-mode has been obtained (red, blue curves) compared with a typical EDA H-mode shape (gray dashed). (Right) EDA H-mode pedestal and performance was evaluated with a healthy triangularity scan.

In addition to the ELMy H-mode experiments, a plasma current scan in Enhanced D-alpha (EDA) H-mode was obtained, with careful attention paid to characterizing pedestal profiles (electron temperature and density, ion temperature and flow velocities, radial electric fields) and edge fluctuation characteristics (Fig. 1-2). Also, at a fixed plasma current, upper triangularity was scanned from about 0.3 to 0.9 in order to test the dependence of pedestal structure on shaping. No substantial change was observed in either the pedestal width or the divertor heat flux profiles. These discharges form the basis of important comparisons with simulations from codes such as BOUT++ and M3D. Finally, a substantial amount of run time was allocated to I-mode studies, in which the team obtained improved characterization of both edge fluctuations and pedestal behavior [1-6].

1.1.2. Data analysis and distribution

Following completion of the FY10/11 experimental campaign, a number of data verification and calibration tasks were performed, to ensure that only accurate and trusted profile information is distributed to modeling colleagues. Thomson scattering data were checked for all pedestal runs contributing to the JRT. In order to correct for density calibration drifts observed through the latter portion of the campaign, cross-checks were made with the line-integral density from interferometry. These corrections could be significant in some cases, but by using a consistent technique applied across multiple run days, it is believed that the density profiles are now accurate to within approximately 5%. The edge CXRS team also was actively engaged in data verification. Good impurity profile data (including density, temperature and flow velocities) were obtained for a number of JRT-relevant discharges.

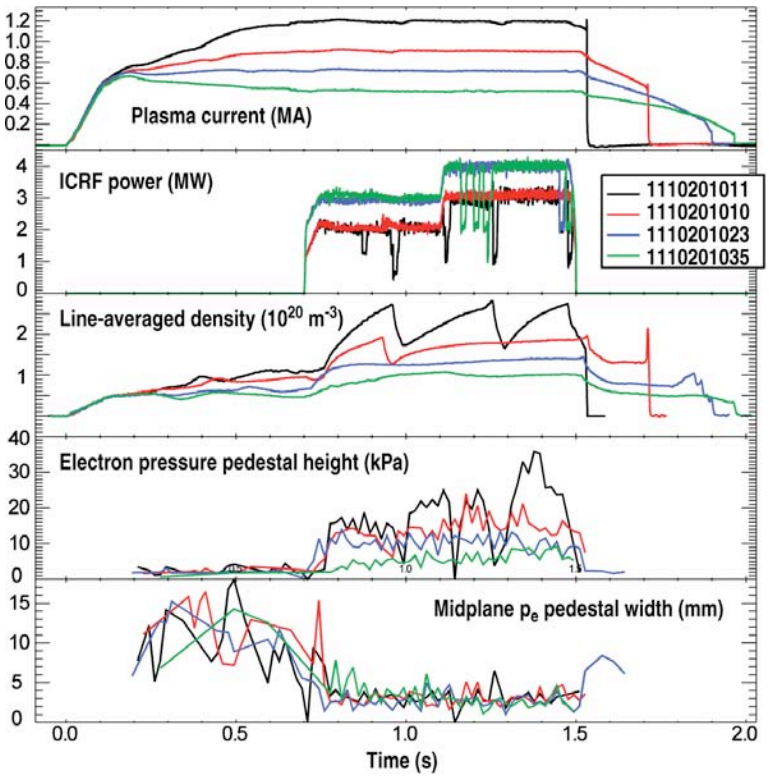

Fig. 1-2. A plasma current scan in EDA H-mode, used to establish a set of base cases for pedestal modeling. Increases in pedestal pressure with current are readily seen, while midplane pedestal widths vary weakly.

A set of profile analysis routines written and maintained by T. Osborne (GA) was successfully imported to the C-Mod computing cluster and interfaced with C-Mod data. These tools facilitate the preparation of fitted pedestal profiles and kinetic EFIT reconstructions for distribution to JRT modelers. DIII-D and NSTX data are also prepared using these tools, providing for a consistent treatment across devices. These tools produce pedestal profile results consistent with those from locally developed fitting routines, as well as code imported from the JET team. Both stand-alone free-boundary EFITs and "varyped" fixed-boundary EFITs are possible using these tools, the latter being a valuable input to modeling of edge stability as a function of edge pressure gradient and current density.

A data locker was created to hold C-Mod JRT verified data archives [1-7]. It is available to users with C-Mod computer accounts either by logging in to the C-Mod workstations or via a password-protected web page. Each data archive, which is keyed to a particular shot and time ID, contains files describing both the EFIT and kinetic profiles (the "a", "g" and "p" files), in the standard formats agreed upon by the JRT working group. New data sets will be continually added to the distribution as they become available, even after completion of the JRT.

In the first three quarters, strong initial efforts were made by a number of modelers to make contact with the C-Mod JRT data. This work continued at an accelerated pace in the fourth quarter. The status of this work is summarized in the next section.

1.2. Status of JRT Analysis and Modeling Efforts

1.2.1 ELMy H-mode

ELMy H-mode discharges on C-Mod spanning a broad range of operational parameters, including plasma current (0.4—1MA), axial magnetic field (3.5-8T), and plasma shaping, were realized as part of the JRT, and have been analyzed for empirical scalings of the H-mode pedestal width and height. Experimental density pedestal heights are consistent with a roughly linear dependence on the plasma current, as had previously been found in EDA H-mode scalings [1-8]; notably, a greater range of density is obtainable at a given current, indicating that density pedestals are less "stiff" than in the EDA H-mode [1-9]. The pedestal pressure gradient was found to scale more strongly than linear with the plasma current, again similar to that in EDA H-mode. Across the magnetic field scan, the plasma current remained the dominant scaling for pressure pedestal height. Measured pedestal widths in flux space are consistent with a dependence on the square root of poloidal beta at the pedestal top, and show no sensitivity on collisionality, normalized gyroradius or shaping (Fig. 1-3).

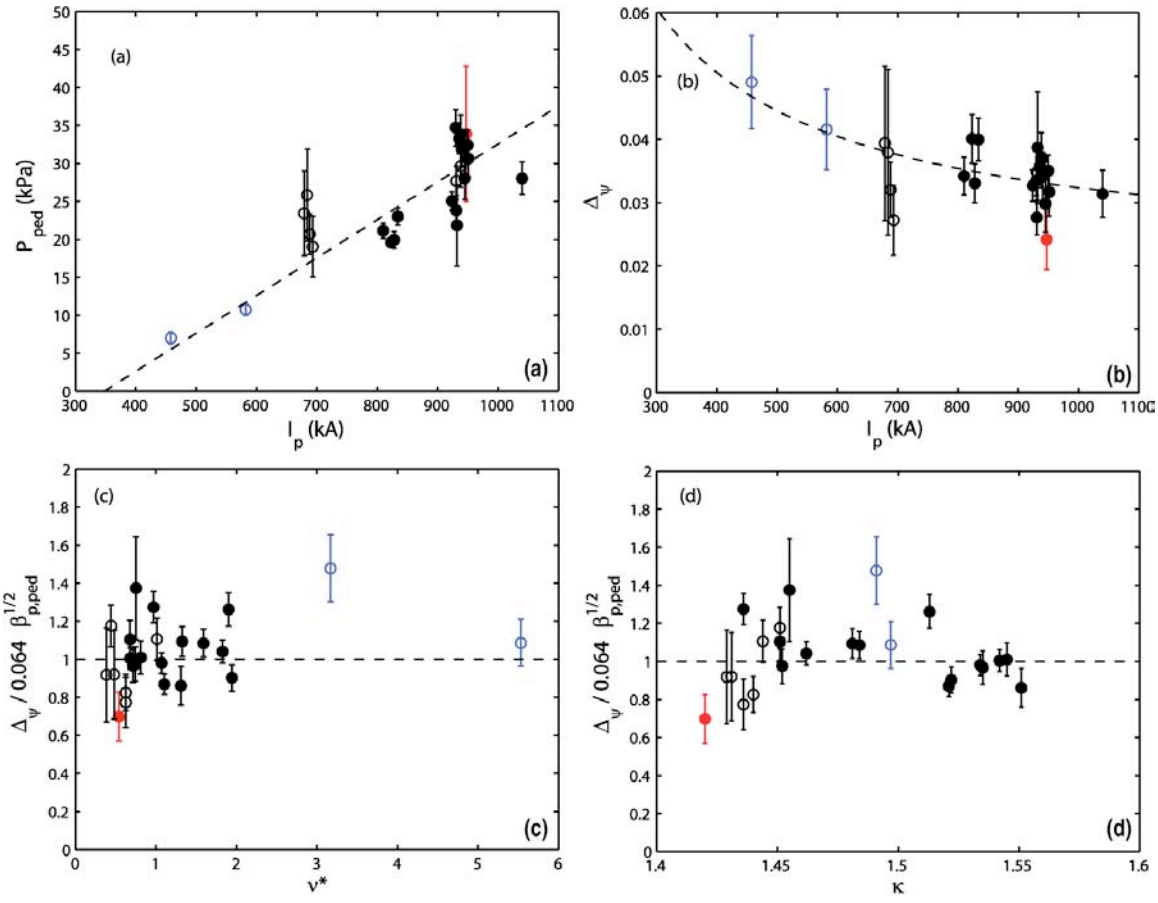

Fig. 1-3. Empirical scalings from FY11 ELMy H-mode runs. Plasma current dependence of (a) pedestal pressure and (b) pressure pedestal width. No systematic variation of width, normalized to empirical beta_pol scaling, is seen with (c) collisionality and (d) elongation.

Comparisons of C-Mod pedestal data to predictions from several versions of the EPED model have been carried out, over a factor of eight in pedestal pressure variation. Generally quite good agreement of

the pressure pedestal height and width has been obtained over a wide range of plasma current, toroidal field, and over a modest scan in elongation. A comparison with the most recent iteration of the model, EPED 1.63, is being readied for publication [1-4]. When experimental pedestal profiles are combined and fitted without consideration of measurement times relative to the ELM cycle (*i.e.* without ELM-synchronization), the experimental pressures are systematically lower than EPED 1.63 predictions. This discrepancy can be reduced considerably by only considering the pedestal profiles measured within the last 20% of the ELM cycle, when pressure is higher than on average. EPED predictions closely match the pedestal width, which ranges over 3—5% in normalized poloidal flux. Pedestal height predictions are found to be sensitive to the form of diamagnetic stabilization used in the model; however even with tweaks to the stabilizing terms, the model continues to reproduce empirical trends and matches measured values to within about 20%.

Peeling-ballooning stability calculations have been made for a subset of these ELMy discharges, verifying proximity of the pedestal to the stability boundary for medium-n modes. Currently the number of analyzed discharges is being increased, in order to obtain improved statistics. As described in the GA theory and DIII-D facility contributions to this report, comparison stability studies and EPED predictions are being made using a set of DIII-D discharges, run in Q4, which were designed to obtain a non-dimensional match to C-Mod ELMy H-mode.

Pedestal structure and stability studies done in the C-Mod ELMy H-mode and similar discharges at DIII-D are contributing to presentations at fall meetings, including the H-mode Workshop in Oxford (J. Hughes, P. Snyder, T. Osborne) and the APS-DPP (P. Snyder, J. Hughes, J. Walk)

1.2.2. EDA H-mode

The EDA H-mode has been extensively studied prior to the JRT, and has relatively well-characterized pedestal structure and transport properties [1-1,1-7]. The regime may exhibit small ELMs, but typically has no ELMs, and is maintained steady state via a continuous edge relaxation mechanism. This benign fluctuation is the quasi-coherent mode (QCM), and it is responsible for regulating particle and impurity content in the plasma while helping to maintain good energy confinement. Understanding QCM physics through computational modeling has been a key focus of C-Mod JRT activities.

Evan Davis, an MIT graduate student, visited LLNL to learn the BOUT++ code and to use it to do edge simulations of C-Mod discharges. The main goal of the BOUT++ simulations is to compare calculated fluctuation characteristics and radial electric field to those in experiment. This in turn should improve understanding of the quasi-coherent mode in EDA and the pedestal-limiting transport it provides. Prior BOUT simulations showed great promise in this area, although following up has had to wait for both full code maturity and the improvement of edge flow and fluctuation diagnostics on C-Mod. In the 4th quarter, substantial progress was made in computing edge stability with BOUT++ in the case of a typical EDA H-mode. The detailed findings are discussed in the LLNL contribution to this report. The chief conclusions from the initial study are that (1) unstable modes exist in the EDA pedestal when resistivity is high and (2) diamagnetic stabilization produces a mode spectrum peaked at n between about 10 and 30. These predictions are consistent with experimental diagnosis of the QCM, which appears at high collisionality, and is typically medium-n. The BOUT++ results show the unstable modes propagating in the electron diamagnetic drift direction (lab frame), also consistent with experiment. Work is ongoing to incorporate realistic flows and radial electric field profile into the simulation. This collaboration will

inform presentations at the Oxford H-mode Workshop (J. Hughes, X. Xu) and at APS-DPP (J. Hughes, E. Davis). Davis attended the BOUT++ Workshop at LLNL in September, as did another MIT graduate student, Ted Golfinopolous, and C-Mod scientist Brian LaBombard. They are making plans to use BOUT++ to model the response of QCM and other edge electromagnetic fluctuations to externally applied magnetic perturbations.

The EDA H-mode edge is also being simulated with M3D. The first simulations considered a 2008 discharge with a well diagnosed QCM instability with toroidal mode number n between 17 and 21. The initial ideal MHD equilibrium magnetic flux surface reconstructions used only magnetics data for input, ignoring the measured kinetic profiles. The measured pressure and density profiles were applied at the start of the M3D simulation, although this was inconsistent with the EFIT reconstruction. Also, there was no bootstrap toroidal current density layer in the pedestal gradient region. These cases were found to be linearly and nonlinearly stable to resistive MHD free boundary modes at central resistivities of 10 times the actual value, for toroidal mode numbers up to n=30. A study at 540 times the actual resistivity found unstable edge modes, but the modes became highly localized to the plasma edge region at higher harmonics $n > 20$. The results were not considered reliable, since MHD stability depends very strongly on the plasma profiles, which were not accurate to this level of detail.

The first M3D simulations using a kinetic EFIT with realistic edge pressure and density profiles were performed using JRT data from a discharge with an experimentally observed QCM instability (with n between 13 and 16). Simulations remain preliminary at this point, having used a rigid, perfectly conducting boundary, at the plasma separatrix, and no information about pedestal flows. These results show that the plasma is relatively stable to edge instabilities for the spectrum of toroidal harmonics up to $n = 23$ with a large central resistivity approximately 100 times actual. Work is continuing on other cases. In particular, kinetic data for the first QCM case is now available and will be compared to the initial results.

In support of experiments to understand the edge and SOL physics operative in EDA discharges, Lodestar has carried out modeling work using two different codes: SOLT and 2DX. SOLT is a non-linear fluid code that models turbulence (including arbitrary $\delta n/n$ amplitude blobs) in a two-dimensional region perpendicular to the magnetic field B at the outboard midplane of the torus. SOLT implements classical parallel physics using closure relations. Previous work in support of the JRT 2010 milestone [1-10] investigated the size and scaling of the SOL heat flux width in NSTX and C-Mod. This work has recently been extended [1-11] to further investigate a quasi-coherent oscillation which appears in the simulations. The SOLT mode has at least some qualitative similarities to the quasi-coherent (QC) mode that is observed experimentally in the EDA regime. The QC feature in SOLT results from density fluctuations at a wavelength of about 6 cm which originate in the strong gradient region just inside the separatrix, and are convected and Doppler shifted by the E×B flows. It is responsible for cross-field transport fluxes, and is a key player in setting the SOL width. Linear physics does not explain the dominant wavenumber in the simulations, i.e. why the density fluctuations peak at the relatively low value $k_y = 1\ cm^{-1}$. The role of nonlinear mode coupling and strong radial inhomogeneities in the edge region is currently being investigated. D. Russell will report on progress with SOLT at the APS-DPP.

Studies with the toroidal geometry, linear 2DX code are complementary to the SOLT nonlinear studies. 2DX is an eigenvalue code which incorporates realistic divertor geometry and global profiles in

the edge and SOL region. A special feature of 2DX allows convenient comparison of a wide variety of physics models. Neither drift-resistive modes (driven by plasma gradients and curvature), nor Kelvin Helmholtz (KH) modes (driven by radial shear in velocity) have so far provided linear candidates with growth rates that show a strong peak in the experimentally observed range of wave-numbers. Additional work is ongoing [1-12]. Thus the results of SOLT and 2DX taken together suggest that nonlinear physics plays a fundamental role in explaining the wavenumber and spectral character of the QC mode. J. Myra will report on progress with 2DX at the APS-DPP.

The C-Mod pedestal width has been compared with XGC0 calculations. Numerical studies, described in the CPES contribution to this report, show a neoclassical pedestal width that scales weakly with pedestal density and toroidal field, and which decreases with increasing poloidal field. Such scalings are not incompatible with empirical scalings from the C-Mod pedestal database. However, results to date have suggested a clear role for anomalous transport in broadening pedestal profiles and the SOL heat flux widths. A specific point of emphasis moving forward are impurity effects on pedestal width, as well as comparisons of simulation results with in-out impurity asymmetries observed in experiment. XGC0 will also be used in the comparative study of pedestals obtained in the Q4 C-Mod/DIII-D dimensionless match experiment.

1.2.3. I-mode

I-mode is a regime of operation that offers high energy confinement and weak particle confinement, via the decoupling of energy and particle transport suppression in the edge pedestal. The regime exhibits a strong temperature pedestal and no significant density pedestal, and tends to operate without ELMs of any kind (Fig. 1-4). Other edge relaxation mechanisms regulate the I-mode particle and impurity content so that it may run steady state, and a likely candidate for this is a weakly coherent mode (WCM), primarily observed in density and magnetics fluctuations, and localized to the edge. Because the I-mode is a relatively recent addition to the landscape of pedestal research, efforts to model it are not as advanced as for the H-mode regimes. However, in the past year, much progress has been made in characterizing experimentally the pedestal transport and fluctuations in I-mode, and systematic studies of the pedestal structure and stability are underway. A. Hubbard has given invited talks on I-mode edge physics at both the 2010 APS-DPP and 2011 EPS meetings. New I-mode results will also be shown at the H-mode workshop (A. Hubbard, J. Hughes) and the 2011 APS-DPP (E. Marmar)

Recent analysis has clarified a number of important features of the I-mode on C-Mod:

- The strong temperature pedestal in I-mode, in the absence of a density pedestal is associated with a ~5x drop in effective thermal conductivity in the pedestal (Fig. 1-4). This drop is well correlated with the suppression of density and magnetics fluctuations in the range of 60—150kHz, and the appearance of a weakly coherent mode (WCM) at 200—300kHz [1-5].
- In addition to being observed in density and magnetic field, the WCM is seen in fast electron cyclotron emission channels. Analysis indicates that the fluctuating T_e is 1—2% of the background [1-13], representing a weaker fluctuation than that in the density (6—13%), as measured by gas puff imaging [1-14].
- Comparative analysis of the WCM in I-mode with the QCM in EDA H-mode was done using gas puff imaging [1-13]. Although both modes propagate in the electron diamagnetic drift direction

when measured in the lab frame, indications are that only the WCM travels in this direction in the plasma frame, and that once ExB velocity is accounted for the QCM likely propagates in the ion direction.

- Whereas the mode amplitude for the QCM in EDA appears to be symmetric about the midplane, as diagnosed by LFS limiter magnetics, the WCM amplitude appears to be up-down asymmetric.

Joint work with ASDEX Upgrade has shown promise for reproducing I-mode phenomenology on devices other than C-Mod [1-15], and an open proposal exists to explore I-mode operation on DIII-D. Very recently, a candidate discharge on DIII-D was identified by R. Groebner and examined by D. Whyte as a potential starting point for such an experiment.

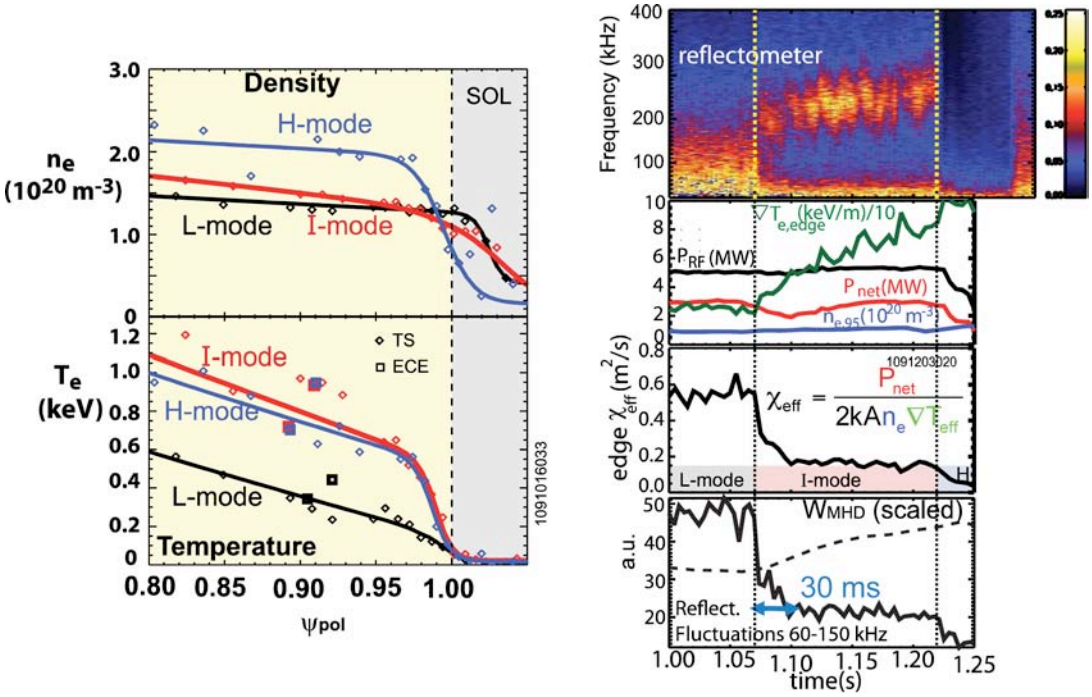

Fig. 1-4. (Left) Examples of pedestal density and temperature profiles in L-mode (black), ELM-free H-mode (blue) and I-mode (red). (Right) Evolution of a discharge (not the same one as at left) with an L-I and an I-H transition. A suppression of broadband edge turbulence in the range of 60—150kHz accompanies a substantial drop in effective thermal conductivity upon entrance into I-mode at 1.07s. Near complete suppression of turbulence and additional suppression of transport (including particles) is seen upon entrance into H-mode at 1.22s. Adapted from [1-5].

1.3. Future Work

The FY11 JRT was highly effective at enhancing the collaboration between the C-Mod pedestal research team and the modeling community. Progress has accelerated in the modeling of pedestal stability and turbulence, and we plan to continue this work moving forward. In the near term, the peeling-ballooning stability analysis of ELMy H-modes will be extended to the ELM-free stationary regimes: EDA H-mode and I-mode. We wish to verify the operating space for these regimes in relation to the boundary for peeling-ballooning instability. Calculations will be conducted both with ELITE and with BOUT++, the latter of which can provide a fairly complete treatment of diamagnetic stabilization, a very important term in the C-Mod pedestal.

Non-linear runs of BOUT++ will also be used to evaluate near-coherent fluctuations and the transport they drive in ELM-free regimes. In the coming year we wish to converge and synthesize the results of EDA simulations from independent codes: BOUT++, M3D, SOLT and 2DX. We will also attempt to simulate I-mode pedestals with codes like BOUT++ and M3D, insofar as they can be run in collisionless regimes. This will be a useful step toward preparing for the FY13 JRT, which is proposed to focus on stationary enhanced confinement regimes without large ELMs. Ongoing work with XGC0 to characterize the anomalous transport in C-Mod EDA H-modes will be extended to other confinement regimes, and comparisons of empirical measurements and transport calculations with predictions from paleoclassical theory will be incorporated, as they have been on other devices.

References for Section 1

[1-1] Greenwald M. et al. Fusion Sci. Technol. **5**1, 266 (2007).

[1-2] Whyte D.G. et al. Nucl. Fusion **50**, 105005 (2010).

[1-3] http://www.psfc.mit.edu/research/alcator/pubs/Cmod_NSTX_Wkshp_2010/index.html

[1-4] Walk J.R. et al., paper in preparation.

[1-5] Hughes J.W. et al. Nucl. Fusion **51**, 083007 (2011).

[1-6] Hubbard A.E. et al., Phys. Plasmas **18**, 056115 (2011).

[1-7] Contact Jerry Hughes (jwhughes@pfsc.mit.edu) for access to the JRT data.

[1-8] Hughes J.W. et al. Fusion Sci. Technol. **51**, 317 (2007).

[1-9] Hughes J.W. et al. Nucl. Fusion **47**, 1057 (2007).

[1-10] Myra J.R. et al., Lodestar Report #LRC-10-138, September, 2010, http://192.168.0.6/LRCreports/LRC-10-138_FY2010_JRT.pdf

[1-11] Russell D.A. et al., to be presented at the 53rd Annual Meeting of the APS Division of Plasma Physics, November 14-18, 2011, Salt Lake City, Utah.

[1-12] Myra J.R. et al., to be presented at the 53rd Annual Meeting of the APS Division of Plasma Physics, November 14-18, 2011, Salt Lake City, Utah.

[1-13] White A. et al, to be published in Nucl. Fusion, 2011.

[1-14] Cziegler I., MIT PhD Thesis, 2011.

[1-15] Hubbard A.E. et al, 38th EPS Conf. on Plasma Physics, Strasbourg, June 2011.

2. NSTX FINAL FY11 JRT REPORT (R. Maingi, D.P. Boyle, J.M. Canik, A. Diallo and the NSTX Team)

2.1. Completion of 4th Quarter Milestone – Executive Summary

The NSTX portions of the targeted goals for the fourth quarter and for the entire year were achieved, as documented below. The research was focused in two main areas: pedestal and stability characteristics in ELMy H-mode, and in the transition from ELMy to ELM-free H-mode enabled via lithium wall coatings. Experiments supporting each area were conducted in early FY11, and the analysis was completed during the remainder of the FY. The focus of our theory/experiment comparison was on peeling/ballooning stability analysis with ELITE; in addition, we performed simple estimates evaluating paleoclassical transport. Finally additional work was done to characterize the profiles and turbulence in Enhanced Pedestal H-modes.

We analyzed the evolution of pedestal, height, width, and gradients, as well as density fluctuations, during the inter-ELM cycle as a function of plasma current, I_p. Our list of high level findings include:

1. The pedestal pressure height P_{tot}^{ped} saturates only in the last 30% of the ELM cycle at low and intermediate I_p, and not at all at the high $I_p > 1$ MA.
2. The P_{tot}^{ped} increases ~ quadratically with I_p, and increases with lower divertor triangularity δ_l, but appears to be independent of toroidal field B_t.
3. The pedestal pressure width in physical space, P_{tot}^{width}, increases during the ELM cycle, and appears to be independent of I_p.
4. The pedestal pressure width in normalized poloidal flux (ψ_N) space, Δ, increases as the square root of pedestal β normalized to the poloidal magnetic field, β_θ^{ped}; the leading coefficient is notably however higher than other devices.
5. The maximum pressure gradient saturates early in the ELM cycle, but increases with I_p.
6. A coherent density fluctuation strongly increasing at the plasma edge was observed on reflectometry; the amplitude of this fluctuation was a maximum after the ELM crash, and it decayed during the rest of the ELM cycle.

We analyzed the evolution of global and edge plasma parameters during scans of increasing lithium deposition, during which plasmas transitioned slowly from ELMy to ELM-free. The main findings include:

1. Divertor recycling light and profile peaking factors decreased with increasing lithium evaporation between discharges; the cross-field electron thermal diffusivity χ_e at ρ=0.7 showed a continuous decrease with lithium evaporation.
2. Edge χ_e and particle diffusivity D near the top of the pedestal decreased with increasing lithium evaporation. Effectively the minimum level of transport in the steep gradient region of the H-mode barrier was extended inward from $\psi_N = 0.94$ to $\psi_N = 0.8$.
3. Density fluctuations measured from reflectometry and high-k scattering at the top of the pedestal were reduced by ~ 90%.

4. The ratio of T_e to n_e scale lengths, η_e, was close to 1, in the region where electron temperature gradient modes are expected to be destabilized, i.e. they may be responsible for the stiff T_e profiles. On the other hand, the magnitude and profile of the inferred electron thermal transport diffusivities from ψ_N = 0.8-1 was remarkably close to that predicted from paleoclassical transport theory for the with-lithium discharges.
5. Edge stability calculations with ELITE of this transition showed that the ELMy discharges were all near the kink/peeling boundary, far from the ballooning boundary; ELM-free discharges were removed from the kink/peeling stability limit.
6. The critical parameters that separated ELMy and ELM-free operation were the density and pressure profile width and symmetry point locations; large widths and symmetry points farther from the separatrix correlated with ELM-free discharges.

These results encourage the continued use of lithium for wall conditioning and edge studies in NSTX-Upgrade. It is likely that studies that target the reason for the confinement improvement, including the continuous dependence on the pre-discharge lithium evaporation amount, will receive initial priority. Moreover the location of NSTX discharges on the kink/peeling side of the peeling-ballooning diagram parallels that expected in ITER. One qualitative conclusion then is that control of the density profile could be critical for ELM control in ITER, just as it appears to be in NSTX.

The main body of this report is divided into two main sections: ELMy H-mode, and the ELMy to ELM-free transition with lithium coatings. In addition, a small section on advances in Enhanced Pedestal H-mode characterization is included, as that regime offers the prospect of separated particle and thermal transport channels.

2.2. ELMy H-mode Analysis

A defining feature of the high confinement or “H-mode” operational scenario is the existence of a transport barrier near the plasma boundary; this localized region of low transport is characterized by an increase in local gradients [2-1]. The plasma profiles thus develop a stairstep or “pedestal” shape, which is commonly referred to as the “H-mode pedestal”. This pedestal can be quite narrow in width and is interpreted as the interface between two regions during H-mode operation: the core plasma and the scrape-off layer. These two regions are governed by different physical mechanisms inherent in the wide range of spatial and temporal scales and also in the presence of sources and sinks of particles.

The presence of strong gradients in the pedestal region is often correlated with rapidly growing instabilities known as edge localized modes (ELMs) in many toroidal confinement devices. These ELMs result in a periodic, substantial drop of the plasma stored energy (typically < 10%) on the timescale of several hundred microseconds [2-2]. The reduction or elimination [2-3] of ELMs while maintaining high energy confinement is essential for the ITER, which has been designed for H-mode operation.

Detailed analysis has shown that large ELMs are triggered by exceeding either edge current density limits (kink/peeling modes) and/or edge pressure gradient limits (ballooning modes) [2-4 – 2-6]. Similar edge stability calculations using model equilibria have indicated that spherical tokamaks should have access to higher pressure gradients and H-mode pedestal heights than higher aspect ratio tokamaks, owing to high magnetic shear and possible access to second stability regimes [2-7]. Generally speaking though, spherical tokamaks have observed a wide variety of ELM types, many in common with higher aspect

ratio tokamaks [2-8,2-9]; true ELM-free regimes with high pedestal pressure gradients have been rare. The use of lithium in NSTX has enabled access to such a high pedestal pressure regime, one in which the core stability limits with high normalized beta are observed with no sign of ELMs [2-10]; these will be discussed in the next section.

To project forward ELMy H-mode operating scenarios to NSTX Upgrade, low aspect ratio designs for a Fusion Nuclear Science Facility, and ITER, a series of experiments was conducted [2-11] in NSTX. The main goal was to experimentally measure the scaling of the H-mode pedestal structure, i.e. heights, widths, and gradients, as a function of engineering parameters, e.g. plasma current I_p, toroidal field B_t, and lower divertor shape triangularity, δ_l. To the extent possible, we also attempted to compare results with available theoretical and numerical simulations. As described in the next section, we evaluated our edge stability with the PEST and ELITE codes, and interpreted our edge and divertor profiles and transport with the SOLPS code. While our original intent was to compare the pedestal structure measurements in this section with the EPED model [2-12], it was felt that the version of EPED under present development, EPED2, with a more accurate calculation of diamagnetic stabilization, would be more appropriate for future comparisons.

The experiments described in this section [2-11] were performed using neutral beam injected power from 4 to 6 MW. The discharges studied used a marginally double-null divertor configuration, with the plasma slightly biased downward, and the lower triangularity $\delta_l \sim 0.6$. The upper triangularity was typically kept at 0.4 and the elongation was kept between 2.3 and 2.4. To target ELMy discharges for studies reported here, a total of 50 mg of lithium was deposited on the bottom divertor plates between discharges. The key diagnostics utilized to characterize the pedestal parameters were the mid-plane Thomson scattering system [2-13] for electron density n_e and temperature T_e sampled at 60 Hz, the fully stripped C6+ charge-exchange recombination spectroscopy [2-14] for providing the carbon density and ion temperature T_i with a 10ms time resolution, and the divertor recycling light levels, e.g. D_α emission, for identifying ELMs. We characterized the evolution of the radial profiles between ELMs by reconstructing composite profiles synchronously with multiple ELMs. For this study, we focused on large type I ELMs of typical frequency ranging between 20 and 70 Hz. Individual radial profiles of density, temperature and pressure were first mapped using reconstructed EFIT equilibria [2-15,2-16] in normalized poloidal flux coordinates ψ_n ($\psi_n = (\psi_c - \psi)/(\psi_c - \psi_{sep})$, where ψ_c and ψ_{sep} represent the poloidal flux at the core and at the separatrix, respectively). These individual profiles were then collated together as a function of their timing relative to the ELM cycle; this can be regarded as a correlated sampling approach. The electron profiles were fitted with "standard" modified hyperbolic tangent fits, and the ion profiles were fitted with cubic splines. The resulting fit yields an estimate of the pedestal width (Δ) from which a gradient can be determined. The error in the fit in combination with an estimate of the scatter around the fit yields estimates on the error of the pedestal parameters. An example of a reconstructed density profile using this technique is shown in Fig. 2-1.

To capture details of the inter-ELM dynamics, the profile fits were performed around sliding temporal windows of 20% width. For example, we represent a window between 30% and 50% of an ELM cycle by its midpoint, which in this case is 40%. With this nomenclature, n_e or T_e *prior to* and *after* an ELM crash are identified as 90% and 30% of an ELM cycle, respectively.

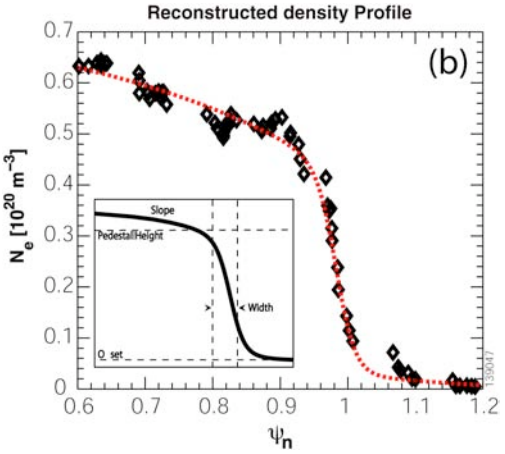

Fig. 2-1. Example of reconstructed n_e profile, using multiple time slices and conditional averaging, in synchronization with the ELM cycle [Diallo, NF 2011].

As shown in Fig. 2-2, we observed a clear buildup of the pedestal pressure before the onset of ELMs at all I_p, similar to observations in MAST [2-17] and AUG [2-18]. In the low and medium I_p cases, we observed a saturation of the pedestal height late in the ELM cycle, in contrast to the high I_p case where the pedestal height increased until ELM onset. A factor of 3 increase in pedestal height during the ELM cycle was observed at high I_p; this is similar to the 400% increase observed [2-19] in DIII-D. The saturation late in the ELM cycle in our data, however, contrasts with the DIII-D observations where the electron pedestal pressure saturates in the early phase, e.g. 20–50% of the ELM cycle.

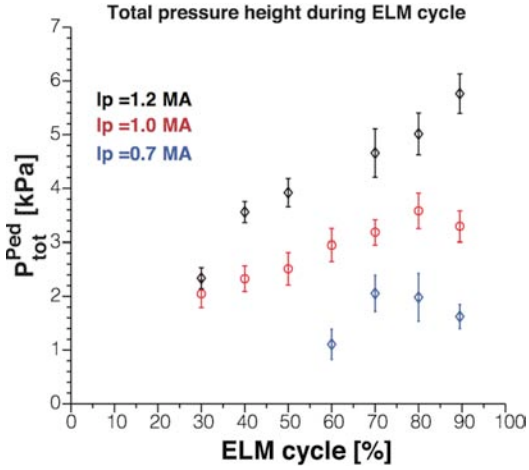

Fig. 2-2. Dependence of total pressure at the top of the pedestal as a function of the fraction of the ELM cycle, for 3 different values of I_p. [Diallo, NF 2011]

It is clear from Fig. 2-2 that the pedestal pressure increased with I_p. We display the total pedestal pressure during the last 20% of an ELM cycle as a function of I_p in Fig. 2-3. There is a near quadratic increase in the pedestal height prior to the ELM onset (e.g. 90% ELM cycle) with I_p. Note that the B_t was 10% higher for I_p = 900 kA and 1.1MA than that of I_p = [1.2, 1.0, 0.7] MA, but we show later that the pedestal parameters appear to be independent of B_t.

As shown in Fig. 2-4, the pedestal width Δ increases until the onset of an ELM to a nominal value of ~2 cm (0.085 in ψ_n units), at both low and high I_p. Moreover the physical space width seems to be largely independent of I_p at comparable fractions of the ELM cycle. For the medium I_p case, only one point is

included in the early stage of the ELM cycle as the remaining points have error bars too large to allow for meaningful comparison.

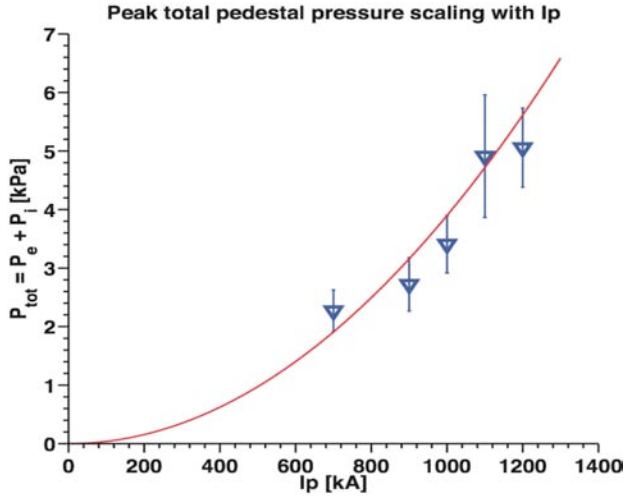

Fig. 2-3. Dependence of total pressure at the top of the pedestal as a function of I_p. [Diallo, NF 2011]

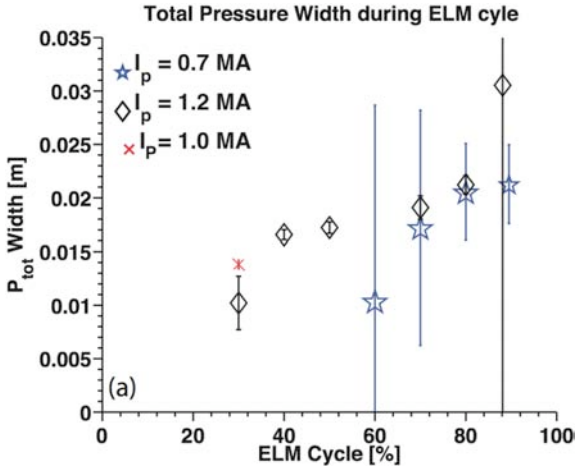

Fig. 2-4. Dependence of total pressure profile width as a function of the ELM cycle for three different values of I_p. [Diallo, NF 2011]

In contrast, Fig. 2-5 shows a clear dependence of the pedestal width in ψ_n space prior to the type I ELM onset, e.g. the last 20% of an ELM cycle, with the square root of pedestal β normalized to the poloidal magnetic field, β_θ^{ped}. The approximately square root dependence is consistent with experimental observations in DIIID and MAST, except the fitted constant coefficient in NSTX is ~ 70% larger than that of MAST [2-20] and 2.4 times greater than that of DIII-D [2-21]. The reason for the difference is under investigation.

Finally, Fig. 2-6 shows the maximum pressure gradient for various parts of the ELM cycle. While there is clearly an increase in the maximum pressure gradient with I_p, the maximum pressure gradient remains constant during the ELM cycle. This lack of variation in the maximum pressure gradient is consistent with recent observations in both AUG [2-22] and DIII-D [2-19,2-23], where the maximum pressure gradient initially increases and is limited at an early phase of the ELM cycle. In our case, the increase in the pressure prior to its saturation (before the 20% of the ELM cycle) could not be resolved. Hence, in view of this saturation prior to the ELM crash, the pressure gradient appears to play a weak role

in the triggering of an ELM. In the framework the peeling–ballooning physics, it is plausible that the edge current could play the key role just prior to the ELM crash.

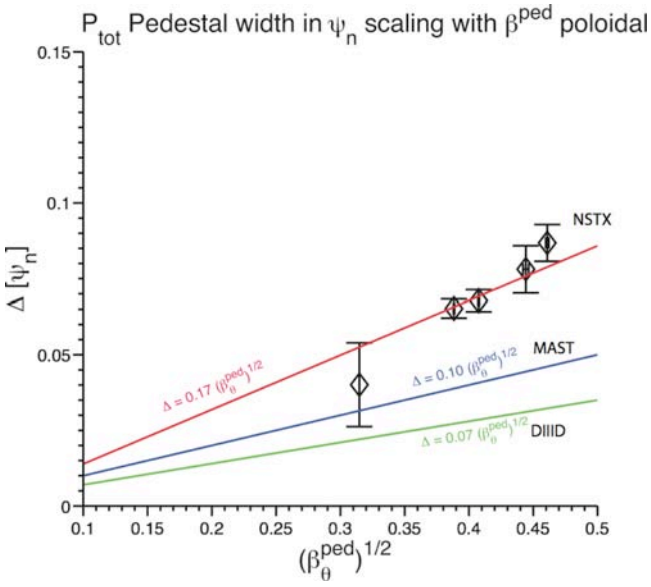

Fig. 2-5. Dependence of total pressure profile width as a function of normalized pedestal top pressure, β_θ^{ped}. [Diallo, NF 2011]

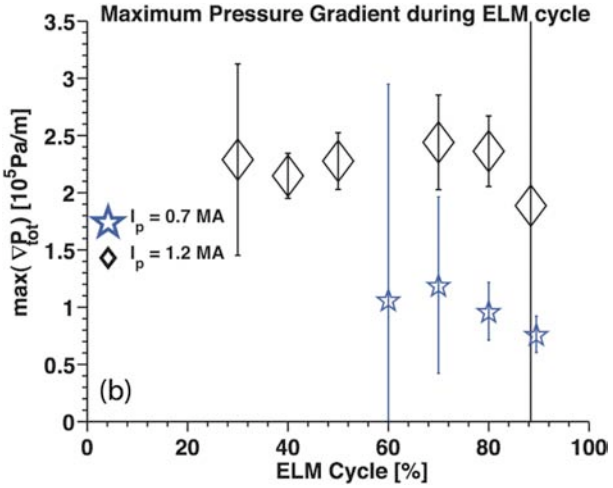

Fig. 2-6. Dependence peak pressure gradient in the H-mode pedestal as a function of the ELM cycle for three different values of I_p. [Diallo, NF 2011]

Finally we measured the dependence of the pedestal pressure height on lower divertor triangularity, δ_l, and B_t. Fig. 2-7 shows that the pedestal height increased with δ_l, although there is substantial scatter at any given δ_l. Initial measurements of the effects of B_t on pedestal height showed a negligible correlation. These data were obtained over a small range of B_t in ELMy discharges and a larger B_t range in ELM-free discharges, as shown in Fig. 2-8. Future experiments in NSTX Upgrade are needed for more confidence in these two dependences.

The density fluctuations at various stages of an ELM cycle were obtained using the 16-channel reflectometer probing the edge plasma; the analysis procedure was described elsewhere [2-11]. The observed density fluctuations exhibit a coherent peak in the vicinity of 12 kHz at the top edge of the density pedestal. The overall fluctuation level decreases prior to the onset of ELM. The characteristics of

the 12 kHz coherent fluctuation observed in the density fluctuations could not be attributed to modes detected on Mirnov signals, which indicates that either the peak density fluctuation spectra are too weak to be detected by Mirnovs or that they are electrostatic. Nonetheless, the observed fluctuations suggest that they are not likely to play a role in constraining the profiles inside the edge barrier, and they clearly do not exhibit the characteristics of kinetic ballooning modes, which are postulated to set the pedestal width in the EPED model [2-12].

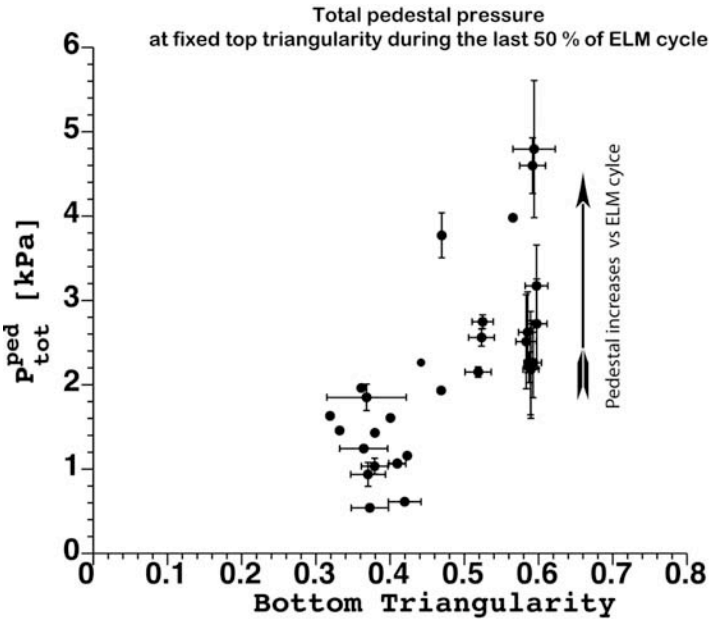

Fig. 2-7. Dependence of total pressure at the top of the pedestal as a function of lower divertor triangularity, δ_l during the last 50 % of the ELM cycle. The arrow indicates the increase of the pedestal height at fixed top and bottom triangularities. [Diallo, NF 2011]

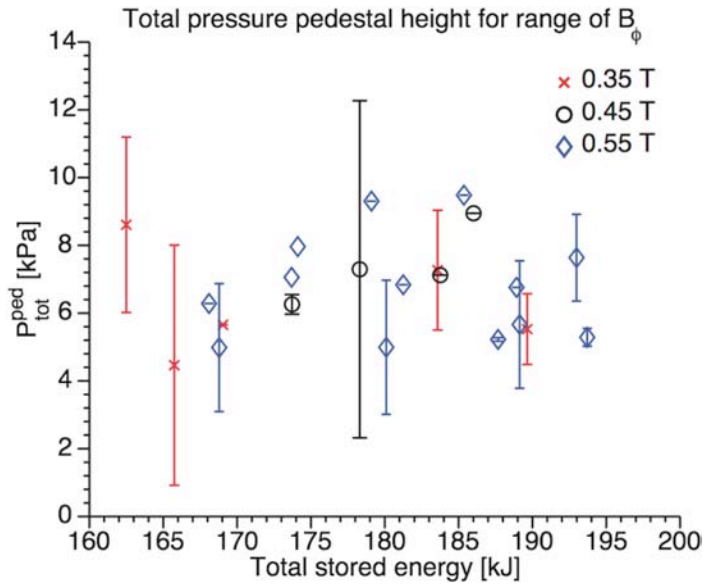

Fig. 2-8. Dependence of total pressure at the top of the pedestal as a function of B_t. This dataset was taken in ELM-free discharges, but the trend is reflected in the ELMy discharges, albeit in a narrower range. [Diallo, NF 2011]

2.3. ELMy to ELM-Free Transition with Lithium Wall Coatings

Lithium wall coatings have been used in a variety of devices to control edge recycling and improve energy confinement [2-24 – 2-28], and their use is a focal point of experiments in NSTX. Hence, analysis of the effect of lithium on edge plasma characteristics represents one of the unique contributions from NSTX toward this Joint Research Target report. Most of the data discussed in this section was obtained in previous years, but the in-depth analysis reported here was conducted in FY 2011.

Lithium was first introduced into the National Spherical Torus Experiment (NSTX) in 2005 via pellet injection, with modest, short-lived effects on the discharge characteristics [2-29]. A lithium evaporator (LiTER) was installed in 2007 to coat the lower portion of NSTX, resulting in reduced recycling, improved energy confinement, and a reduction of edge instabilities known as ELMs [2-30]. In 2008, a second LiTER was installed into NSTX to provide 360° coverage of the lower divertor, thereby eliminating shadowed regions [2-31,2-32]. Lithium from the previous campaign's experiments had been removed by sanding of the tiles during the vent prior to the operations. Approximately a month of dedicated experiments using periodic boronization of the graphite plasma-facing components (PFCs) was used to provide reproducible ELMy H-modes with good energy confinement.

A reference scenario with ordinary Type I ELMs was developed several years ago in an Alcator C-Mod/MAST/NSTX similarity experiment [2-33] on small ELM regimes. These ELMs had a fractional stored energy drop $\Delta W/W \sim 2\text{-}5\%$, nominal frequency of ~ 100 Hz that increased with heating power, in a boundary shape with a relatively high X-point for NSTX, with $\delta_r^{sep} \sim -5$mm. Here δ_r^{sep} is the distance between the two X-points mapped to the outer midplane, where the convention that $\delta_r^{sep} < 0$ means the lower X-point is closer to the plasma than the upper X-point. There are no small, Type V ELMs in this discharge scenario, which are otherwise common [2-34] in NSTX. Other relevant discharge parameters were: I_p=0.8 MA B_t=0.45 T, P_{NBI}=4 MW, and line average electron density n_e from 4 - 6.5 x 10^{19} m^{-3}. Periodic boronizations in the run campaign had been applied prior to this experiment.

The lithium was then introduced gradually but systematically, to thoroughly document its impact on global discharge characteristics, including ELM activity, as well as plasma profiles. The amount of lithium deposition between discharges was chosen carefully such that the transition from ELMy to ELM-free discharges would occur over at least 10 discharges. HeGDC of 6.5 minute duration was used between all of the discharges, followed by lithium evaporation from two overhead evaporators. Note that subsequent experiments demonstrated that HeGDC is unnecessary with lithium coatings between discharges. During the plasma discharges, a shutter was used to prevent lithium evaporation into the vacuum vessel to avoid coating of the windows. Additional details of this experiment and preliminary analysis are published elsewhere [2-35].

Figure 2-9 shows the lithium deposition between discharges during the sequence, as well as the cumulative deposition. The deposition rate was kept approximately constant between the first 9 discharges starting with #129021, and was gradually increased afterwards. We emphasize that this sequence was the first use of lithium in this campaign, insuring that the reference discharges were truly pre-lithium. The gas fueling, P_{NBI}, and boundary shape were held constant until the very end of the scan, when higher fueling and lower P_{NBI} were needed to avoid low density locked modes and resistive wall modes.

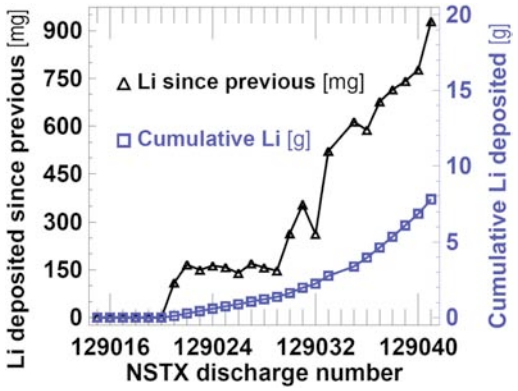

Fig. 2-9. Amount of lithium deposition before subsequent discharge, and cumulative deposition in the discharge sequence. [Boyle, PPCF 2011]

The evolution of the divertor D_α for the sequence is shown in Fig. 2-10. The external gas fueling was held constant until #129036, and then it was increased on the subsequent discharges. The P_{NBI} was held constant at 4 MW until #129033, after which it was reduced in steps to avoid the locked modes.

The effects of lithium are apparent in the second lithiated discharge #129022, in that the ELM frequency was reduced. ELM-free periods of increasing duration are evident after #129024, but the progression to full ELM-free operation was not monotonic. Even as more lithium was added, fully ELMy discharges returned (129027, 129029, 129032). These ELMy discharges all coincided with a sustained period of low confinement, high recycling L-mode at the end of the previous discharge (129026 had no neutral beam heating; 129028 and 129031 suffered locked modes). Discharges 129029 and 129030 also suffered locked modes and ended in periods of L-mode but were followed by discharges with ELM-free phases. However, these L-mode periods were shorter and had very low stored energy. One possible explanation [2-36] for the return of ELMs is that the accumulated lithium was passivated by the sustained L-mode discharges, and the amount of fresh lithium in these discharges was by itself insufficient to suppress ELMs. Discharges 129033, 129036, 129038 and 129041 were ELM free despite following periods of sustained and/or high stored energy L-mode. In these cases, the thick coatings of fresh lithium were able to suppress ELMs by themselves, regardless of the condition of the previously accumulated lithium.

The discharges #129033 and #129035 - #129037 did not achieved sustained H-mode phases, as the combination of heating power (P_{NBI}=2 MW) and external fueling was not optimized until #129038. Discharges #129039 and #129041 both disrupted at 0.35sec and 0.515 sec respectively, as a result of higher β_N from an increase of P_{NBI} to 3 MW. In addition, #129041 had modestly higher external gas fueling than #129038 and #129039.

The evolution of other relevant plasma parameters during the scan is shown in Fig. 2-11. Panel (a) shows that the lower divertor D_α at t=0.4 sec gradually decreased with increasing lithium coatings, dropping substantially at the highest coating values. The upper divertor D_α at t=0.4 sec gradually decreased with increasing lithium coatings also (panel (b)), showing an even larger fractional drop than the lower divertor D_α; this suggests that the lithium evaporated into the lower divertor might have been transported to the upper divertor through plasma-wall interactions, where it reduced recycling. The line-average density at t=0.4 sec was gradually reduced also, while the peak plasma stored energy W_{MHD} and β_N (generally between 0.45 and 0.6 sec) from equilibrium reconstructions [2-16] gradually increased. Again, the last three discharges had reduced P_{NBI} compared to the other discharges. Finally panel (f) shows that the confinement enhancement factor relative to the ITER97-L scaling increased slowly during the coating scan.

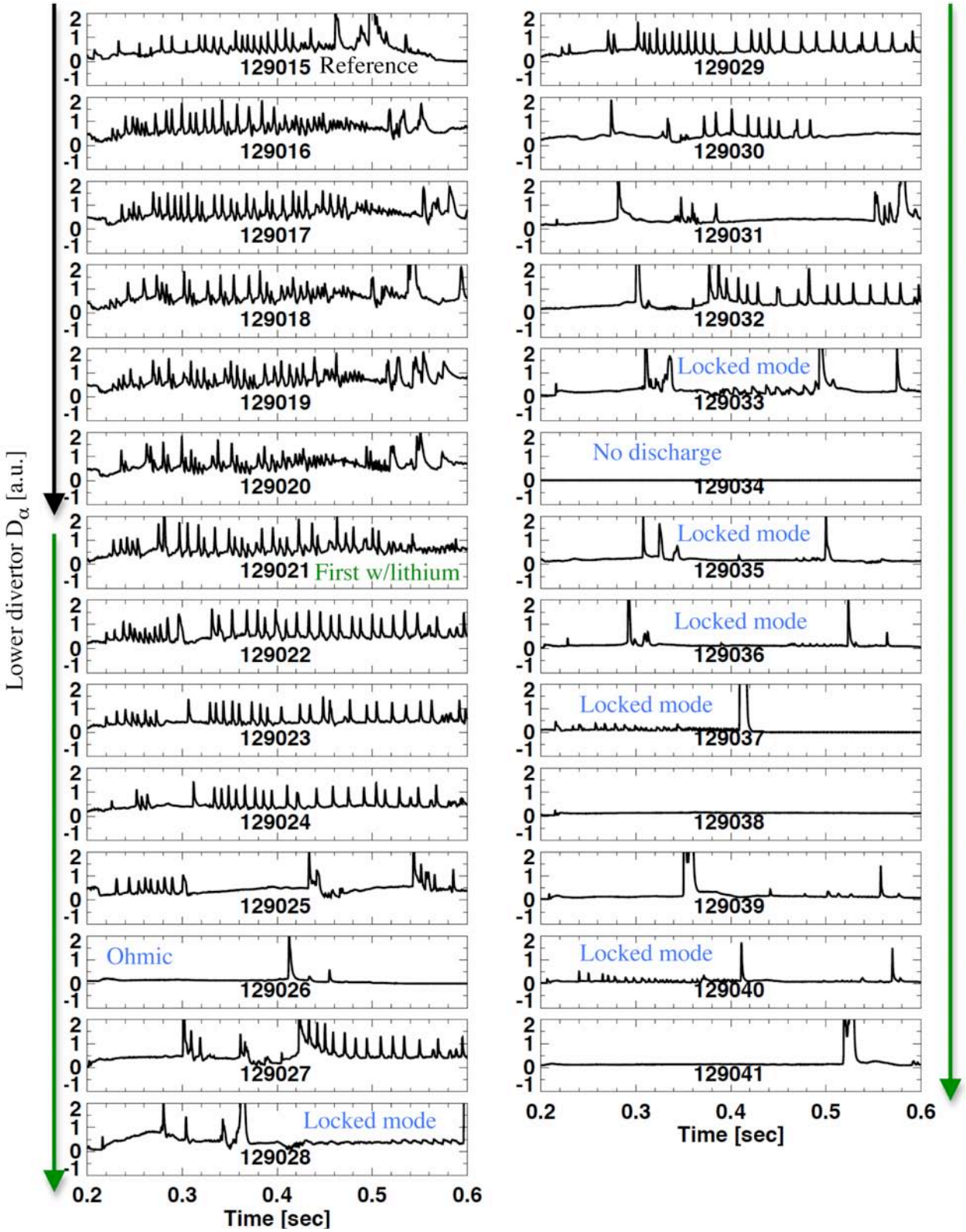

Fig. 2-10. Evolution of lower divertor D_α emission during discharge sequence, showing the gradual effect on ELMs. The black vertical arrow indicates reference, non-lithiated discharges, and the green arrows show lithiated discharges.

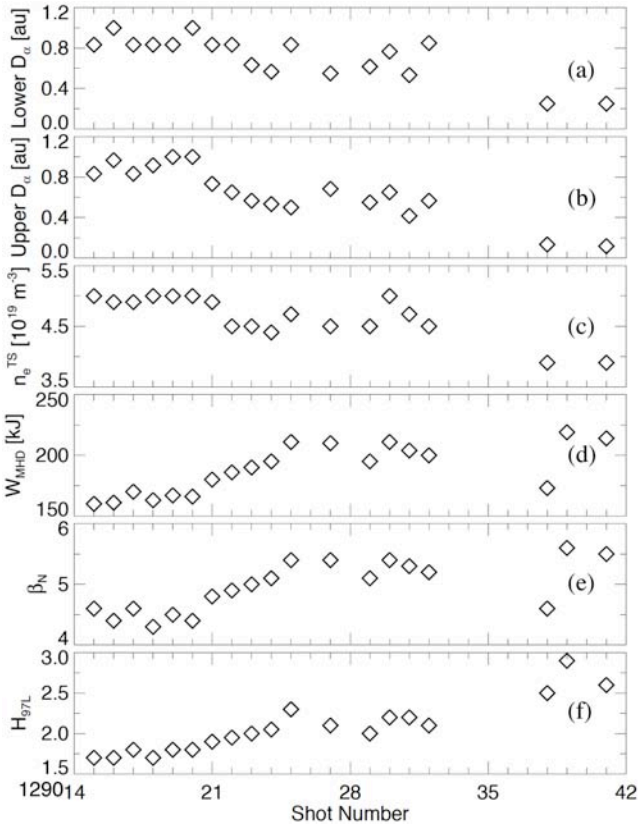

Fig. 2-11. Evolution of plasma parameters during systematic scan: (a) Lower divertor D_α baseline value at t=0.4 sec, (b) upper divertor D_α baseline value at t=0.4 sec, (c) line average density from Thomson scattering at t=0.4 sec, (d) peak stored energy W_{MHD}, (e) β_N at time of peak W_{MHD}, and (f) energy confinement relative to ITER97-L scaling at time of peak W_{MHD}. Lithium was added starting with #129021. The P_{NBI} and gas fueling were varied in the final three discharges. [Maingi, PRL 2011]

The electron kinetic profiles were correlated with the amount of pre-discharge lithium deposition, as shown in Fig. 2-12. The n_e peaking factor initially increases as the lithium deposition is increased; this is due to a general reduction in the edge density. As the discharges became less ELMy, the density profile gradient was reduced, leading to a reduced peaking factor in the latter half of the discharge sequence. On the other hand, the T_e and P_e profiles peaking factors decreased nearly monotonically with increasing lithium deposition, consistent with a analysis of a broader dataset [2-31]. The ion profile peaking factors did not show a clear trend during the scan.

The core transport during this scan was evaluated with the TRANSP code [2-37,2-38]. The procedure uses the kinetic n_e and T_e profiles from Thomson scattering data, the T_i and n_C data from CHERs, Z_{eff} from visible Bremsstrahlung radiation, radiated power from bolometry, reconstructed equilibrium from the EFIT code [2-15,2-16], and neutral beam (NB) data. Monte Carlo techniques are used to compute the NB deposition, and no fast ion diffusion was used. A match to the neutron rate was achieved by varying the edge neutral density. The analysis showed [2-39] that both the total and electron τ_E increased with increasing lithium deposition; indeed, the electron τ_E increased more rapidly than the global τ_E. In addition the edge electron thermal diffusivity at r/a=0.7 χ_e decreased strongly with increasing lithium deposition; in contrast the ion thermal diffusivity χ_i actually increased modestly. On the other hand, the core χ_e, χ_i, and χ_ϕ at r/a=0.35 were insensitive to or weakly increasing with the pre-discharge lithium deposition. These results agree with analysis [2-40] of a broader dataset, which included a few of the discharges from this scan.

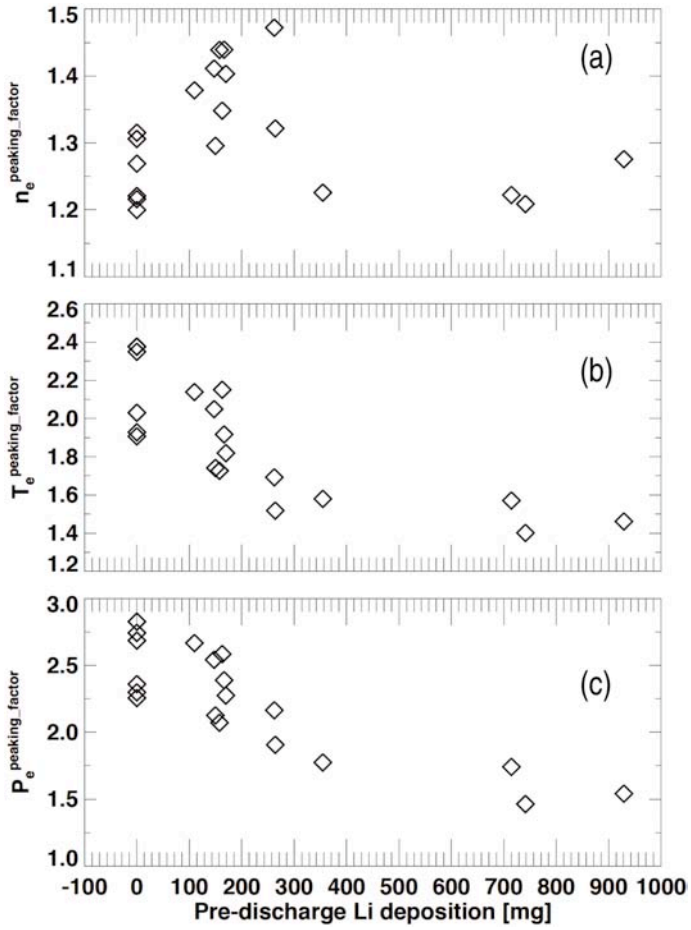

Fig. 2-12. Dependence of profile peaking on lithium deposition: (a) n_e profile peaking factor, (b) T_e profile peaking factor, and (c) P_e profile peaking factor. [Maingi, PRL 2011]

To illustrate the dramatic effect of high lithium deposition between discharges (> 400 mg), we now compare the time evolutions for a reference ELMy discharge with two completely ELM-free discharges. Figure 2-13 shows the evolution of a boronized ELMy discharge (black), with two lithiated discharges, one with low input power (orange), and one with intermediate input power (blue). Panel (a) shows that the ELM-free discharges lasted longer, and panel (b) shows the ELM activity as spikes on the divertor D_α emission. Note that the baseline divertor D_α emission was substantially lower in the with-lithium discharges, indicating reduced recycling. At these high inter-discharge evaporations, the energy confinement τ_E increased such that the heating power needed to be reduced to avoid the global stability limit [2-10,2-35]; hence, panel (c) shows a range in P_{NBI} from 2 to 3 MW in the discharges with lithium, compared with P_{NBI}=4 MW in the reference discharge. Note that the discharges with lithium near the end of the lithium coating scan with P_{NBI}=4 MW had large locked modes shortly after the I_p flat-top (not shown). Panel (d) compares the normalized plasma pressure β_N, where $\beta_N=\beta_t B_t a_m/I_p$, and $\beta_t=4\mu_0 W_{MHD}/(3V_p|B_t|^2)$ is the plasma pressure normalized to the on-axis vacuum toroidal field B_t, a_m is the minor radius, I_p is the plasma current, μ_0 is the permeability of free space, and W_{MHD} and V_p are the plasma stored energy and volume from equilibrium reconstructions. Despite the reduction in P_{NBI} from 4 to 2 MW, the orange and black discharges had nearly identical peak β_N and stored energy. An additional 1 MW of NBI power in the blue discharge increased $\beta_N \sim 5.5$, i.e. where resistive wall modes are typically encountered [2-41,2-42] in NSTX. Indeed the sudden drop in β_N in the blue discharge at ~ 0.5 sec was correlated with magnetohyrodynamic (MHD) activity typical of resistive wall modes. Panel (e) shows that

the τ_E normalized by the ITER-97 L-mode global scaling [2-43] was 50% higher in the with-lithium discharges. The discharges with lithium in Fig. 2-13 showed reduced early density and dN/dt, although the eventual density in the lowest power discharge reached the same value as the reference discharge, partly because of the lack of ELMs. Also the radiated power fraction increased with time in these ELM-free discharges [2-10,2-30,2-31,2-35], because ELMs typically flush impurities, preventing temporal accumulation. While this temporal increase in radiated power is a hindrance in developing these lithiated ELM-free discharges into long pulse scenarios, other methods have been shown to reduce impurity accumulation, e.g. with pulsed 3-D fields [2-44,2-45] or use of the "snowflake divertor" configuration [2-46].

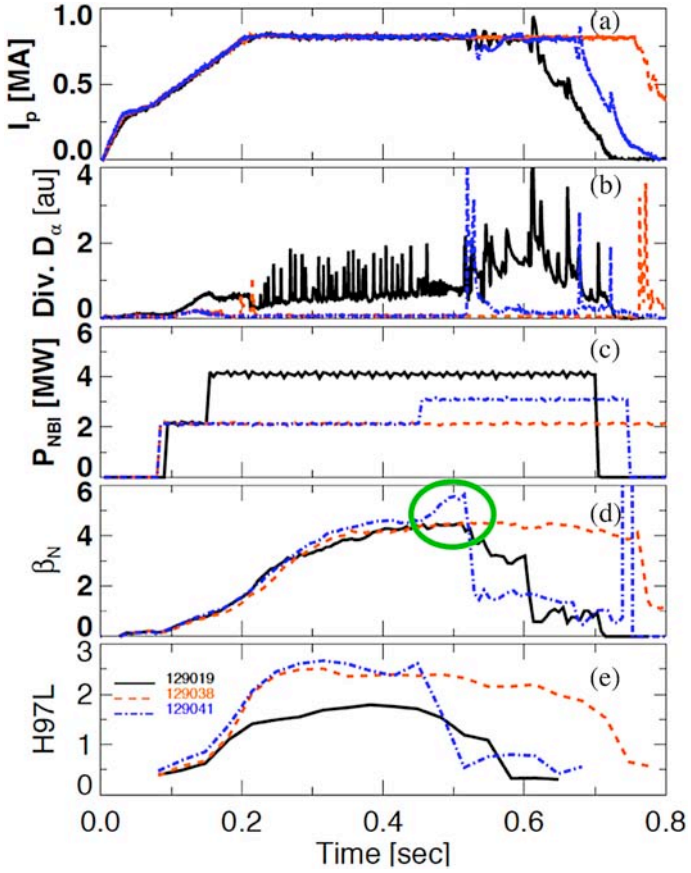

Fig. 2-13. Comparison of one of the reference pre-lithium ELMy discharge (black), and two with-lithium discharges with different NBI power (blue, red): (a) plasma current I_p, (b) upper divertor D_α emission, (c) neutral beam injected power P_{NBI}, (d) normalized plasma pressure, β_N (e) confinement time relative to ITER97L scaling.

The effect of lithium conditioning on the plasma kinetic profiles for the 2 MW lithiated and 4 MW boronized discharges from Fig. 2-13, is displayed in Fig. 2-14. The technique used for the profile analysis is described elsewhere [2-47]; briefly, synchronization with the ELM cycle is used to produce conditionally-averaged profiles from a number of the ELMy reference discharges, while 100 ms windows are used to construct composite profiles in the ELM-free discharge, #129038 from Fig. 2-13. Panel (a) shows that the electron density n_e gradient (from Thomson scattering [2-13,2-48]) was clearly reduced in the lithiated discharge, while panel (b) shows that the edge ion temperature T_i from charge exchange recombination spectroscopy was markedly higher. Panel (c) shows that the electron temperature T_e gradient was comparable near the separatrix from normalized poloidal flux ψ_N to 0.95-1.0, but the steep gradient region extended into ψ_N of 0.8 in the with-lithium discharge. Panel (d) shows that the edge ion

toroidal rotation from CHERs was higher in the lithiated discharge, despite the reduction in neutral beam power/torque. Note that the peak pressure Ptot and its gradient were shifted radially inward farther from the separatrix. The changes to the ion pressure profile were subtle [2-36], because the increase in T_i was offset by a decrease in ion density, due to increased Z_{eff}. Hence the total pressure gradient was dominated by the electron gradients in all cases. Two ELM-free pressure profiles are shown in panels (e) and (f) to demonstrate that the peak pressure gradient was actually higher in some of the ELM-free composite profiles, but was generally shifted inward away from the separatrix, i.e. at ψ_N=1. This inward shift of the pressure profiles with lithium resulted in a similar shift of the bootstrap current, which was stabilizing to the kink/peeling modes thought to be responsible [2-10] for these ELMs in NSTX.

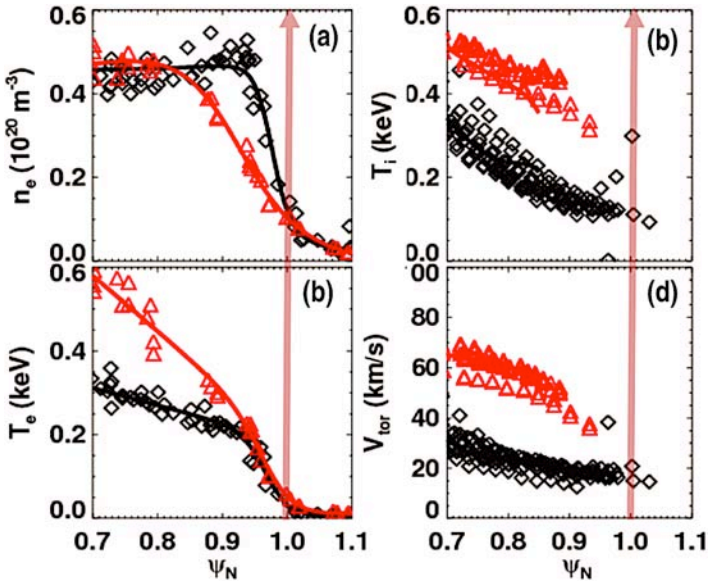

Fig. 2-14. Profile comparison of no-lithium (black) and with-lithium discharges (red): (a) n_e, (b) T_i, (c) T_e, (d) V_{tor}, for pre- and with-lithium discharges.

Figure 2-15 shows that the measured ELM frequency during discharges from this sequence decreased with increasing discharge number, i.e. increasing lithium deposition. Clearly, the transition to ELM-free operation was not quite monotonic, however, in that several discharges with substantial ELM-free periods were followed by ELMy discharges. The data points in black had edge profiles that were analyzed with the ELM-synchronization method mentioned above, whereas the data points in blue were unsuitable for profile analysis, but were included for more insight into the trends. There are several discharges with more than one data point per discharge; in those cases, the edge profiles were analyzed in non-overlapping time windows of duration ~ 0.1 sec. This was necessary because the discharges had both an ELMy and an ELM-free phase, or long ELM-free phases with evolving density.

The n_e, T_e, and P_e composite profiles were fitted [2-36] with a "standard" modified hyperbolic tangent ("mtanh") function [2-49], which includes both a tanh component and a linear component. The ELM frequency from the black data points is shown as a function of these pedestal widths in panels N15 (b), (c), and (d). The additional data points in red were obtained in discharges with heavy lithium wall coatings run in the 2009 campaign, using the same discharge programming and reduced P_{NBI}, as in #129038. The n_e and P_e profile widths are both shown to order the ELMy and ELM-free data, mostly as a threshold criterion. The T_e profile width can be immediately ruled out as an ordering parameter. Since the

lithium mainly changes the recycling and the edge fueling, these trends support the hypothesis that the density profile change is central to the ELM suppression.

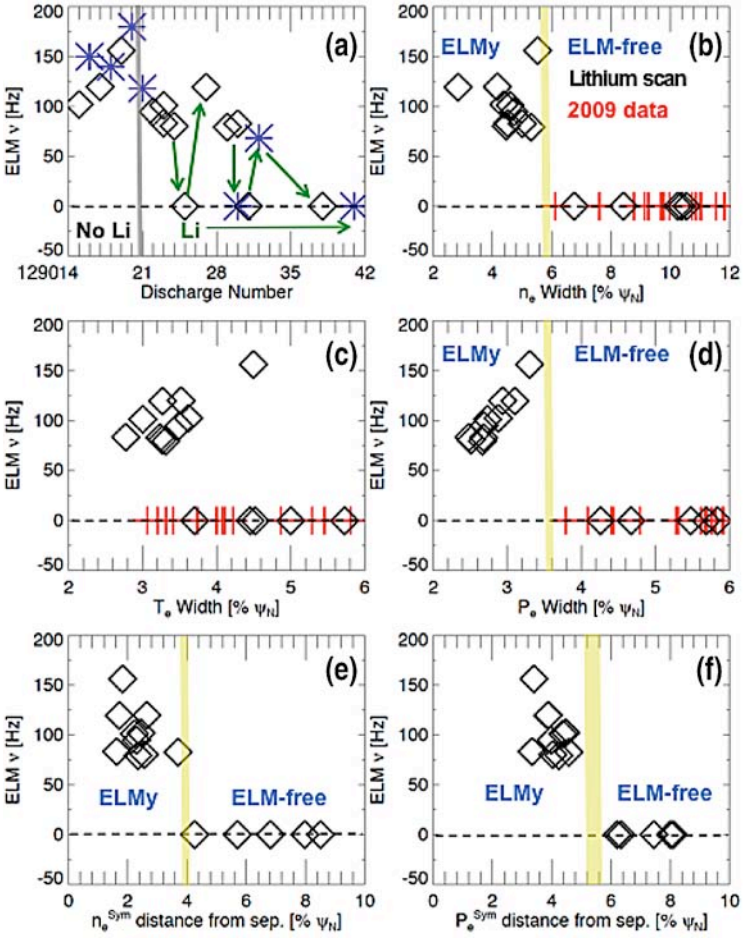

Fig. 2-15. (a) Average ELM frequency during the scan; discharges with both ELMy and ELM-free periods of duration > 100ms are shown with multiple data points. (b) ELM frequency dependence on the fitted widths of the (b) n_e, (c) T_e, and (d) P_e profiles. Panels (e) and (f) show the ELM frequency vs. the distance from the n_e and P_e tanh function symmetry points from the separatrix. Converged tanhh fits could not be obtained for the blue data points in panel (a), but they are included to reflect the ELM frequency trend. Data from additional similar, more recent discharges are included in red in panels (b), (c), and (d), but additional uncertainty in the separatrix location precludes their addition in (e) and (f).

In addition to the profile widths, the mtanh profile fitting yields the pedestal top value and its location, the peak gradient and its location, and the pedestal bottom value and its location. A thorough analysis of the correlation between ELM frequency and the other parameters from the tanh fits showed that ELMy and ELM-free discharges were also organized by the location of the peak n_e and P_e gradients [2-36], i.e. the symmetry point of the tanh function. Figure 2-15(e) and (f) show the ELM frequency vs. distance of the n_e and P_e symmetry point from the separatrix; indeed, there is a threshold distance that organizes the ELMy and ELM-free data. This is unsurprising, because as the characteristic width of a profile grows, the location of its peak gradient shifts also, provided the location of the bottom of the profile remains fixed. It is relevant, however, because the location of the symmetry point coincides with the location of the peak bootstrap and local parallel current in the kinetic equilibria; increasing the separation between this current and the separatrix improves stability to kink/peeling modes. Note that the 2009 data are not included in Fig. 2-15(e) and (f) because of possible systematic uncertainty in the separatrix location for those discharges relative to the main sequence in Fig. 2-9; this uncertainty would affect the computed symmetry point to separatrix distance, but not the profile widths in Fig. 2-15(b), (c), and (d).

Many of the discharges in this sequence were simulated [2-50] with the 2-D edge plasma and neutrals code SOLPS [2-51], to interpret and quantify the change in edge recycling and transport. Parallel transport in SOLPS is classical, with kinetic free-streaming corrections. Recycling and other neutral source terms are computed with the Monte Carlo code, EIRENE [2-52]. Cross-field transport is anomalous and user-defined; in these simulations, radial profiles of the particle and thermal diffusivities were iterated to match the midplane n_e, T_e, T_i, and fully stripped carbon density profiles. Here the radial transport was independent of poloidal angle; other simulations have also been done with poloidally dependent transport [2-53]. Recycling and power balance were used to match the outer divertor D_α and heat flux. Thus, the final particle and thermal diffusivity profiles can be compared to interpret the effect of lithium on cross-field transport coefficients. No attempt was made to determine a particle or thermal pinch; hence, the diffusivities should be interpreted as "effective" cross-field transport coefficients. The full procedure is described elsewhere [2-50,2-54], and summarized below.

The peak value of the lower, outer divertor D_α profiles [2-55] was used to constrain the divertor recycling coefficient, R_p. The reference ELMy discharge peak D_α emission is matched using $R_p \sim 0.98$, while the ELM-free peak D_α emission was matched with $R_p \sim 0.90$. The trend is nearly identical to previous results [2-50] that did not model the impurities beyond a sensitivity assessment. In addition, these calculations matched the peak divertor heat flux from infrared thermography [2-56,2-57], which effectively constrain the separatrix n_e and T_e values. The match to the available profile data for the reference ELMy discharge #129015 and the ELM-free discharge #129038 was quite good [2-50]. Both sets of simulations reproduce the data sufficiently well to assess the effect of lithium on the inferred effective radial transport rates.

Figure 2-16 shows the results of the 2-D modeling [2-54] for four of the discharges from the scan: a reference ELMy discharge based on composite ELM-synchronized plasma profiles (from #129015-019), an ELMy discharge near the transition to ELM-free operation (#129030), the subsequent ELM-free discharge (#129031), and the penultimate ELM-free discharge (#129038). Panel (a) shows the match to the n_e profiles, panel (b) shows the required effective particle diffusion coefficient, D_e^{eff}, panel (c) shows the match to the T_e profile, while panel (d) shows the corresponding effective electron thermal diffusivity, χ_e^{eff}. The simulations show that both the D_e^{eff} and χ_e^{eff} from the reference ELMy discharge had a minimum in the vicinity of the steep gradient region from $0.94<\psi_N<1$, indicative of the H-mode transport barrier. With increasing discharge number and lithium coatings, both the D_e^{eff} and χ_e^{eff} decreased gradually in the region from $0.8<\psi_N<0.94$, until the minimum transport level extended to $\psi_N=0.8$, the inner domain of the calculation. The D_e^{eff} and χ_e^{eff} values actually increased modestly from $0.94<\psi_N<1$, and the D_e^{eff} dropped in the scrape-off layer, i.e. $\psi_N>1$. The resilience of the T_e gradients from $0.94<\psi_N<1$ in panel (c) is notable, raising the prospect of transport regulation via electron temperature gradient (ETG) modes [2-54], as discussed below. In the next few paragraphs, we discuss the inferred changes to the edge turbulence from reflectometery, and evaluate both ETG modes and paleoclassical transport from the perspective of the observed transport changes with lithium.

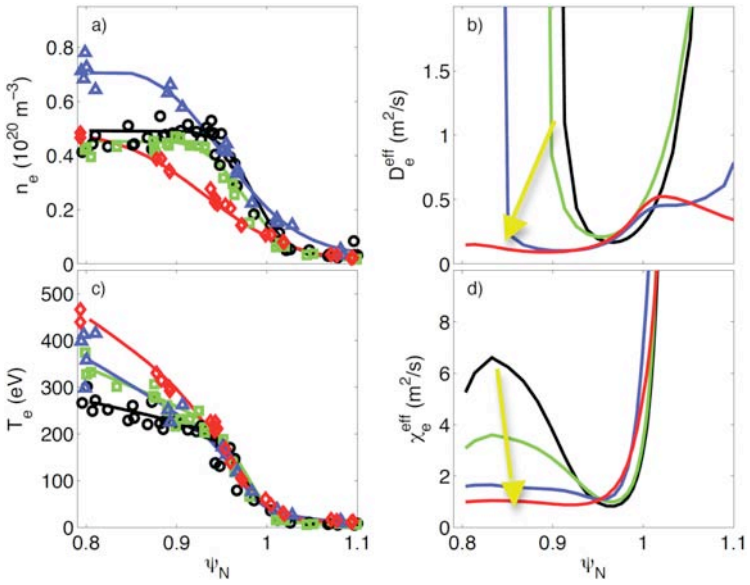

Fig. 2-16. Modeling results for four discharges during the lithium deposition scan: (a) n_e, (b) T_e, (c) effective cross-field electron diffusion coefficient $D_e^{eff,}$ and (d) effective cross-field electron thermal diffusivity, χ_e^{eff}. The yellow arrows indicate the trend with increasing lithium deposition. [Canik, PoP 2011]

NSTX is equipped with reflectometers [2-58] sensitive to n_e fluctuations in the pedestal region. The system used in these studies operates at five fixed frequencies (30, 35, 42, 44.5, 50 GHz), with quadrature detection used to separate the phase and amplitude of the reflected signals. These reflectometer frequencies allow density fluctuations to be probed from approximately the pedestal top ($n_e^{cutoff} \sim 3.1x10^{19}$ at 50 GHz) to near the separatrix ($n_e^{cutoff} \sim 1.1x10^{19}$ at 30 GHz). As is evident from the raw signals [2-54], the pre-lithium discharges show very strong amplitude fluctuations in the reflected signals due to scattering near the cutoff surface, whereas in the with-lithium discharges, this effect is much smaller and fluctuations are mainly in the phase. This alone implies a change in the turbulence characteristics, although the change in the n_e profile near the cutoff layer also needs to be taken into consideration. A quantitative estimate can be made for the change in the RMS density fluctuation level $\delta n/n$, using some assumptions about the underlying turbulence and a synthetic diagnostic model. The inferred profiles of $\delta n/n$ in the pre-lithium and with-lithium discharges are shown in Fig. 2-17. While this allows a comparison of the fluctuation level profiles between the pre- and with-lithium cases, it should be noted that the precise magnitude in the pre-lithium case remains somewhat uncertain given the assumptions required in making this estimate. Note that the innermost pre-lithium measurements are made in the inner part of the pedestal, near the top of the density pedestal, and these overlap with the outer channels for the with-lithium case. In this region of overlap, a reduction of density fluctuations from on the order of 10% pre-lithium to ~1% with lithium is inferred.

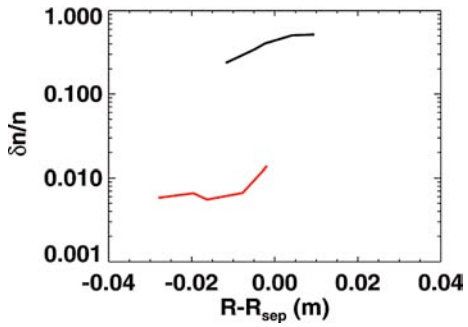

Fig. 2-17. Comparison of n_e fluctuation levels from reflectometry between pre-lithium (black) and with-lithium (red) discharges. [Canik, PoP 2011]

While the interpretive modeling and fluctuation measurements described above indicate that transport and turbulence are significantly reduced with lithium near the pedestal top, the underlying mechanisms for this reduction are under investigation. One candidate mechanism that can be considered is turbulence caused by ETG modes.

The critical gradient for ETG mode onset is given roughly [2-59] by

$$\left[\frac{R}{L_{T_e}}\right] = \max\left[\eta_e^{crit}\frac{R}{L_n}, \left(1+\frac{Z_{eff}T_e}{T_i}\right)\bullet\left(1.33+1.91\hat{s}/q\right)\cdot F_G\right] \quad ,$$

where R is the major radius, L_{Te} and L_n are the temperature and density gradient scale lengths, $\eta_e = L_n/L_{Te}$, $\hat{s}$ is the magnetic shear, q is the safety factor, and F_G represents additional variations due to the MHD equilibrium that are not easily quantifiable for spherical torus parameters. The critical value η_e^{crit} is typically ~ 0.8 based on core ETG calculations, although a value of 1-1.25 was found [2-60] in the edge of ASDEX-Upgrade plasmas. For both of the NSTX discharges [2-54], the n_e gradient is strong outside of ψ_N~0.95, so that the ETG threshold can be expected to be set by the n_e gradient. The measured T_e gradient scale lengths are comparable to the n_e scale lengths in this region, suggesting that ETG may play a role in the fairly stiff T_e profiles observed near the separatrix. Near the pedestal top, the n_e gradients are weaker in both the pre- and with-lithium cases, making the critical T_e gradients more sensitive to Z_{eff}, T_e/T_i, and the q-profile. Based on this simple analysis, it does appear that ETG may be a contributor to the total transport at least in the with-lithium case, where only small low-k fluctuations are measured.

Another possible mechanism for setting the edge transport rates is paleoclassical transport, which is driven by the diffusion of poloidal magnetic flux [2-61,2-62]. Paleoclassical transport depends strongly on the neoclassical resistivity, and so is sensitive to the T_e and Z_{eff} profiles. Recently, a model of the pedestal structure based on paleoclassical transport within the pedestal and ETG transport at the pedestal top has been proposed, and predictions were made for the electron heat and particle transport rates [2-63].

Profiles of χ_e from the paleoclassical model are shown in Fig. 2-18, along with the values from experiments, for the pre- and with-lithium cases [2-54]. Near the separatrix, the paleoclassical predictions reflect much of the structure seen in experiment, with χ_e being similar in magnitude and increasing with radius as ψ_N approaches 1.0. Furthermore, the paleoclassical values of χ_e also show the modest increase in the with-lithium case compared to pre-lithium observed near the separatrix. In the pedestal-top region, the experimental χ_e is significantly higher than the paleoclassical value for the pre-lithium case, suggesting that another transport mechanism dominates; in the with-lithium case, the agreement with paleoclassical remains good across the entire edge region.

The paleoclassical χ_e prediction [2-63] is proportional to the magnetic field diffusivity D_η induced by the parallel neoclassical resistivity. The neoclassical resistivity contains contributions from both the classical (Spitzer) resistivity (which depends on $Z_{eff}/T_e^{3/2}$), and parallel electron viscosity effects (which depend primarily on collisionality). In the steep gradient region ($0.94<\psi_N<1.0$) the density is reduced by ~ 50% in the with-lithium case. This reduces the collisionality and increases the viscosity effects by similar factors, and thereby increases the neoclassical resistivity (and χ_e) by ~40%, as shown in Fig. 2-18. For $\psi_N<0.9$, the competing effects of larger Z_{eff} but higher T_e with lithium largely cancel and cause the pre- and with-lithium cases to have similar neoclassical resistivity, and hence χ_e magnitudes as seen in Fig. 2-18.

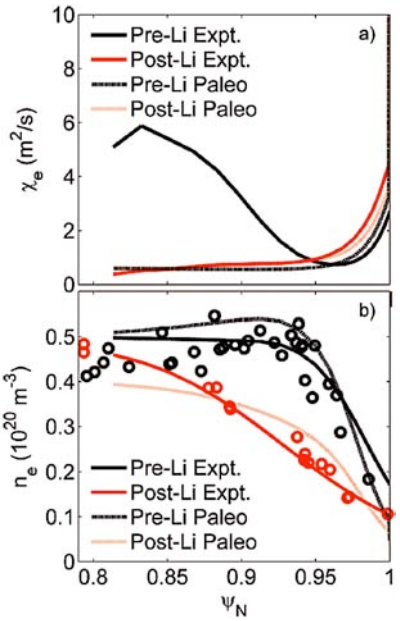

Fig. 2-18. Experimental and paleoclassical values of a) χ_e^{eff} and b) n_e profile for pre- (black) and with-lithium (red) discharges. [Canik, PoP 2011]

The n_e profile can also be predicted using the paleoclassical model; note that a strong inward particle pinch is predicted that nearly balances outward diffusion, so it is more straightforward to compare the density profile directly rather than diffusivities. Figure 2-18 compares [2-54] the measured and predicted paleoclassical edge n_e profiles. The paleoclassical n_e profile is scaled so that the average edge density from the model matches the magnitude of the experimental data; note that the paleoclassical model predicts the profile shape only, and not the magnitude. Again, the paleoclassical model captures the experimental trends going from pre-lithium to with-lithium, with the n_e pedestal widening in the with-lithium case, with a reduced gradient within the pedestal. In this application of the paleoclassical model, the n_e profile shape is determined by the resistivity profile only; the particle source due to neutrals is neglected, since this is expected to play a small role in the model. We now move to discuss stability analysis of the discharge sequence.

Detailed stability analysis was performed for most of the discharges of this sequence [2-36] with the ELTE code [2-5,2-6]. These calculations showed [2-36] that the ELMy discharges were all close to the current-driven kink/peeling mode boundary within our ability to reconstruct the profiles, while the ELM-free discharges were uniformly farther from their kink/peeling mode stability boundaries. To perform the stability analysis, free boundary equilibria were calculated using EFIT constrained by the fit pressure profiles, and by current profiles calculated using the Sauter neoclassical formula for the bootstrap current [2-64]. While the lack of an edge current measurement is a major source of uncertainty in the stability analysis, we note that the neoclassical value was found to be in agreement with lithium-beam measurements [2-65] on DIII-D. To map out the stability boundary, additional fixed boundary model equilibria were calculated with variations in the edge current and pressure gradient.

The stability criterion is commonly given by $\gamma_0/(½\ \omega_{*i})$, where γ_0 is the linear growth rate of the peeling-ballooning mode and ω_{*i} is the diamagnetic drift frequency. Contour plots of $\gamma_0/(½\ \omega_{*i})$ versus normalized edge current and normalized pressure gradient are shown in Fig. 2-19 for four discharges selected for especially sharp transitions in ELM behavior [2-36]. The crosshairs are centered on the experimental equilibrium and represent relative error in normalized edge current and normalized pressure

gradient of 30% and 20%, respectively. The red region was unstable with $\gamma_0/(\frac{1}{2}\ \omega_{*i}) > 0.15$; the blue region was stable with $\gamma_0/(\frac{1}{2}\ \omega_{*i}) < 0.05$. We note that $\gamma_0/(\frac{1}{2}\ \omega_{*i}) = 1$ marked the stability boundary to intermediate-*n* peeling-ballooning modes [2-47] in DIII-D, but the stability criterion has been found to be an order of magnitude lower for low-*n* kink/peeling modes [2-10,2-66] in NSTX. In all of the discharges in this experiment, the equilibrium was closer to the current driven kink/peeling stability boundary, with the pressure driven ballooning boundary well off to the right hand side of the axis. In Fig. 2-19(a), a pre-lithium ELMy discharge was very close to the stability boundary. In Fig. 2-19(b) the stability boundary was much farther away for a discharge in which ELMs had been suppressed by intermediate lithium coatings. The improved stability was partly due to reduction of the edge current. More importantly, the stability boundary shifted to the left and upward; even with edge current comparable to the value in panel (a), this discharge would have been more stable. This shift in stability was probably because the pressure gradient and current peaks were shifted inward away from the separatrix. Figure 2-19(c) shows a discharge in which ELMs returned, despite continued lithium deposition. Here, the stability boundary was very similar to the pre-lithium case, though the discharge had a significantly larger edge current and pressure gradient. In the thick lithium coating, ELM-free discharge, [Fig. 2-19(d)], the edge current was about the same as the other ELM-free case, but the pressure gradient was lower, which in and of itself is destabilizing for kink/peeling modes. However, the stability boundary shifted to the left and up as the pressure gradient and current peaks shifted inward, making this discharge robustly stable. To summarize: the ELM-free equilibria were farther from their stability boundaries than the ELMy discharges. In the ELM-free discharges, the stability boundaries shifted to the left and up as the edge pressure gradient and current peaks widened and shifted away from the separatrix.

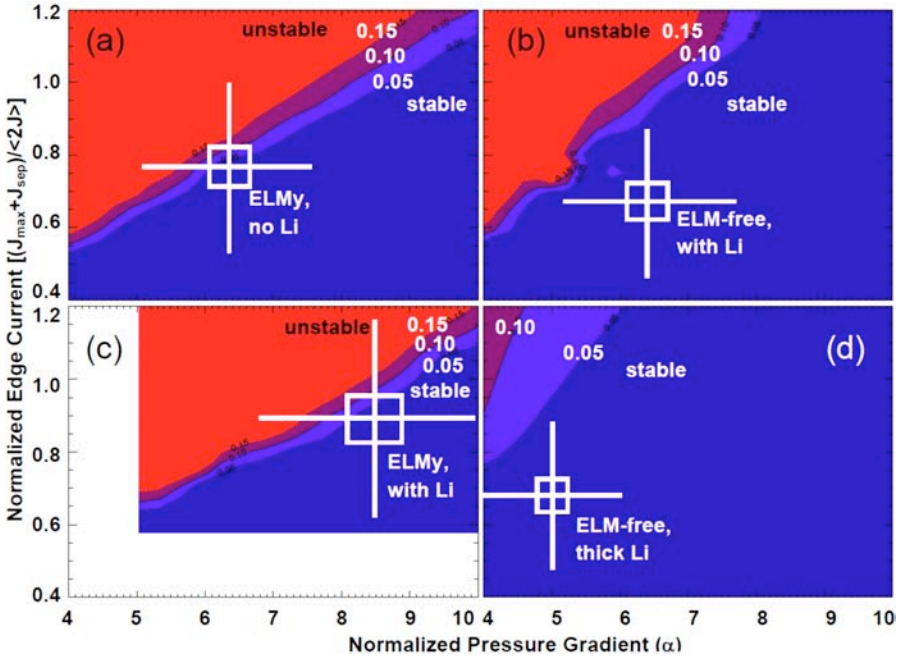

Fig. 2-19. Edge stability diagram for four discharges from the discharge sequence as computed with ELITE: ELM-free plasmas were farther from the kink/peeling stability boundary. Equilibria are from (a) a pre-lithium ELMy discharge, (b) an intermediate lithium discharge with reduced ELM activity, (c) an intermediate lithium discharge where ELMs have returned (no converged kinetic fits in blank space), and (d) a high lithium deposition, ELM-free discharge. Note that the axes have suppressed zeros. [Boyle, PPCF 2011]

The above trend is clear at the endpoints [2-36]: other no-lithium discharges in this experiment were similar to Fig. 2-19(a), and thick lithium discharges from other NSTX experiments were similar to Fig. 2-19(d). Other intermediate lithium discharges in this experiment were more similar to Fig. 2-19(b)

than Fig. 2-19(c). That is, their edge currents were ~20-40% below the stability boundary, whether or not they were ELMy. Given the number of steps involved in calculating the stability, it is unsurprising that it is difficult to resolve the precise transition from ELMy to ELM-free. However, it is clear that in general, ELM-free equilibria were farther from their stability boundaries than the ELMy discharges.

The reason for the enhanced stability is not simply a reduction in the peak pressure gradient; indeed, the peak pressure gradient was actually higher in some of the ELM-free discharges. The primary reason for the movement of the stability boundary is that the peak pressure gradient and calculated edge bootstrap current peak were shifted inboard farther from the separatrix, which is stabilizing for the peeling mode drive. Note that the low aspect ratio of the NSTX naturally results in the ballooning mode drive being insignificant for these ELMs.

To summarize, we have shown that many plasma parameters change nearly continuously with increasing lithium coatings in this section. Specifically, the divertor recycling was gradually reduced with increasing lithium wall coatings in NSTX, and the plasma stored energy and normalized τ_E all increased, while the core T_e and P_e profiles became less peaked with increasing lithium wall coatings. The inferred χ_e dropped sharply at r/a ~ 0.7. Interpretive 2-D simulations showed that the near-separatrix D_e^{eff} and χ_e^{eff} were reduced substantially from $0.8<\psi_N<0.94$, i.e. the H-mode pedestal effectively expanded to the inner boundary of the calculation in the ELM-free discharge with lithium. The most dramatic changes to the profiles were in the pedestal region, where the n_e and P_e profile widths doubled. Interestingly, the edge T_e gradient remained approximately constant in the H-mode barrier region, but increased just inside the top of the pedestal with increasing wall coatings. The ion pressure profile was changed only modestly; hence, the total pressure profile reflected the modification of the electron pressure profile, whose peak gradient and associated bootstrap current moved farther from the separatrix. These profile changes were clearly correlated with the observed gradual suppression of ELMs with increasing lithium, with reduced drive for the kink/peeling mode being the key stabilizing mechanism.

2.4. Enhanced Pedestal H-mode Characterization

The energy confinement multiplier relative to ITERH98y2 scaling, i.e. τ_E/τ_E^{H98y2}, typically obtained in spherical tokamaks with boron wall coatings is typically 0.8-1.0, albeit with different dependences than the international scaling [2-67]. The deployment of lithium wall coatings has helped [2-30,2-40,2-68] to increase τ_E/τ_E^{H98y2} up to 1.1-1.2*H98y2 in NSTX, but still short of the desired value for some future attractive STs designs. In general, improving the τ_E has merit for nearly all fusion concept designs, provided the scenarios do not introduce other problematic instabilities or excessive confinement of the helium ash and/or impurities.

Recently a spontaneous transition in H-mode discharges that results in a ~ 50% increase in τ_E was observed in NSTX. This increase is in addition to the 40-50% τ_E improvement provided by ELM-free lithium operation [2-10]. The improvement in τ_E is caused by a marked increase in the edge pedestal electron and ion temperatures (T_e, T_i), as well as a substantial broadening of the H-mode pedestal width, which has been referred to as the "Enhanced Pedestal" (EP) H-mode [2-69,2-70]. The electron density on the other hand, is observed to flatten. The EP H-mode is particularly interesting to study because of this apparent separation of particle and thermal transport channels.

The EP H-mode phase is triggered following certain large edge-localized modes (ELMs), either naturally occurring or those induced by applied 3D fields [2-71]. The increase in the pedestal T_e, T_i leads to a high pedestal pressure and relatively low pressure peaking factor, which increases the stability limit to resistive wall modes [2-72,2-73]. Furthermore, the wider pedestals lead to high edge bootstrap currents, low inductive flux consumption, and correspondingly high non-inductive fraction.

Historically EP H-modes have been difficult to achieve reliably. However analysis of recent data has uncovered a high I_p, low q95 scenario for reliable, albeit short-lived, EP H-modes. An example of this scenario is shown in Fig. 2-20; the EP H-mode was triggered by the first ELM at t1, and terminated at time t2. The line-average density ramp was markedly eliminated during this phase.

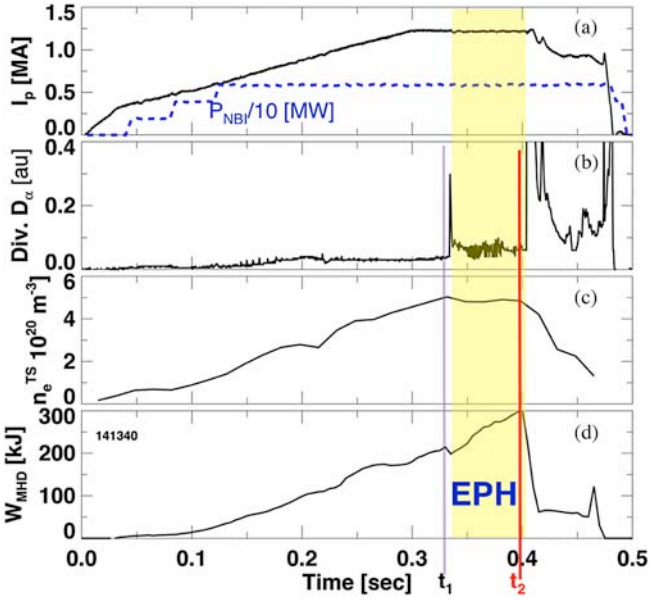

Fig. 2-20. Evolution of a high I_p EP H-mode: (a) plasma current and NBI power (b) divertor D_α emission, (c) line-average density from Thomson scattering (d) and plasma stored energy. The EP H-mode phase is indicated in yellow.

Figure 2-21 compares the plasma profiles just before the beginning and end of the EP H-mode phases. The characteristic increase in T_e and T_i was observed, as was a substantial drop in the edge n_e. Finally the signature change in the toroidal rotation (V_{tor}) profile, namely an increase in the edge shear with a zero crossing at the edge q=3 surface, is clearly seen.

Figure 2-22 shows that magnetic fluctuations were enhanced in the Mirnov data during the EP H-mode shown above. An upward chirping set of coherent modes is clearly visible in the early part of EP H-mode; in general, magnetic fluctuations increased in amplitude. In addition, density fluctuations measured by the BES diagnostic also increased. We speculate that these fluctuations might be responsible for the apparent separation of particle and thermal transport channels.

Looking ahead to NSTX Upgrade, research on EP H-mode will include research on reliable triggering, and pulse length extension via β feedback. In addition, in-depth analysis of the turbulence characteristics, including comparison with the I-mode confinement regime [2-74,2-75], is planned.

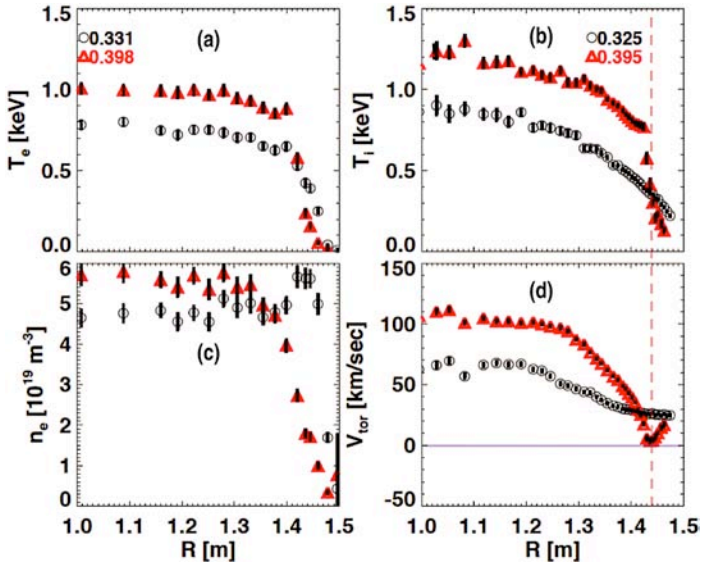

Fig. 2-21. Profile comparison during normal H-mode (black) and EP H-mode phases (red): (a) T_e, (b) T_i, (c) n_e, (d) V_{tor} from high I_p EP H-mode.

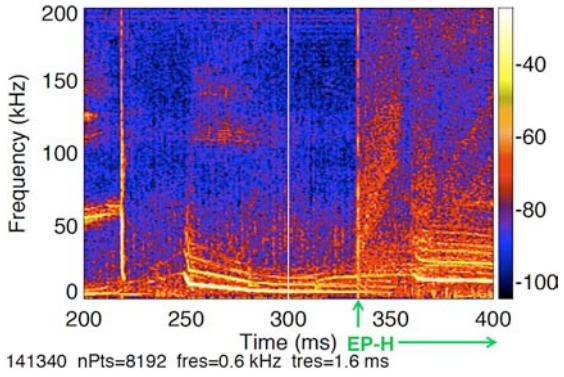

Fig. 2-22. Spectrogram of magnetic fluctuations from Mirnov data, showing increased fluctuations during EP H-mode phase.

References for Section 2

[2-1] Wagner F., et al. Phys. Rev. Lett. **49**, 1408 (1982).

[2-2] Zohm H. Plasma Phys. Control. Fusion **38**, 105 (1996).

[2-3] Loarte A., et al. Proc. 22nd Fusion Energy Conf., Geneva, SZ, 13-18 Oct. 2008 IT/P6 (2008).

[2-4] Connor J.W., et al. Phys. Plasmas **5**, 2687 (1998).

[2-5] Snyder P.B., et al. Phys. Plasmas **9**, 2037 (2002).

[2-6] Wilson H.R., et al. Phys. Plasmas **9**, 1277 (2002).

[2-7] Snyder P.B., H.R. Wilson, T.H. Osborne and A.W. Leonard Plasma Phys. Control. Fusion **46**, A131 (2004).

[2-8] Maingi R., et al. Nucl. Fusion **45**, 1066 (2005).

[2-9] Kirk A., et al. Plasma Phys. Control. Fusion **46**, 551 (2003).

[2-10] Maingi R., et al. Phys. Rev. Lett. **103**, 075001 (2009).

[2-11] Diallo A., et al. Nucl. Fusion **51**, 103031 (2011).

[2-12] Snyder P.B. Nucl. Fusion **49**, 085035 (2009).

[2-13] LeBlanc B.P., et al. Rev. Sci. Instrum. **74**, 1659 (2003).

[2-14] Bell R.E., et al. Phys. Plasmas **17**, 082507 (2010).

[2-15] Lao L.L., et al. Nucl. Fusion **25**, 1611 (1985).

[2-16] Sabbagh S.A., et al. Nucl. Fusion **41**, 1601 (2001).

[2-17] Kirk A., et al. Plasma Phys. Control. Fusion **49**, 1259 (2007).

[2-18] Maggi C.F., et al. Nucl. Fusion **47**, 535 (2007).

[2-19] Groebner R.J., et al. Nucl. Fusion **49**, 045013 (2009).

[2-20] Kirk A., et al. Plasma Phys. Control. Fusion **51**, 065016 (2009).

[2-21] Groebner R.J., et al. Nucl. Fusion **49**, 085037 (2009).

[2-22] Burckhart A., et al. Plasma Phys. Control. Fusion **52**, 105010 (2010).

[2-23] Maggi C.F. Nucl. Fusion **50**, 066001 (2010).

[2-24] Snipes J., E.S. Marmar, J.L. Terry J. Nucl. Mater. **196-198**, 686 (1992).

[2-25] Mansfield D.K., et al. Nucl. Fusion **41**, 1823 (2001).

[2-26] Majeski R., et al. Phys. Rev. Lett. **97**, 075002 (2006).

[2-27] Apicella M., et al. J. Nucl. Mater. **363-365**, 1346 (2007).

[2-28] Sánchez J., et al. J. Nucl. Mater. **390-391**, 852 (2009).

[2-29] Kugel H.W., et al. J. Nucl. Mater. **363-365**, 791 (2007).

[2-30] Kugel H.W., et al. Phys. Plasmas **15**, 056118 (2008).

[2-31] Bell M.G., et al. Plasma Phys. Control. Fusion **51**, 124054 (2009).

[2-32] Kugel H.W., et al. J. Nucl. Mater. **390-391**, 1000 (2009).

[2-33] Maingi R., et al. Nucl. Fusion **51**, 063036 (2011).

[2-34] Maingi R., et al. Nucl. Fusion **45**, 264 (2005).

[2-35] Mansfield D.K., et al. J. Nucl. Mater. **390-391**, 764 (2009).

[2-36] Boyle D.P., et al. Plasma Phys. Control. Fusion at press (2011).

[2-37] Hawyrluk R.J. Phys. of Plasmas Close to Thermonuclear Cond. **1**, 19 (1980).

[2-38] Goldston R.J., et al. J. Comput. Phys. **43**, 61 (1981).

[2-39] Maingi R., et al. Phys. Rev. Lett. **107**, 145004 (2011).

[2-40] Ding S., et al. Plasma Phys. Control. Fusion **52**, 015001 (2010).

[2-41] Menard J.E. Nucl. Fusion **43**, 330 (2003).

[2-42] Sabbagh S.A. Nucl. Fusion **46**, 635 (2006).

[2-43] Kaye S.M., M. Greenwald, U. Stroth Nucl. Fusion **37**, 1303 (1997).

[2-44] Canik J.M., A.C. Sontag, R. Maingi, R. Bell, D.A. Gates Nucl. Fusion **51**, 064016 (2010).

[2-45] Canik J.M., et al. Phys. Rev. Lett. **104**, 045001 (2010).

[2-46] Soukhanovskii V.A., et al. Nucl. Fusion **51**, 012001 (2011).

[2-47] Osborne T.H., et al. J. Phys.: Conf. Series **123**, 012014 (2008).

[2-48] LeBlanc B. Nucl. Fusion **44**, 513 (2004).

[2-49] Groebner R.J. and T.H. Osborne Phys. Plasmas **5**, 1800 (1998).

[2-50] Canik J.M., et al. J. Nucl. Mater. at press (2011).

[2-51] Schneider R. Contrib. Plasma Phys. **46**, 3 (2006).

[2-52] Reiter D.J. Nucl. Mater. **196-198**, 80 (1992).

[2-53] Smirnov R.D., et al. Contributions to Plasma Physics **50**, 299 (2010).

[2-54] Canik J.M., et al. Phys. Plasmas **18**, 056118 (2011).

[2-55] Soukhanovskii V.A. Rev. Sci. Instrum. **75**, 4320 (2004).

[2-56] Mastrovito D.M. Rev. Sci. Instrum. **74**, 5090 (2003).

[2-57] Maingi R., et al. J. Nucl. Mater. **363-365**, 196 (2007).

[2-58] Kubota S., et al. Bull. Am. Phys. Soc. **53**, 188 (2008).

[2-59] Jenko F., W. Dorland G.W. Hammett Phys. Plasmas **8**, 4096 (2001).

[2-60] Jenko F., et al. Phys. Plasmas **16**, 055901 (2009).

[2-61] Callen J.D. Phys. Rev. Lett. **94**, 055002 (2005).

[2-62] Callen J.D., C.C. Hegna A.J. Cole Phys. Plasmas **17**, 056113(2010).

[2-63] Callen J.D., J.M. Canik S.P. Smith Phys. Rev. Lett. submitted (2011).

[2-64] Sauter O., C. Angioni, Y.R. Lin-Liu Phys. Plasmas **6**, 2834 (1999).

[2-65] Thomas D.M. et al. Phys. Rev. Lett. **93**, 065003 (2004).

[2-66] Sontag A.C., et al. Nucl. Fusion **51**, 103022 (2011).

[2-67] Kaye S.M., R.E. Bell, D. Gates Phys. Rev. Lett. **98**, 175002 (2007).

[2-68] Bell R.E. Phys. Plasma submitted (2010).

[2-69] Maingi R., et al. Phys. Rev. Lett. **105**, 135004 (2010).

[2-70] Maingi R., et al. J. Nucl. Mater. **390-391**, 440 (2009).

[2-71] Canik J.M., et al. Phys. Rev. Lett. **104**, 045001 (2010).

[2-72] Lazarus E.A. Phys. Rev. Lett. **77**, 2714 (1996).

[2-73] Sabbagh S.A., E.D. Fredrickson, D.K. Mansfield Proc. 16th Internatonal Conf. on Fusion Energy, Montreal, CA, 7-11 Oct. 1996 AP2 (1996).

[2-74] McDermott R.M., et al. Phys. Plasmas **16**, 056103 (2009).

[2-75] Whyte D.G., et al. Nucl. Fusion **50**, 105005 (2010).

3. DIII-D FINAL FY11 JRT REPORT (R.J. Groebner for DIII-D Group)

3.1. Executive Summary

In support of the "DOE FY11 Joint Research Target on Pedestal Physics", a focussed research program in FY11 identified a set of physics processes proposed to control the pedestal structure, identified models for these processes, devised tests of these models and carried out experiments in the FY11 DIII-D experimental campaign. A rich data set was obtained for testing models of kinetic ballooning modes, paleoclassical transport, electron temperature gradient modes and neutral fueling. Some initial analysis has been performed, particularly by evaluating the EPED and paleoclassical models over a significant portion of the new data set, and plans have been developed for analyzing the full data set.

3.2. Introduction

The DIII-D pedestal program has had a strong focus on testing pedestal models for several years. A key result from recent studies is that there is a weak or no dependence of the pedestal width on ρ^*, the ion gyroradius normalized to machine size. This result is based on a coordinated experiment between JET and DIII-D in which ρ^* was varied by a factor of four. This result contradicts a major theoretical paradigm for pedestal width, namely that ExB shear suppression of long wavelength drift turbulence should produce a ρ^* scaling of pedestal width. Thus, there is a need to identify other physics processes that might be setting the pedestal width and height and to test models of these processes. Section II briefly discusses the process by which models were identified for testing, Section III is a description of the DIII-D experimental pedestal plan developed for the FY11 campaign and section IV gives a summary of experimental results for each of the models tested. A bibliography of recent and planned publications and presentations is appended to the end of the report.

3.3. Identifying Testable Models

The goal of the DIII-D pedestal program for FY11 was to make substantial progress in identifying physics processes that are important in controlling the pedestal structure. Addressing this goal requires testing models of these processes. An important criterion for selecting models to test was that the models provide quantitative predictions for comparison with experiment. Some of the models chosen for testing have this capability; for some of the models that were selected, it is anticipated that current developments of the models will soon provide this quantitative capability.

A significant effort was expended to solicit input from the US theoretical and modeling communities for appropriate models to test. A major source of input was the "DIII-D Pedestal Transport Workshop", held on February 17-18, 2010 at General Atomics. Ideas were also solicited from the Edge Coordinating Committee, from the US Transport Task Force, in the DIII-D Research Opportunities Forum and in other ways.

3.4. FY11 Experimental Pedestal Plan

Table 3-1 lists the pedestal physics processes and associated experimental tests that became the basis for the FY11 experimental pedestal campaign.

Table 3-1
Physics Processes and Tests of Processes used to Formulate DIII-D Experimental Pedestal Plan

Physics Process	Proposed Effect	Control Parameters	Tests (Measurements plus Theory)
Kinetic Ballooning Modes (KBM)	Limit the total pedestal pressure gradient	S (magnetic shear) α (pressure gradient)	- ∇P clamped to predicted critical gradient? - Radial correlation length of low-k fluctuations scales with $\beta_{pol}^{1/2}$?
Paleoclassical Transport	Irreducible transport limit to pedestal ∇T_e and ∇n_e	Magnetic diffusivity D_η heating power	- $n_e(\rho)\ D_\eta(\rho)$ ~ constant in pedestal? At predicted value? - ∇Te ~ constant in pedestal? At predicted value?
Electron Temperature Gradient (ETG) Modes	Limit ∇T_e in pedestal and on pedestal top	η_e	- η_e clamped at critical value? - High-k fluctuations increase as L_{Te} is increased?
Particle fuelling	Control pedestal density profile, particularly the width	Neutral depth	- Particle pinch builds pedestal density profile? - Can D3D match ped profiles in a machine with very different fuelling characteristics?

Five experiments were designed and carried out to test these processes. These experiments with their DIII-D designations were:

- 21-1 Test models for limiting pedestal gradients (KBM).
- 21-2 Test models for limiting pedestal gradients (ETG, Paleoclassical).
- 21-3 Test role of neutral fueling vs density pinch in density pedestal with opaque SOL.
- 21-4 Test role of neutral fueling vs density pinch in density pedestal with dimensionless match to C-Mod.
- 21-5 Are HFC modes a signature of linear KBM physics?

These experiments have all been successfully performed and rich data sets have been obtained. These data sets include edge pedestal profile measurements from the upgraded Thomson Scattering system, which has provided substantially improved spatial resolution in the pedestal, due to a doubling of the chord density, and higher time resolution, due to the addition of new lasers. These data provide significant improvements in the quality and accuracy of pedestal profiles and are a major benefit of the FY11 campaign. Strong emphasis was placed on obtaining fluctuation data and good data sets were obtained for most of the experiments. Other required data, such as ion profiles, profile reflectometry and radiated power, were obtained routinely. For some experiments, data was obtained from divertor and scrape-off layer diagnostics for purposes of 2D/edge modeling.

In addition to using the diagnostic capability of DIII-D, these experiments covered a wide operating space and also exploited much of the flexibility of the machine. These experiments included operation at high current (2 MA), operation over a wide range of plasma current and toroidal field, operation over a wide range of shapes, use of shaping capability to enhance the data from one or more diagnostics, use of ECH heating, use of NBI heating, use of the flexibility of the NBI system to vary source voltages and duty cycles, use of counter as well as co-neutral beam injection and use of the cyropumps. Most experiments were operated in the Type-I ELMing regime. In addition, some data were obtained in the

QH-regime and an experiment was conducted in which the shape and pedestal dimensionless parameters were matched to a C-Mod ELMy experiment.

3.5. Experimental Results

Initial results of tests of the models and work remaining to be done will be presented here.

3.5.1. Kinetic ballooning modes.

The EPED pedestal model contains a width model derived from kinetic ballooning mode physics. Thus, testing the EPED model also tests a kinetic ballooning model. Most of the experiments that were performed will be useful for testing the EPED model and therefore KBM physics. Experiment 21-1 obtained data over a wide range of conditions and was designed as the most comprehensive test of the EPED model. An important result of this experiment is that it filled in a major gap in the previous data sets and provided good pedestal width data at high beta poloidal (Fig. 3-1). In the preliminary analysis of this experiment with the EPED model, the ratio of predicted to observed pedestal height is 1.13 ± 0.22 and the ratio of predicted to observed pedestal width is 1.00 ± 0.13. More refined analysis is underway and will be presented at the 2011 H-mode Workshop in Oxford, England and the 53rd Annual Meeting of the APS Division of Plasma Physics in Salt Lake City, Utah (DPP2011). *The focus of the ongoing analysis* will be on comparing the KBM width model within the EPED model with the new and improved pedestal measurements and particularly to compare the model predictions with recent high beta poloidal discharges, which are predicted to have wide pedestals.

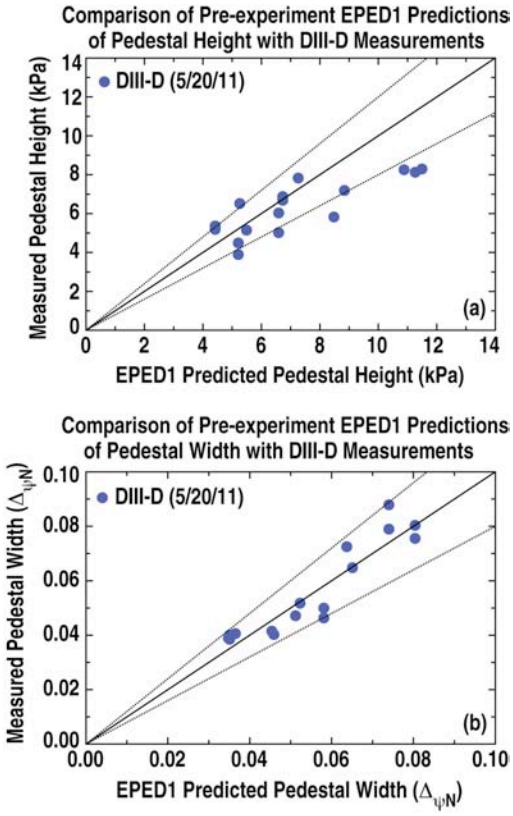

Fig. 3-1. Preliminary comparison of EPED1 predicted (a) pedestal height and (b) pedestal width to DIII-D observations in a pedestal experiment employing new high resolution Thomson scattering measurements in a scan of plasma current and magnetic field. This experiment obtained a significant amount of data at high pedestal beta poloidal and filled in a previous gap in measured widths between 0.06 - 0.08 in normalized psi. (To be presented by P.B. Snyder at 2011 APS/DPP meeting in Salt Lake City, UT.)

Testing of the EPED/KBM models was pushed into new regimes in at least two other experiments. Experiment 21-3, which used operation at plasma currents of 2 MA, provided the highest pedestal pressure to date in tests of these models. *Analysis of these data will explore* the limits of the KBM model for the high pedestal pressures. And, experiment 21-4, which produced H-mode plasmas to match the ELMy H-mode regime of C-Mod, allows for testing of the models in a unique shape and at low power, but it also will allow for good comparisons with complementary experiments in C-Mod (Fig. 3-2). *Analysis of this experiment is in progress* and will be presented at the 2011 H-mode Workshop. Preliminary results show agreement of the model with the data to within 20% or better. This analysis will examine the ability of the KBM model to provide a unified picture of widths in the joint C-Mod/DIII-D matched discharges.

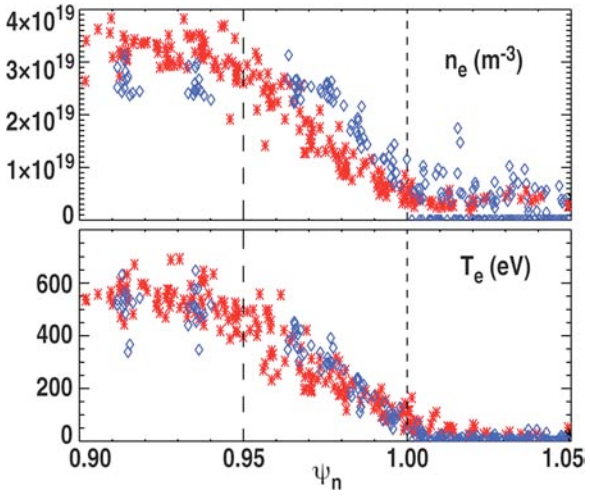

Fig. 3-2. Preliminary analysis showing nearly matched pedestals in C-Mod (blue diamonds) and DIII-D (red stars). The C-Mod data have been appropriately scaled to DIII-D temperatures and densities. The T_e pedestals overlay well. The DIII-D density pedestal is wider in flux space than the C-Mod density pedestal. There is a near match of both T_e and n_e at normalized psi ~ 0.95. (C-Mod data courtesy of J.W. Hughes.)

Data were also obtained to more directly test KBM physics. Experiment 21-5 was performed to generate high frequency coherent (HFC) modes, which were first observed in a QH-mode experiment in 2009. Detailed analysis of the first experiment, now published in PRL (Yan, Z., et al., PRL 107, 055004 (2011)), shows that the modes have several characteristics expected for linear kinetic ballooning modes. For instance, the HFC modes had a frequency expected for KBMs. In the new experiment, plasma conditions (particularly plasma current and toroidal field) were varied with the goal of varying the theoretical frequency for KBMs and then determining if the observed frequency tracked the predictions. A good data set was obtained and analysis will be done later this year. *The focus of the analysis* will be on determining if the observed fluctuations are consistent with theoretical modeling of linear KBMs and on the possible impact of such fluctuations in limiting the pedestal pressure gradient, at least in QH-mode plasmas.

3.5.2. Paleoclassical transport

An analytic theory, based on paleoclassical transport theory (Callen, J.D., Report UW-CPTC 11-4, submitted to Phys. Plasmas), has been developed to make predictions of pedestal profile parameters, such as electron temperature gradient and the density profile. A key prediction of the model is that increasing power flow into the electrons in the pedestal will lead to an increasing electron temperature gradient. This is in contrast to predictions of critical gradient models, such as one based on electron temperature

gradient (ETG) turbulence, which predict that small scale turbulence limits the magnitude of the electron temperature gradient. Thus, experiment 21-2 was developed to test both paleoclassical and ETG models at the same time. This experiment used variations of both high power ECH heating and neutral beam heating to see if the T_e gradient could be increased with increasing power.

A good data set was obtained and the experiment showed that the T_e gradient could be increased somewhat with increases of heating power (Fig. 3-3). However, it appears likely that ELMs may have also played a role in limiting the maximum gradient that could be achieved within a discharge. So, this simple test of paleoclassical transport might not be as easy to interpret as originally expected. However, the predictions of the model have been evaluated for most of the pedestal experiments performed this year and these predictions have been compared to experiment (Fig. 3-4). This work is possible because analysis is available for edge profiles for a large number of discharges. In turn, techniques have been developed to rapidly evaluate the paleoclassical model predictions once the pedestal profiles are analyzed.

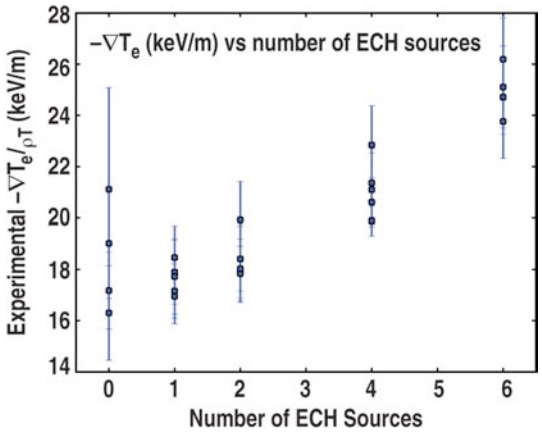

Fig. 3-3. Electron temperature gradient at pedestal midpoint as a function of number of ECH gyrotrons. ECH power was injected at normalized rho of about 0.8. Absorbed power from one gyrotron was about 0.5 MW. A constant power of 2.8 MW of neutral beam heating was applied for all cases. Increased ECH power increased the T_e gradient in the pedestal. During the scan, the pedestal n_e and its maximum gradient decreased due to density pumpout, which increased with number of gyrotrons.

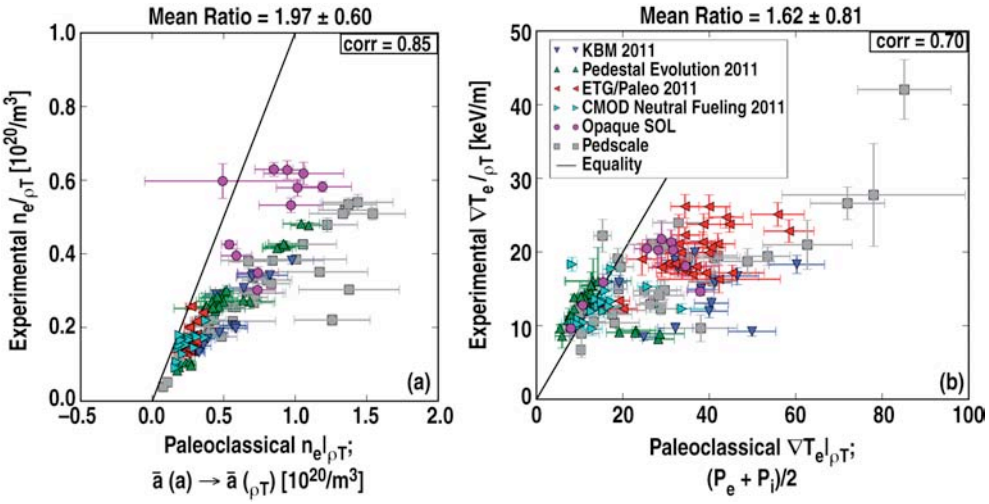

Fig. 3-4. Preliminary comparison of predictions from paleoclassical pedestal model to pedestal measurements shown for a number of experiments. a) Measured electron density at T_e symmetry point versus prediction from the model. Solid line is unity line. b) Measured gradient of T_e at symmetry point versus prediction from the model. Solid line is unity line. Initial analysis has been performed for most experiments in 2011. "Pedscale" refers to database from prior years. (To be presented by S.P. Smith at 2011 H-Mode Workshop in Oxford, England.)

The preliminary results show that most predictions of the T_e gradient are at or above the experimentally observed levels and that the predicted pedestal density is generally two times higher than measured. These results may mean that the paleoclassical model predicts a lower bound for electron thermal transport in the pedestal and some additional transport mechanism may also need to be invoked in many cases. This work has also shown that uncertainties in the electron power flow through the pedestal can be a significant source of systematic error in evaluating the paleoclassical model. Such uncertainties are thought to arise from uncertainties in the collisional ion-electron energy coupling term, which could arise from uncertainties in the temperature difference between ions and electrons. Thus, in Fig. 3-4, the power flow used in the model predictions is the average of the electron and ion power flow into the pedestal, as determined from the ONETWO transport code. This work will be reported at the H-mode Workshop in Oxford and DPP2011. *The focus of these studies* is on exploring whether the paleoclassical model predicts an irreducible minimum electron density and temperature transport in the steep gradient region of pedestals.

3.5.3. Electron temperature gradient turbulence

ETG turbulence has been proposed as a process to cause electron heat transport at the pedestal top and in the pedestal. Thus, it is a candidate for limiting the pedestal height, pedestal width and for limiting the pedestal electron temperature gradient. As noted under the discussion for paleoclassical transport, experiment 21-2 was done in which power variations, particularly with strong electron heating, were performed in order to determine if the pedestal electron temperature gradient showed evidence of reaching a "critical gradient" beyond which it would not evolve much, as would be expected for strong ETG turbulence. As noted previously, the pedestal Te gradient was increased with increased heating power (Fig. 3-3). Interpretion with gyrokinetic codes will be done to determine if the observed gradients are consistent with predictions of limits set by ETG transport.

As part of this experiment, measurements of density fluctuations were made at small scales, where ETG turbulence would be expected to manifest itself. Fluctuations were observed and the relative density fluctuation level showed a weak decrease with increased heating power (Fig. 3-5). This trend is opposite to simple expectations of ETG modes increasing in magnitude with increased heating power. However, theoretical guidance provided after the experiment was completed suggests that the dominant effect of increased power on ETG modes should be observed in the electron temperature fluctuations, which were not measured, and that the density fluctuations might not show much effect from increased power. In addition, a significant density pumpout was observed with ECH heating and the amount of pumpout increased with ECH power. Since the density gradient is expected to affect ETG stability, a proper interpretation of this experiment must be made by applying a gyrokinetic model to the actual experimental temperature and density profiles. This work will be done with codes such as GYRO and TGYRO. *The focus of these studies* is on determining if the observed changes in the T_e gradient and in observed fluctuation intensity are consistent with theoretical modeling of ETG modes and if the amplitude of the fluctuations correlate with increases in electron heat transport – at the pedestal top and/or within the pedestal.

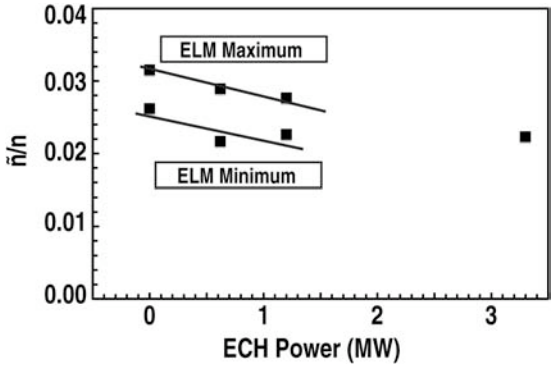

Fig. 3-5. RMS intensity of density fluctuations normalized to line averaged density from high-k backscattering measurement as a function of ECH heating power. Fluctuations were measured at a wavenumber of 35 cm^{-1} and originated from the outer 10-15 cm of the plasma edge. In addition to the ECH power shown, 2.3 MW of NBI power were applied in all conditions; total power varied from 2.3 to 5.6 MW. Data are shown early in ELM cycle ("ELM minimum") and late in ELM cycle ("ELM maximum").

3.5.4. Neutral fueling/density pinch

Fueling of the pedestal by neutral particles has been proposed as a mechanism to control the pedestal density structure, particularly its width. There has been mounting evidence that fueling cannot explain all experimental observations and that there might be a "density pinch". Experiment 21-3 was performed with the goal of getting a definitive result to determine if neutral fueling alone can explain the pedestal density profile or if some other mechanism must be invoked. This experiment required operating in conditions to obtain a scrape-off layer that was as opaque as possible to neutral particles, thereby eliminating neutral fueling as a significant physics mechanism inside the separatrix. These studies are also relevant for ITER where it is anticipated that the SOL will be very opaque to neutrals and there are concerns about how the pedestal and core plasma will be fuelled. The desired experimental conditions were obtained and the required data for edge modeling were obtained. A very high pedestal density was obtained but the electron density profile looked normal and the steep gradient region was mostly inside the separatrix (Fig. 3-6). Detailed 2D/edge modeling will be required to reconstruct the neutral source profiles that were achieved in the experiment and to see if the scrape-off layer was indeed opaque to neutrals. *This analysis has been initiated with a focus* on determining the degree of SOL opacity to neutrals that was achieved and whether the neutrals that do make it past the SOL provide significant fueling in the pedestal.

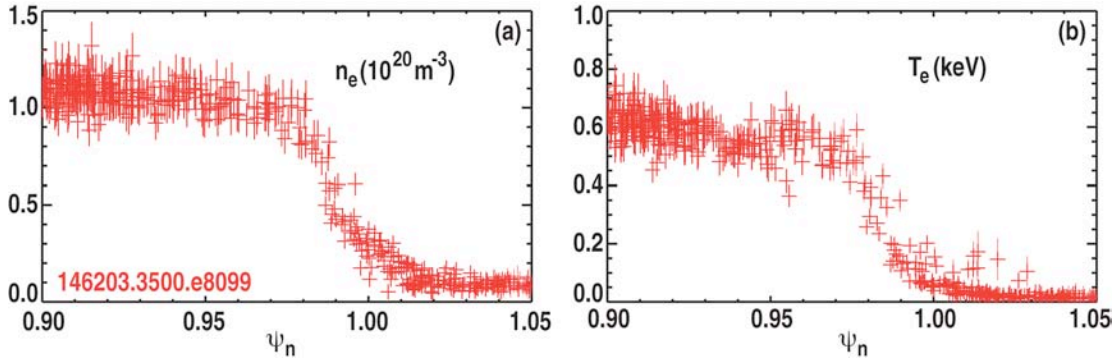

Fig. 3-6. Pedestal profiles for a) n_e and b) T_e in the "opaque SOL" experiment. Most of the steep gradient region of density pedestal lies inboard of separatrix. Edge/2D analysis is required to determine if the scrape-off layer was opaque to neutrals.

Experiment 21-4, in which DIII-D performed a dimensionless match to a pedestal from an ELMy H-mode discharge in C-Mod, is also expected to provide some data on the physics of the density pedestal formation. The appropriately scaled pedestal density profiles from the two machines can be compared to see if they overlay, as would be expected if neutral fueling were not important, or if they do not completely overlay, as would be expected if fueling were important. Preliminary analysis indicates that the scaled pedestal T_e profiles overlay well for the primary matched plasma current. The scaled density profile in DIII-D was generally wider in normalized flux space than in C-Mod (Fig. 3-2). Data were also obtained at lower plasma current and both scaled T_e and n_e profiles were matched closely. These different observations at different currents indicate that much more careful analysis is required to study the interplay of transport and fueling in forming the density pedestal in these experiments. Ideas for this analysis are being developed. *The focus of the analysis* will be on trying to assess if neutral fueling plays a significant role in determining the pedestal structure in comparably scaled C-Mod and DIII-D pedestals.

Bibliography for Section 3

The results reported here are from the FY11 experimental campaign. Much of this work will be reported in the next one to two years. The first reports will be at the 2011 H-Mode Workshop and at the 53rd APS-DPP meeting. Below is a list of relevant presentations that will be made at these meetings. Most of these presentations are expected to lead to published papers. This bibliography also includes papers published in 2010 and 2011 on recent DIII-D experimental results. Many of these results are directly related to the physics issues discussed here and the FY11 experimental campaign follows in a logical way from many of these results.

2010-2011 Pedestal Publications of Recent DIII-D Data:

Beurskens, M.N.A., "H-mode pedestal scaling in DIII-D, ASDEX Upgrade, and JET," Phys. Plasmas **18**, 056120 (2011); http://pop.aip.org/resource/1/phpaen/v18/i5/p056120_s1

Callen, J.D., et al., "Analysis of pedestal plasma transport," Nucl. Fusion **50**, 064004 (2010); http://iopscience.iop.org/0029-5515/50/6/064004

Groebner, R.J., et al., "Limits to the H-mode pedestal pressure gradient in DIII-D," Nucl. Fusion **50**, 064002 (2010); http://stacks.iop.org/0029-5515/50/064002

Osborne, T.H., et al., "Scaling of H-mode pedestal and ELM characteristics in the JET and DIII-D tokamaks," 2010 FEC – Korea - EXC2/1; http://www-pub.iaea.org/mtcd/meetings/PDFplus/2010/cn180/cn180_papers/exc_2-1.pdf

Owen, L.W., et al., "Comparing 1.5D ONETWO and 2D SOLPS analyses of inter-ELM H-mode plasma in DIII-D," Nucl. Fusion **50**, 064017 (2010); http://iopscience.iop.org/0029-5515/50/6/064017

Pankin, A.Y., et al., "Kinetic modeling of H-mode pedestal with effects from anomalous transport and MHD stability," Problems of Atomic Science and Technology, Series Plasma Physics 17(N1) (2011) 8-12.

Snyder, P.B., et al., "A first-principles predictive model of the pedestal height and width: development, testing and ITER optimization with the EPED model" Nucl. Fusion **51**, 103016 (2011); http://iopscience.iop.org/0029-5515/51/10/103016

Stacey, W.M., et al., "Force balance and ion particle transport difference in high and low confinement tokamak edge pedestals," Phys. Plasmas **17**, 112512 (2010); http://link.aip.org/link/?PHP/17/112512

Stacey, W.M., et al., "The role a radial particle pinches in ELM suppression by resonant magnetic perturbations" Nucl. Fusion **51**, 013007 (2011); http://iopscience.iop.org/0029-5515/51/1/013007

Stacey, W.M., et al., "Evolution of the H-mode edge pedestal between ELMs," Nucl. Fusion **51**, 063024 (2011); http://iopscience.iop.org/0029-5515/51/6/063024

Yan, Z., et al., "Pedestal density fluctuation dynamics during the inter-ELM cycle in DIII-D," Phys. Plasmas **18**, 056117 (2011); http://link.aip.org/link/?PHP/18/056117

Yan, Z., et al., "High-frequency coherent edge fluctuations in a high-pedestal-pressure Quiescent H-Mode plasma," Phys. Rev. Lett. **107**, 055004 (2011); http://link.aps.org/doi/10.1103/PhysRevLett.107.055004

Yan, Z., et al., "Pedestal turbulence dynamics in ELMing and ELM-free H-mode plasmas" 2010 IAEA-FEC – EXC/p3-05; http://www-pub.iaea.org/mtcd/meetings/PDFplus/2010/cn180/cn180_papers/exc_p3-05.pdf

Submitted Publications that use DIII-D Data:

Callen, J.D., et al., "Pedestal structure model" Report UW-CPTC 11-3, July 11, 2011 (submitted to Phys. Rev. Lett.); http://www.cptc.wisc.edu

Callen, J.D., "Model for pedestal structure" Report UW-CPTC 11-4, 11 July 2011 (submitted to Phys. Plasmas); http://www.cptc.wisc.edu

Pankin, A.Y., et al., "Stress tests of transport models using FACETS code" submitted for publication to AIP Proc. for CNR-Chalmers workshop (July 2011, Varenna, Italy).

Stacey, W.M., "The effect of ion orbit loss on the interpretation of ion energy and particle transport in the DIII-D edge plasma," Phys. Plasmas (Sept 2011).

Stacey, W.M., "X-transport of ions in diverted tokamaks, with application to DIII-D," submitted to Phys. Plasmas.

Invited Overview Talk at H-Mode Workshop:

Hughes, J.W., "H-mode transition physics and H-mode pedestal structure: Pedestal dynamics near transitions and requirements for high confinement access and sustainment"

To be Presented at H-Mode Workshop:

Callen, J.D., "Comprehensive set of pedestal structure model predictions"

Canik, J.M. et al., "Effects of neutral fueling on pedestal characteristics in low and high density DIII-D H-modes"

Eldon, D.P., et al., "Initial results of the high resolution edge Thomson Scattering upgrade at DIII-D"

Lore, J.D. et al., "Effect of ECRH versus NBI heating on pedestal structure in DIII-D"

Osborne, T.H., et al., "Scaling of H-mode pedestal and ELM characteristics from a multi-tokamak database and comparison to theoretical models"

Pankin, A.Y,. et al., "Study of H-mode pedestal buildup dynamics using the FACETS code"

Smith, S.P., et al., "Testing the paleoclassical pedestal model against measured DIII-D pedestal profiles"

Snyder, P.B., et al., "The EPED pedestal model: model extensions and validation"

Sontag, A.C., et al., "Effect of toroidal rotational shear on edge ion and electron profiles"

Stacey, W.M. et al., "Non-diffusive transport in the tokamak edge pedestal"

Invited Talks to be Presented at 2011 APS-DPP Meeting:

Schmitz, L., "Predator-prey oscillations and zonal flow-induced turbulence suppression preceding the L-H transition"

Snyder, P.B., "The EPED pedestal model: gyrokinetic extensions, experimental tests, and application to ELM-suppressed regimes"

II. THEORY RESEARCH FY11

4. FINAL REPORT FOR PEDESTAL JRT – GENERAL ATOMICS THEORY GROUP (P.B. Snyder with contributions from E.A. Belli, J. Candy, N. Ferraro, J. Kinsey, G. Staebler and R. Waltz)

The GA theory group has contributed to the 2011 Joint Research Target on Pedestal Structure, via development and application of theoretical models of the pedestal structure, and engagement in model validation via comparisons to observations on DIII-D, Alcator C-Mod and NSTX. Several codes and models are being developed and applied by the GA theory group for study of the H-Mode pedestal. These include the ELITE and GATO linear MHD codes, the M3D-C1 extended MHD code, the TGYRO transport framework, the GYRO linear and nonlinear electromagnetic gyrokinetic (GK) simulation code, the TGLF model and the NEO neoclassical transport code. The EPED model, developed at GA, combines calculations of peeling-ballooning and kinetic ballooning mode (KBM) criticality conditions to predict the pedestal height and width in high performance H-modes.

4.1. Executive Summary

The EPED model, which predicts the pedestal height and width by combining calculated peeling-ballooning and KBM constraints (with no free or fit parameters) has been compared to more than 50 cases on Alcator C-Mod and DIII-D spanning a factor of 20 in pedestal height. Good quantitative agreement (within ~20-25%) is generally found in both predicted pedestal height and width, with a strong correlation (correlation coefficient $r > 0.8$) between predicted and observed pedestal height. Peeling-ballooning stability analysis with ELITE has been conducted on several experiments from Alcator C-Mod, DIII-D and NSTX, finding results consistent with peeling-ballooning modes being a constraint on the pedestal and the trigger for Type I ELMs. Non-ideal effects on peeling-ballooning modes, including diamagnetic stabilization, have been explored with M3D-C1. Gyrokinetic eigenmode analysis of the pedestal region with GYRO has identified both electron drift and KBM instabilities in the edge barrier region, and ITG and microtearing instabilities in the outer core region, and noted important effects of realistic geometry. The plasma response to applied 3D magnetic perturbations, such as those used to control ELMs, has been studied with M3D-C1, identifying the important role of rotation. Through two-fluid modeling with M3D-C1 it has been found that it is primarily the component of the electron rotation perpendicular to the magnetic field that controls the tearing mode stability. NEO calculations of neoclassical transport, including the full linearized Fokker-Planck collision operator and an impurity species, find significant (~10-20%) modifications of neoclassical bootstrap current, electron and impurity heat flux, and ion and impurity poloidal flow, due to the effects of the full collision operator and impurity species.

4.2. Final Report, Including Fourth Quarter Progress

4.2.1. Peeling-ballooning stability analysis

Intermediate wavelength MHD instabilities driven by the sharp pressure and current gradients in the edge barrier ("peeling-ballooning" modes) have been proposed as a mechanism for driving ELMs and constraining the pedestal. For the JRT, a standard procedure has been adopted for peeling-ballooning analysis, involving accurate equilibrium reconstruction and then variation around the observed

equilibrium to allow calculation of stability boundaries. The ELITE code is employed to calculate the growth rates of a range of mode numbers (typically n~5-30) on each of these equilibrium variations, and stability boundaries are then traced out and compared to observation. To date, more than 150 DIII-D cases have been studied, with several additional cases studied this past quarter, including cases with RMP ELM suppression. Several NSTX cases have also been analyzed, including a series of discharges where ELMs gradually went away after application of lithium. A series of Alcator C-Mod equilibria from ELMing discharges have been analyzed, and compared to a set of DIII-D equilibria from the recent C-Mod comparison experiment (note that the equilibria used in these stability calculations, and other analysis of the recent C-Mod and DIII-D experiments is preliminary). Figure 4-1 shows peeling-ballooning stability diagrams for C-Mod and DIII-D discharges which are near a dimensionless match in the pedestal. Figure 4-2(a,b) shows the calculated n=25 peeling-ballooning mode structures for matched C-Mod and DIII-D discharges, with the n=12 mode structure from NSTX 129022 shown for comparison in Fig. 4-2(c). Results suggest that Type I ELM onset and observed pedestal constraints are generally consistent with expectations from peeling-ballooning stability, and further analysis is ongoing.

Non-ideal modeling of linear peeling-ballooning eigenmodes and nonlinear ELM dynamics has been performed with M3D-C1. Linear growth rates obtained with M3D-C1 have shown good agreement with calculations using GATO and ELITE in the ideal limit. Beyond this, the effects of edge resistivity and two-fluid effects have been explored using M3D-C1. Calculations including gyroviscosity have been carried out to test the simple diamagnetic stabilization model used to interpret ELITE results; the results of these calculations show that the self-consistent treatment is somewhat less stabilizing than the simple theory suggests, but generally not by a significant margin. Nonlinear ELM calculations have recently been performed, but this study is still at an early stage.

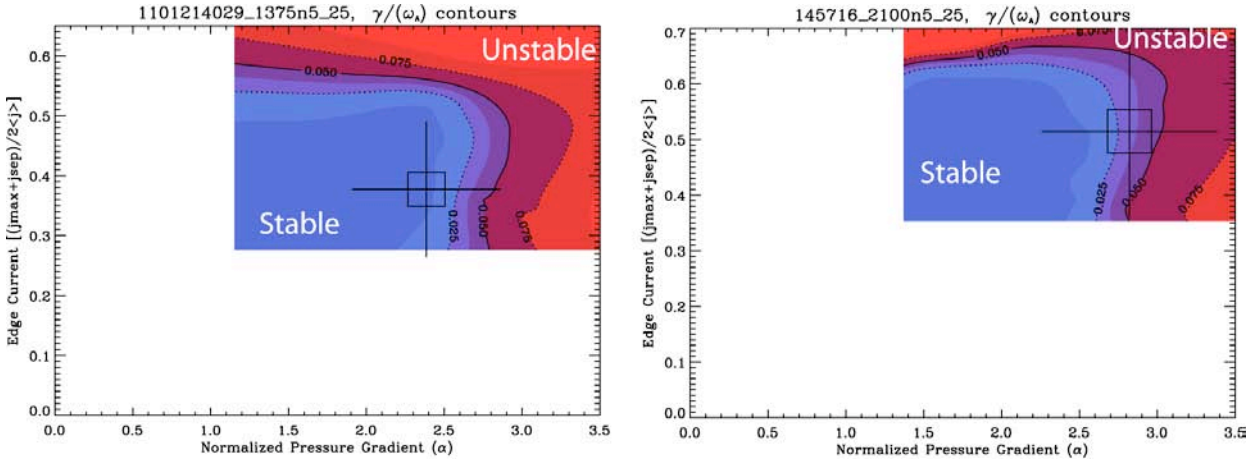

Fig. 4-1. Peeling-ballooning stability diagrams calculated with ELITE for (a) Alcator C-Mod shot 1101214029, and (b) DIII-D shot 145716. These discharges are near dimensionless similarity, with the DIII-D discharge run in the typical Alcator C-Mod ELMing shape. The crosshair shows the location of the experimental operating point, and the stability boundary is constructing by calculating the n=5-25 stability of ~150 equilibria perturbing around the experimental point. The resulting peeling-ballooning stability boundary is similar (α_{crit}~3), as expected, with both discharges approaching a similar part of the stability boundary shortly before an ELM is observed. (Note that the equilibria used in this study are preliminary)

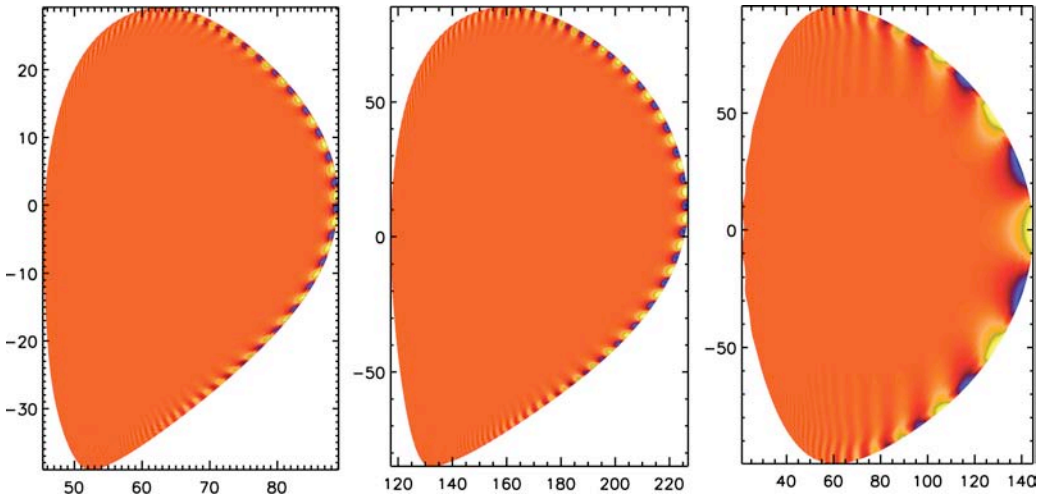

Fig. 4-2. Calculated n=25 peeling-ballooning mode structure from ELITE for (a) Alcator C-Mod shot 1101214029, and (b) DIII-D shot 145716. The yellow and blue contours near the edge show the ballooning structure of the mode. These discharges are near dimensionless similarity, with the DIII-D discharge matching the typical Alcator C-Mod ELMing shape. The resulting peeling-ballooning mode structure is similar as expected. (c) The calculated n=12 mode structure for NSTX shot 129022 is shown for comparison. (Note that the equilibria used in this analysis are preliminary)

4.2.2. The EPED pedestal model

The EPED model combines calculated peeling-ballooning and kinetic ballooning mode (KBM) constraints to predict the height and width of the pedestal, as shown in Fig. 4-3(a). The present version of the model, EPED1.6, calculates both constraints directly for each case, and has zero fit parameters and zero free parameters. This quarter, predictions from the full EPED1.6 model have been compared to a set of 24 Alcator C-Mod cases, a set of 20 DIII-D cases from the Alcator C-Mod similarity experiment (matching the C-Mod ELMing shape), and an additional set of 15 DIII-D discharges from other experiments. Results of this comparison are shown in Fig. 4-3(b,c). These 59 cases from C-Mod and DIII-D cover a range of a factor of ~20 in pedestal pressure (1.7 to 35 kPa), and a factor of ~9 in pedestal beta (0.13-1.9%). The EPED1.6 model predicts the pedestal height with good accuracy, with a ratio of predicted to observed pedestal height of 1.15 ± 0.23, and a correlation coefficient of 0.96 between predicted and observed pedestal height. [Note: The observations on C-Mod are averaged over the ELM cycle, while the EPED model predicts the fully developed pedestal height (near maximum), so a slight overprediction is expected, particularly at larger pressures where the ELMs are large.] In addition, the simplified EPED1 model has been compared to a set of current, magnetic field, and shape scans on DIII-D that were conducted in 2008, and carefully analyzed as part of the JRT. The results are shown in Fig. 4-4(a), with very good agreement found between the EPED1 predicted pedestal pressure and the observations. A dedicated experiment to test the EPED model, and KBM physics, was conducted on DIII-D on May 20, 2011. This experiment took advantage of the recent upgrade to the DIII-D Thomson scattering system to produce accurate measurements of the pedestal height and width. The experiment consisted of a series of current and magnetic field scans, in plasmas optimized for good coverage with both profile and turbulence diagnostics. EPED1 predictions were made and presented before the experiment was conducted. An initial comparison between these EPED1 predictions and the measured pedestal heights and widths (16 cases from 9 discharges) is shown in Fig. 4-4(b,c). Preliminary

agreement between the EPED1 predictions and observations is very good with a ratio of predicted to observed pedestal height of 1.13 ± 0.22 with a correlation of 0.81, and a ratio of predicted to observed pedestal width of 1.00 ± 0.13 with a correlation of 0.93.

The EPED model, including the full EPED1.6 and the simplified EPED1, has now been compared to more than 200 cases on 5 tokamaks, generally finding good quantitative agreement (within ~20–25%), and strong correlation (r>~0.8), between predicted and observed pedestal height. The EPED1.6 model and initial comparisons to DIII-D, C-Mod and JET are described in a recent paper [Snyder et al, Nucl. Fusion **51** 103016 (2011)], and additional detailed comparisons with C-Mod will be described in an upcoming paper by J. Walk et al. Further comparisons will be described in upcoming H-Mode Workshop presentations by T. Osborne, J. Hughes, and M. Beurskens, and an upcoming APS/DPP invited talk by P. Snyder.

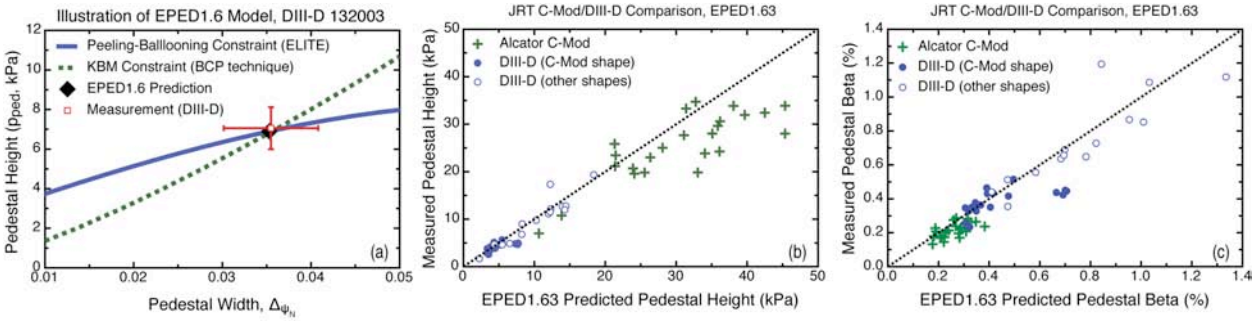

Fig. 4-3. (a) The EPED1.6 model predicts the pedestal height and width by combining calculated peeling-ballooning (solid line) and KBM (dotted line) constraints. The EPED prediction (solid diamond) can then be compared to observations (open square). Comparisons of the EPED1.63 predicted and observed pedestal height for a set of 24 Alcator C-Mod (green crosses), 20 DIII-D discharges in the Alcator C-Mod shape (solid circles), and 15 DIII-D discharges in other shapes (open circles), are given in terms of pedestal pressure (b) and pedestal beta (c), with the dotted line indicating perfect agreement.

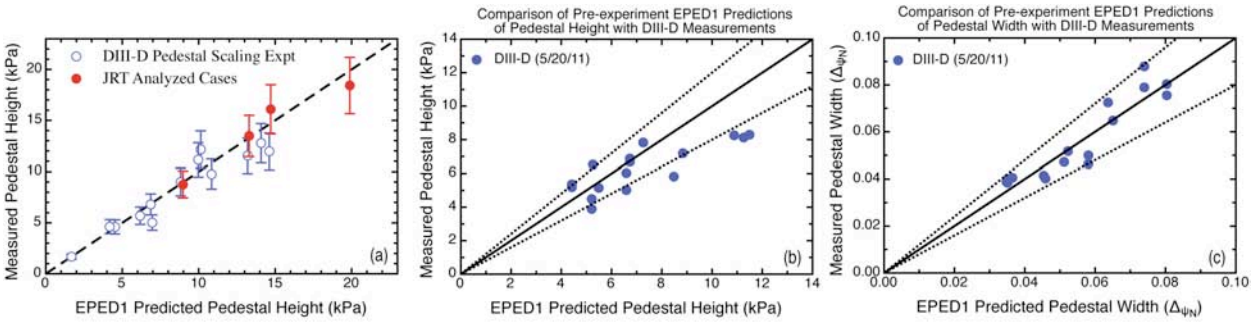

Fig. 4-4. (a) Comparison of EPED1 predicted pedestal height to DIII-D observations in a pedestal scaling experiment, including a current scan (filled circles) that has been carefully analyzed as part of the JRT. Preliminary comparison of EPED1 predicted (b) pedestal height and (c) pedestal width to DIII-D observations in a recent (5/20/11) pedestal experiment employing high resolution Thomson scattering measurements in a scan of plasma current and magnetic field.

4.2.3. Gyrokinetic stability and transport, and neoclassical transport

A number of microinstabilities, including the KBM, ETG, ITG/TEM, microtearing and Kelvin-Helmholtz modes, may potentially play a role in governing pedestal structure and transport. Quantitatively studying these modes in the edge barrier region generally requires challenging calculations

that include electromagnetic perturbations, realistic geometry, collisions, and a wide range of scales. The GYRO code now includes fully electromagnetic perturbations, full geometry, and collisions, and is incorporated along with the NEO neoclassical code, and the TGLF transport model inside the TGYRO transport framework. This quarter, we have continued to test and employ the general geometry capability of TGYRO, as well as conducing electromagnetic gyrokinetic stability studies in Miller geometry. All TGYRO/GYRO/NEO/TGLF components can make use of data in numerous formats (plasma state, iterdb, astra, p-file) and can optionally include geometry data from the EFIT g-file. These components are now available via GitHub, and user support is being provided to scientists at GA, LLNL and NSTX who are undertaking gyrokinetic pedestal studies as part of the JRT. We have explored gyrokinetic stability in the pedestal for an equilibrium based on DIII-D shot 131997. We have determined nominal grid resolution parameters for running the recently-developed GA field eigenvalue solver. Using the eigenvalue solver, we can track more than just the most unstable mode. In particular, we can also follow the evolution of the (local) mode from core to edge. GYRO finds ITG and microtearing unstable in the core, and a KBM-like mode unstable in the center of the pedestal when the pedestal is near of beyond the ideal ballooning threshold (as expected). Strong electron drift instabilities are also found and will be further investigated. One significant result is that exact geometry is critical to an accurate calculation of the growth rate: we found that in the region of strongest gradient, the difference between Miller and general geometry was a factor of two. This is in contrast to the core, where the difference is typically less than 1%. More detailed studies and code-code benchmarks are ongoing (see also LLNL section). The full linearized Fokker-Planck collision operator, full edge geometry, and rapid toroidal rotation, have been added to the NEO code, and extensive sets of neoclassical transport have been undertaken including impurity species and the full collision operator. These studies find significant (~10-20%) modifications to the neoclassical bootstrap current, the electron and impurity heat flux, and the ion and impurity poloidal rotation due to the inclusion of the full physics model (compared to simplified models such as NCLASS, Sauter, and Chang-Hinton).

4.2.4. Plasma response to 3D fields

Edge response to externally applied non-axisymmetric fields has been explored using linear non-ideal MHD modeling. The goals of this modeling were to gain an understanding of the level of stochasticity expected to occur in the pedestal relative to vacuum modeling; to evaluate the penetration of resonant fields (and the associated of islands) near the top of the pedestal; and to make quantitative predictions for magnetic measurements of plasma response within the separatrix. Reconstructed axisymmetric equilibria from DIII-D discharges were considered. The extended-MHD code M3D-C1 was used to perform these calculations [N.M. Ferraro and S.C. Jardin. J. Comp. Phys. 228:7742 (2009)]. This code implements a resistive, two-fluid model, and includes equilibrium rotation. M3D-C1 is well suited for studies of the plasma edge because it self-consistently includes the core, edge, and open field-line regions within its computational domain. Furthermore, these calculations use the Spitzer resistivity based on experimental electron temperature profiles, and realistic values of perpendicular energy and momentum transport.

The results of modeling error field penetration clearly show the importance of plasma rotation. This is demonstrated by a series of calculations done using the reconstructed equilibrium from DIII-D shot 135762 subject to applied n=1 fields from the DIII-D I-coils (as was the case in the experiment). When the plasma response is not taken into account, large islands are found to exist in the core, and much of the

pedestal is found to be stochastic. When the plasma response is taken into account, the results depend strongly on the equilibrium rotation profile. If rotation is omitted, the q=3 island is actually enhanced in this case, whereas the stochasticity in the pedestal is found to be reduced from the vacuum case. The core islands are found to be strongly reduced by the inclusion of rotation; however, the edge stochasticity is sensitive to the rotation profile. Specifically, including a rotation profile that is proportional to the pressure profile (which, in this H-mode case, drops sharply to zero at the edge) is found actually to enhance the edge stochasticity significantly. In contrast, if the rotation is taken to be uniform throughout the plasma, the edge stochasticity is reduced. These four cases are illustrated in Fig. 4-5.

Through two-fluid modeling with M3D-C1 it has been found that it is the component of the electron rotation perpendicular to the magnetic field that controls the tearing mode stability, as opposed to ion rotation or parallel flows. A calculation of the perturbed magnetic fields expected to be present along the anticipated path of a proposed plunging magnetic probe just within the separatrix has also been conducted. For this calculation, the response of DIII-D shot 126006 to n=3 fields was considered with both M3D-C1 and MARS-F, and the results of the two codes showed relatively good quantitative and qualitative agreement, despite differences in the codes' scrape-off layer and vacuum vessel models. The plasma response is found to be greatest just within (~2 cm) the separatrix, and is found to be significantly larger than the vacuum fields there.

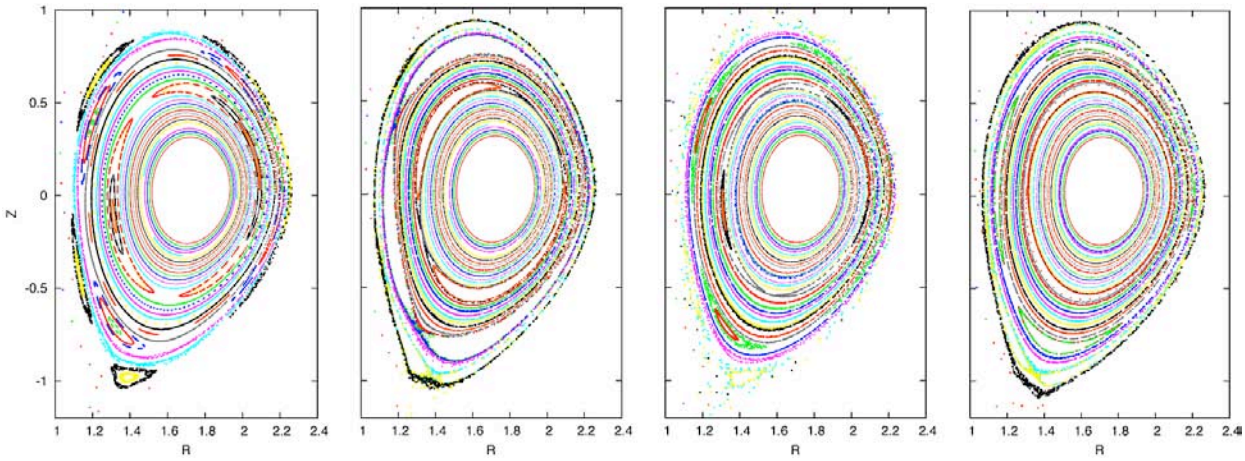

Fig. 4-5. Poincaré plots show the calculated perturbed equilibrium of DIII-D shot 135762 in response to applied *n*=1 fields from the DIII-D I-coils. From left to right: plasma response is ignored; plasma response is included, but without equilibrium rotation; equilibrium rotation is proportional to the pressure profile; equilibrium rotation profile is flat.

Bibliography for Section 4

Belli E.A. and J. Candy, "Fully electromagnetic gyrokinetic eigenmode analysis of high-beta shaped plasmas," Phys. Plasmas **17**, 112314 (2010).

Belli E.A. and J. Candy, "An Eulerian method for the solution of the multi-species drift-kinetic equation," Plasma. Phys. Control. Fusion **51**, 075018 (2009).

Beurskens M.N.A. et al. including P.B. Snyder, "H-Mode pedestal scaling in DIII-D, ASDEX Upgrade and JET," Phys. Plasmas **18**, 056120 (2011).

Boedo J.A., E.A. Belli et al., "Poloidally and radially resolved parallel D+ velocity measurements in the DIII-D boundary and comparison to neoclassical computations," Phys. Plasmas **18**, 032510 (2011).

Candy J., "A unified method for operator evaluation in local Grad-Shafranov plasma equilibria," Plasma Phys. Control. Fusion **51**, 105009 (2009).

Candy J. and E.A. Belli, "Neoclassical transport including collisional nonlinearity," Phys. Rev. Lett. **106**, 235003 (2011).

Doyle E.J. et al. including P.B. Snyder, "Demonstration of ITER operational scenarios on DIII-D," Nucl. Fusion **50**, 075005 (2010).

Ferraro N.M., S.C. Jardin, and P.B. Snyder, "Ideal and resisitive edge stability calculations with M3D-C1," Phys. Plasmas **17**, 102508 (2010).

Groebner R.J., P.B. Snyder, T.H. Osborne et al.," Limits to the H-Mode pedestal pressure gradient in DIII-D," Nucl. Fusion **50**, 064002 (2010).

Guttenfelder W., J. Candy et al., "Electromagnetic transport from microtearing mode turbulence," Phys. Rev. Lett. **106**, 155004 (2011).

Hudson B., T.E. Evans, T.H. Osborne, CC. Petty, P.B. Snyder and E.A. Unterberg, "ELM suppression by resonant magnetic perturbation in high-performance stationary plasmas," Nucl. Fusion **50**, 045006 (2010).

Kinsey J.E., G.M. Staebler, J. Candy, R.E. Waltz and R.V. Budny, "ITER predictions using the GYRO verified and experimentally validated TGLF transport model," Nucl. Fusion **51**, 083001 (2011).

Snyder P.B., ITPA Pedestal Group, "Pedestal stability comparison and ITER pedestal prediction," Nucl. Fusion **49**, 085035 (2009).

Snyder P.B., R.J. Groebner, A.W. Leonard, T.H. Osborne and H.R. Wilson, "Development and validation of a predictive model for the pedestal height," Phys. Plasmas **16**, 056118 (2009).

Snyder P.B., R.J. Groebner, J.R. Hughes et al., "A first-principles model of the pedestal height and width: Development, testing, and ITER optimization with the EPED model," Nucl. Fusion **51**, 103016 (2011).

Staebler G.M., R.E. Waltz, and J.E. Kinsey, "Discoveries from the exploration of gyrokinetic momentum transport," Phys. Plasmas **18**, 056106 (2011).

Waltz R.E., G.M. Staebler, and W. Solomon, "Gyrokinetic simulation of momentum transport with residual stress from diamagnetic level velocity shears," Phys. Plasmas **18**, 042504 (2011).

Yan Z., G.R. McKee, R.J. Groebner, P.B. Snyder, T.H. Osborne, and K.H. Burrell, "High-frequency coherent edge fluctuations in a high-pedestal-pressure Quiescent H-Mode plasma," Phys. Rev. Lett. **107**, 055004 (2011).

5. FINAL FY11 JRT REPORT FOR LLNL THEORY GROUP (X.Q. Xu)

5.1. Executive Summary

We have used the two-fluid turbulence code BOUT++ and the electromagnetic gyro-kinetic code GYRO to analyze the linear stability of one C-Mod EDA H-mode discharge at modest plasma current and input power, to simulate two ELMy H-mode discharges from NSTX, and to study two H-mode discharges from DIII-D released to collaborators for the FY11 Joint Research Target on pedestal physics. The preliminary results are summarized below and more extensive simulations are in preparation for three publications.

We hosted an international 3-day BOUT++ workshop at LLNL from September 14–16, 2011 (http://bout2011.llnl.gov). The workshop goals were to (1) help prepare fusion researchers to use and further develop the BOUT++ code for plasma edge turbulence, transport, and plasma Edge Localized Mode (ELM) simulations of magnetic fusion devices, and (2) to promote effective collaboration within the BOUT international community. There were 49 registered attendees from five countries in attendance: China, PRC (6), Japan (2), Korea, ROK (5), UK (2) and USA (34). The US participants were from 15 U.S. fusion institutions representing the national labs, universities, and industry participants within the DOE SC Fusion Energy Sciences program. Sixteen percent of the participants are experimentalists from C-Mod, DIII-D, NSTX, and EAST. The workshop agenda had been structured to include special lectures, oral talks and Hands-on exercise examples. The special lectures are on BOUT++ code, solvers, and gyro-fluid extensions. The oral talks are on BOUT++ application to tokamaks, linear machines, and BOUT++ performance analysis to massive concurrency. The Hands-on exercise examples are on (1) basic plasma instabilities; (2) advanced example on ELM simulations; and (3) BOUT++ applications to linear machines and tokamaks. The lecture notes, talks and hands-on exercise examples are available online.

5.2. BOUT++ Simulations of C-Mod EDA H-mode Discharges

Over the last quarter, Evan Davis, an MIT graduate student of Miklos Porkolab visited LLNL for his NNSA Stewardship Science Graduate Fellowship summer practicum. During his visit, Mr. Evan Davis worked on BOUT++ simulations of C-Mod JRT discharge 1110201023 at time 900ms, an enhanced D_α (EDA) H-mode at modest plasma current and input power.

The EDA H-mode typically accessed on C-Mod is relatively quiescent with good energy confinement and reduced impurity confinement. The pedestal plasma is regulated by a continuous quasi-coherent mode (QCM) oscillation between 50 - 200 kHz. To simulate the QC mode, experimentally measured C-Mod kinetic profiles were first used to produce a constrained equilibrium solution (kinetic EFIT) with single-null divertor geometry. The EFIT result provided high resolution profiles of pressure, current, and magnetic field as input for BOUT++ simulations. The preliminary BOUT++ results show

1. C-Mod EDA H-Modes are ideal peeling-ballooning mode stable, which is consistent with the observation of a relatively quiescent plasma with no ELMs for this discharge.
2. C-Mod's EDA H-mode is resistively unstable, and the BOUT++ computed growth rates and linear mode spectrum are consistent with resistive-ballooning mode theory (Figs. 5-1 and 5-2).

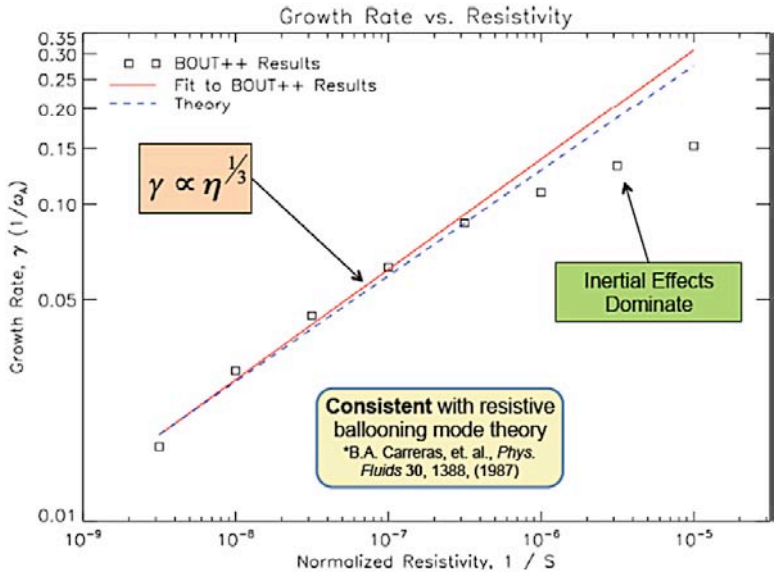

Fig. 5-1. At low resistivity, BOUT++ computed growth rates scale as the one-third power of resistivity, consistent with resistive-ballooning mode theory.

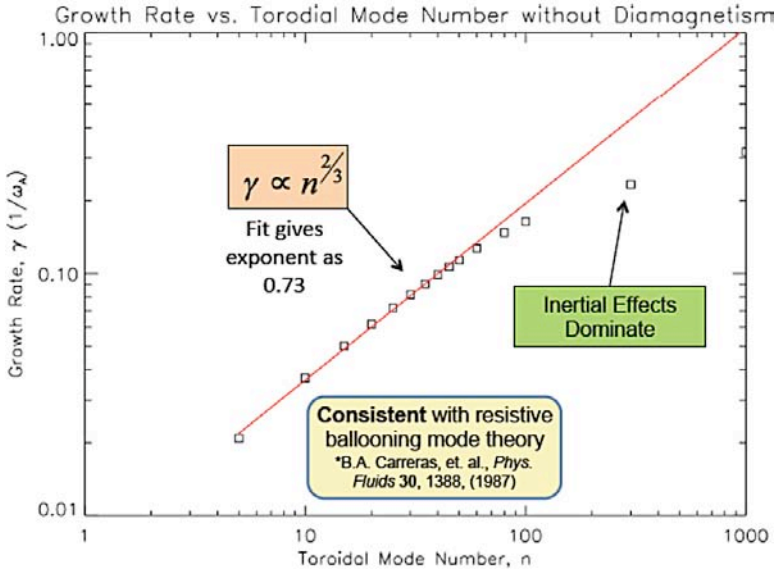

Fig. 5-2. At low toroidal mode number (n), BOUT++ computed growth rates scale as the two-thirds power of n, consistent with resistive-ballooning mode theory.

3. Inclusion of diamagnetic effects and electric field from force balance (assuming no flow) in BOUT++ simulations gives rise to a mode propagating in the same direction as the QC Mode in the laboratory frame. BOUT++ calculations show that ion diamagnetic effects damp higher toroidal mode numbers n (Fig. 5-3). The resistive ballooning mode is peaked at n=25, which is consistent with observations showing toroidal mode numbers for the QCM ranging from 10 to 25. Future simulations will include experimentally measured equilibrium flows from CXRS (i.e. Charge Exchange Recombination Spectroscopy) to get quantitative comparison for the QC mode frequency.
4. Preliminary nonlinear BOUT++ simulations have been done for further comparisons with fluctuation diagnostics to determine the physical origins and effects of the QC Mode (Fig. 5-4).

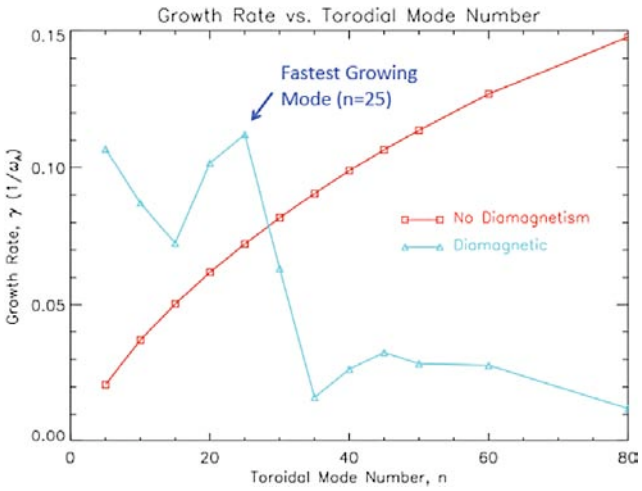

Fig. 5-3. BOUT++ calculations show that ion diamagnetic effects damp higher toroidal mode numbers n.

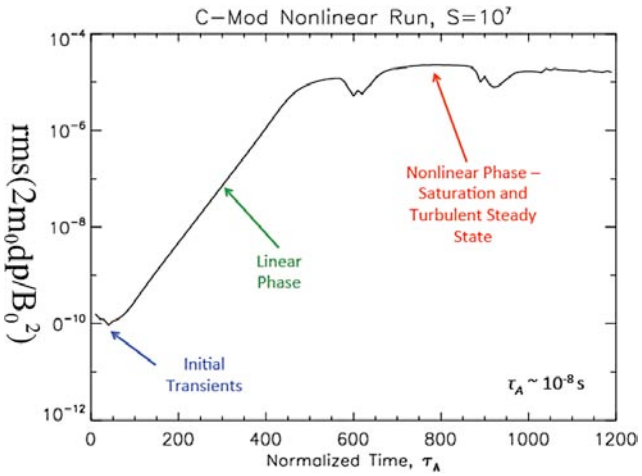

Fig. 5-4. BOUT++ nonlinear simulations of QC mode, showing fluctuating pressure vs. time at outer mid-plane.

5.3. BOUT++ Analysis of NSTX Discharges

The BOUT++ peeling-ballooning ELM model was used to analyze the JRT/ NSTX-ELM series of data. The linear stability of two ELMing NSTX discharges, 129019 and 129032, was studied. Both cases approximately have $B_{T,axis}$ = 0.44 T at R_{axis} = 0.94 m, I_{plasma} = 0.7MA and, for simplicity, a constant density profile $n_e=10^{19}$ m^{-3}. It was found that 129032 is unstable to ELMs and the mode structure for a typical case is shown on the radial-poloidal plane in Fig. 5-5. However, the mode is stabilized for all test cases by diamagnetic effects when one assumes that ExB rotation cancels ion diamagnetic rotation in the pedestal; i.e. assuming that ions are electrostatically confined by the relation $eN_eE_r=dP_i/dr$. Discharge 129019 was not found to be unstable to either ideal or resistive edge instabilities. Under the same assumptions, stability would be expected for NSTX discharges 129031 and 129038 because they have edge pedestal pressure and current profiles that are similar to or smoother than 129019. Due to the sensitivity of the results to the edge flow, it is important to continue studying these discharges with the experimental profiles and using higher resolution EFITs and improved mesh generation capability.

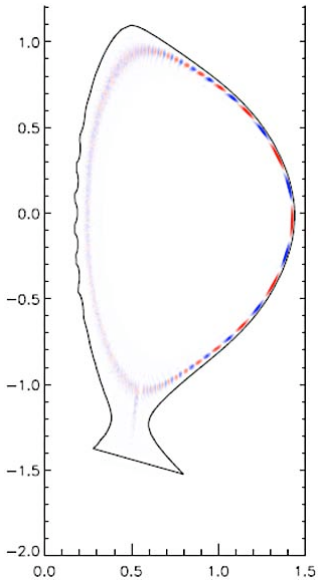

Fig. 5-5. Ballooning mode structure for NSTX discharge 129032.

NSTX discharge 129032 (at 550 ms) has an edge instability that increases with toroidal mode number n and with increasing resistivity. The growth rate vs. toroidal mode number is shown in Table 5-1(a) for a Lundquist number 10^8 and the growth rate vs. Lundquist number is shown in Table 5-1(b) and Fig. 5-6 for Lundquist numbers ranging from 10^6-10^9. Discharge 129019 was stable for a similar range of parameters. Because it is stabilized by the assumed combination of ExB and diamagnetic flows, one would not expect this mode to be classified as an ideal instability.

Table 5-1
(a) Growth rate vs. toroidal mode number for NSTX discharge 129032 for Lundquist number 10^8.
(b) Growth rate vs. Lundquist number for toroidal mode number n=40.

(a) Toroidal mode No. n (Lundquist=10^8)	Growth Rate
8	0.015
10	0.019
15	0.029
20	0.038
30	0.053

(b) Lundquist No. (n=40)	Growth Rate
10^6	0.126
10^7	0.081
10^8	0.058
10^9	0.052

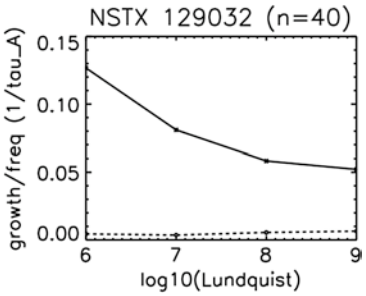

Fig. 5-6. Growth rate vs. Lundquist number for NSTX discharge 129032 for toroidal mode number n=40.

This study used 129x129 EFIT reconstructions to generate BOUT++ meshes with 512 radial x 256 poloidal grid points. However, these NSTX equilibria have strong geometric shaping that significantly stresses the capabilities of the BOUT++ grid generator and higher resolution EFITs should be used in the future. Significant improvements were made to 2d interpolation of functions and gradients within the grid generator. We have added spline, periodic spline, and Fourier-filtering capabilities to smooth the magnetic curvature components, which are the most difficult quantities to calculate. We plan to test the impact of the new grids on the stability results.

5.4. BOUT++ and GYRO Analysis of DIII-D Discharges

Over the last two quarters, a multi-code benchmark effort was initiated and focused on a simplified version of DIII-D experimental shot 131997, where the pedestal measurements are well studied and characterized. A series of equilibria based on 131997 were created in order to vary the total pressure from 0.5 to 1.2 of the experimental value using the varyped tool. The goal of the pressure scan is to demonstrate clear onset of the kinetic ballooning mode (KBM), which occurs in a narrow range near the ideal ballooning threshold, using gyrokinetic simulations of the pedestal. Results are being compared between the Eulerian gyrokinetic code GYRO and the PIC gyrokinetic code GEM. A successful benchmark will lay the groundwork for understanding the structure of the kinetic ballooning mode in the pedestal region of the tokamak and help to determine resolution requirements needed for realistic discharges. We expect to be able to apply the same technique to many different experimental discharges in a fairly straightforward manner.

5.4.1. Summary of results-BOUT++

The BALOO and BOUT++ codes were used to determine the ideal ballooning threshold. Using BOUT++, a threshold for the stability of this mode was observed at 0.7 of the experimental pressure profile as shown in Fig. 5-7. This is consistent with a set of infinite-n ballooning runs using BALOO code and the ELITE peeling-ballooning runs. However, the addition of electron inertial effects causes the mode to become unstable over the entire scan, shown in Fig. 5-7 as dashed curve. For other DIII-D tokamak discharges, such as shot 132016, we also found that the collisionless ballooning modes are unstable in H-mode pedestal, and have lower beta threshold than ideal peeling-ballooning modes, which may be responsible for H-mode turbulence transport.

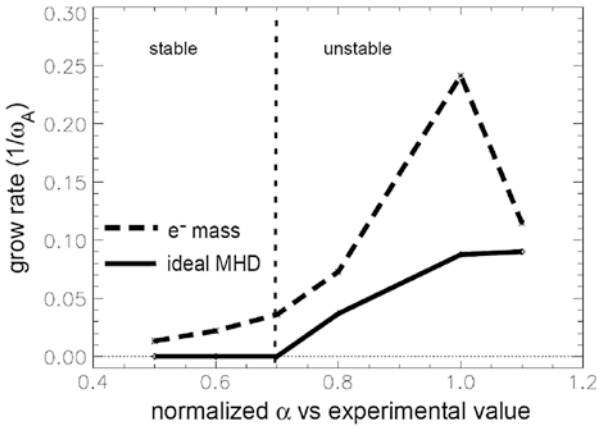

Fig. 5-7. Growth rate vs. normalized pressure gradient for toroidal mode number n=15. The solid curve is for idea MHD; the dashed curve is for non-ideal MHD with electron inertial.

5.4.2. Summary of gyro-kinetic electromagnetic simulation results

Results are being summarized from the Eulerian gyrokinetic code GYRO and the PIC gyrokinetic codes GEM and GTC.

Summary of results-GYRO:

- GYRO finds two modes competing for dominance in the peak gradient region of the pedestal - a mode whose frequency shifts between the electron and ion diamagnetic direction, and a purely ion direction mode (Fig. 5-8). Both modes contain ballooning structure peaking close to the INBOARD midplane (Figs. 5-9, 5-10).

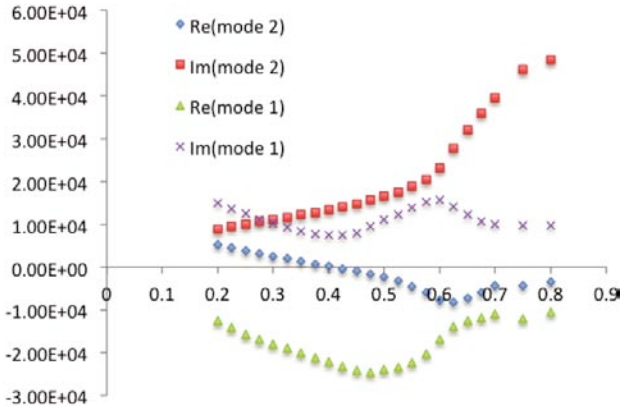

Fig. 5-8. Growth rate and frequencies in (1/s) for two most unstable modes in peak gradient region vs. $k_q r_s$ as calculated by GYRO.

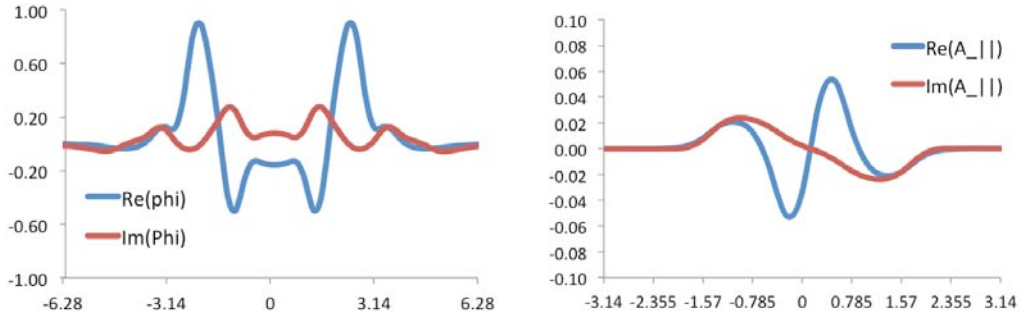

Fig. 5-9. Ballooning structure of dominant (mode2) mode for electrostatic potential (left) and electromagnetic potential (right).

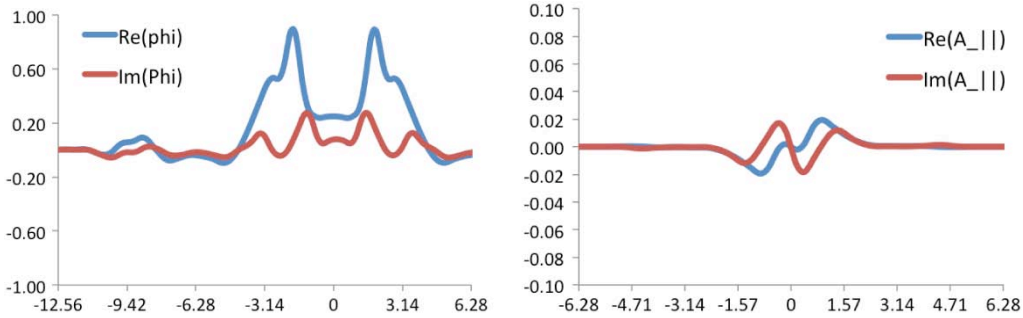

Fig. 5-10. Ballooning structure of dominant (mode1) mode for electrostatic potential (left) and electromagnetic potential (right).

- Outside of the peak gradient (ψ_N <~ .965), the dominant instability is ITG.
- A pressure scan of DIII-D shot 131997 demonstrates onset of KBM at about 90% of the experimental pressure (Table 5-2), in agreement with ELITE calculations (Table 5-3). The growth rate of the KBM in this region is very weak compared to the dominant electron mode and ITG. The ballooning structure of KBM of electrostatic potential and electromagnetic potential is shown in Fig. 5-11.

Table 5-2
GYRO calculated KBM frequency and growth rate for pressure scan at $k_\theta\rho$=0.25. Growth rate is close to negligible at 90% of the experimental pressure value.

Percentage Pressure of Experimental Value	Im Frequency (1/s)
1.2	36,400
1.1	41,400
1.0	44,300
0.9	44,600
0.8	31,300
0.7	9,001

Table 5-3
ELITE calculation of ideal ballooning mode stability. Column 2 demonstrates the radial range of instability, with Column 3 demonstrating the peak growth rate. Both ELITE and GYRO predict the ballooning mode will not be unstable for pressures below 90% of the equilibrium value.

Percentage Pressure of Experimental Value	Radial Domain (psi_N)	Peak Growth Rate n=25 (au)
1.2	0.963–0.995	0.108
1.1	0.967–0.995	0.0748
1.0	0.967–0.995	0.0333
0.9	0.971–0.991	0.00005

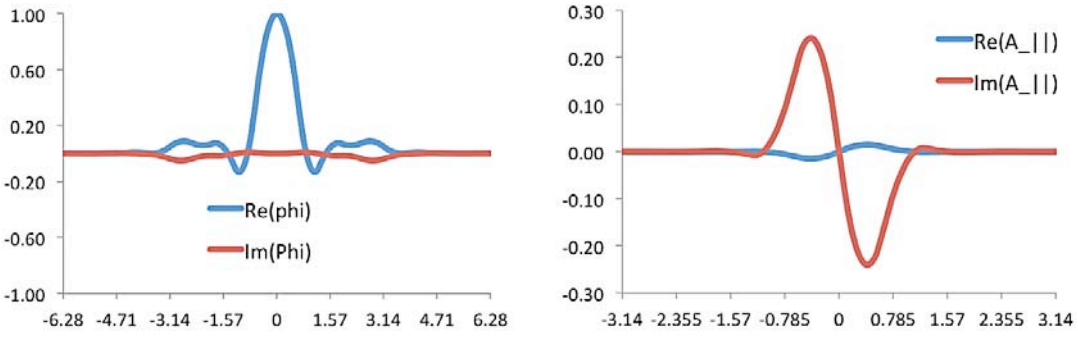

Fig. 5-11. Ballooning structure of KBM of electrostatic potential (left) and electromagnetic potential (right). The right plot demonstrates the real (pink) and imaginary (yellow) components are odd about θ=0, with opposite sign. This is exactly the ballooning structure of the KBM.

Summary of results-GEM:

- Dominant instability in peak gradient region is density gradient driven, with strong response to the electron temperature gradient.
- ITG dominant outside peak gradient, in agreement with GYRO
- The real frequency is in the positive (electron) or negative (ion) direction depending on high or low values of $k_\theta \rho_s$ in the peak gradient region.
- Inclusion of E_r causes instability to be in electron direction, regardless of $k_\theta \rho_s$, most likely due to Doppler shift.

Summary of results-GTC/GYRO/GEM comparison:

- Very good agreement between GEM and GYRO for growth rate of ITG mode at ψ_N = 0.945 (Fig. 5-12). Real frequency disagrees by factor of ~2.5. The discrepancy may be accounted for because the underlying flux tube geometry simulated between GYRO and GEM are not the same. GEM uses Miller geometry, generating coefficients in a manner different from GYRO, which can either use Miller geometry or full geometry. However, GYRO's calculation of Miller coefficients differs from GEM's calculation, so exact equilibria comparisons at the moment are not done.
- GTC- Manually created flux tubes for comparison with GYRO and GEM at radial location (ψ_N = 0.945) outside of peak gradient region. Peak growth rate and frequency are in correct range of GYRO/GEM results (simulations pick out peak growth rate instead of growth rate vs. $k_\theta \rho_i$.)
- Discrepancy between GEM and GYRO for peak gradient region is subject of current study (Fig. 5-13).

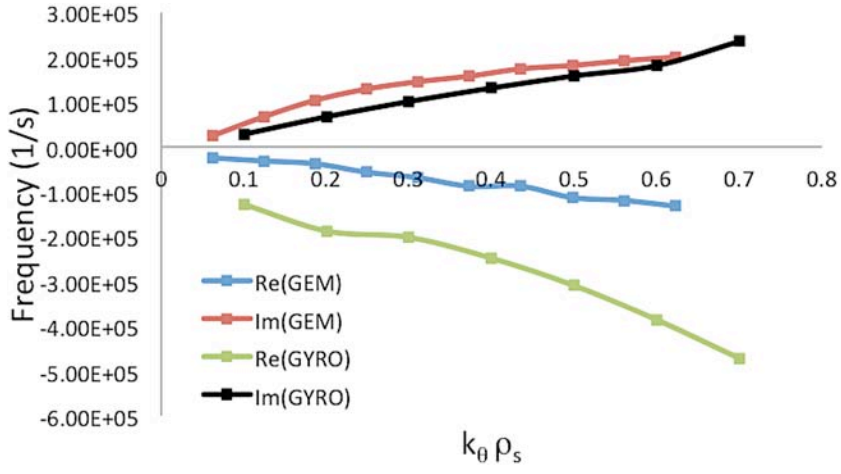

Fig. 5-12. Growth rate and real frequency of dominant ITG mode for GYRO and GEM for y_N=0.946. The two codes use different models to describe the flux surface geometry (GEM uses Miller, GYRO a numerical description), which would explain the disagreement.

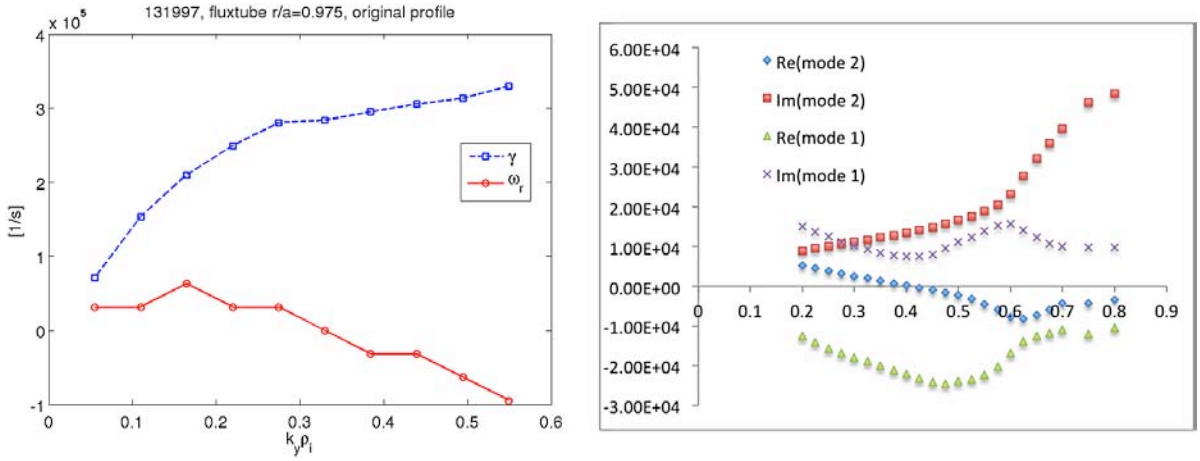

Fig 5-13. k_θ ρ scan for GEM (left, initial value) and GYRO (right, initial value) at the peak gradient region. Disagreement could be attributed to each code assigning different Miller geometry coefficients for the same radial location.

Publications for Section 5

[5-1] Wang E., X.Q. Xu, J. Candy, P. Snyder, and R. Groebner, submitted to Contribution to Plasma Physics, 2011.

[5-2] Davis E., et al. in preparation

[5-3] Xu X.Q., et al, in preparation for Nucl. Fusion.

6. FINAL FY11 JRT REPORT FROM CENTER FOR PLASMA EDGE SIMULATION (C.S. Chang)

The SciDAC Center for plasma edge simulation (CPES, now headquartered at PPPL) has been developing first-principals-based simulation tools, which are applicable to the 2011 Joint Research Target on Pedestal Structure. All of these simulation tools use realistic diverted magnetic field geometry, based upon the experimental g-eqdsk data. XGC0 is a kinetic neoclassical transport code with an anomalous transport modeling capability, XGC1 is a gyrokinetic turbulence-neoclassical code, Flow-M3D is a free boundary equilibrium reconstruction code with toroidal and poloidal flows and is used by XGC, and EFFIS is an automated integrated simulation framework tool to couple XGC, Flow-M3D, M3D-omp, M3D-mpp, and the GA-York's code Elite. XGC0-RMP has the capability to simulate the kinetic RMP penetration, consistently with pedestal evolution and transport. We present the results from XGC0 here.

6.1. Neoclassical Behavior of Density Pedestal Width

The XGC0 kinetic transport code has been used to study the neoclassical pedestal density width behavior with respect to the variation of B_T, B_P, n_e, and T_i. We compare the results between a low field, low density plasma in DIII-D geometry and a high field, high density plasma in C-Mod geometry. Figure 6-1 shows a comparison of the scaling behaviors for the density pedestal width in ψ_N space. It can be seen from Fig. 6-1(a) that the predicted density pedestal width does not show a dependence on the pedestal density height in the high density C-Mod plasmas (the variation seen in the figure is from statistical simulation noise). However, at the lower pedestal densities in DIII-D (below $4x10^{19}m^{-3}$), the pedestal width increases with decreasing density height. The latter phenomenon, observed from low density DIII-D simulation, is from the neutral penetration effect. The "Mahdavi" pedestal model may correspond to this regime only. At a higher pedestal density, the neutral penetration effect is not as robust and its physics is masked by the neoclassical plasma physics.

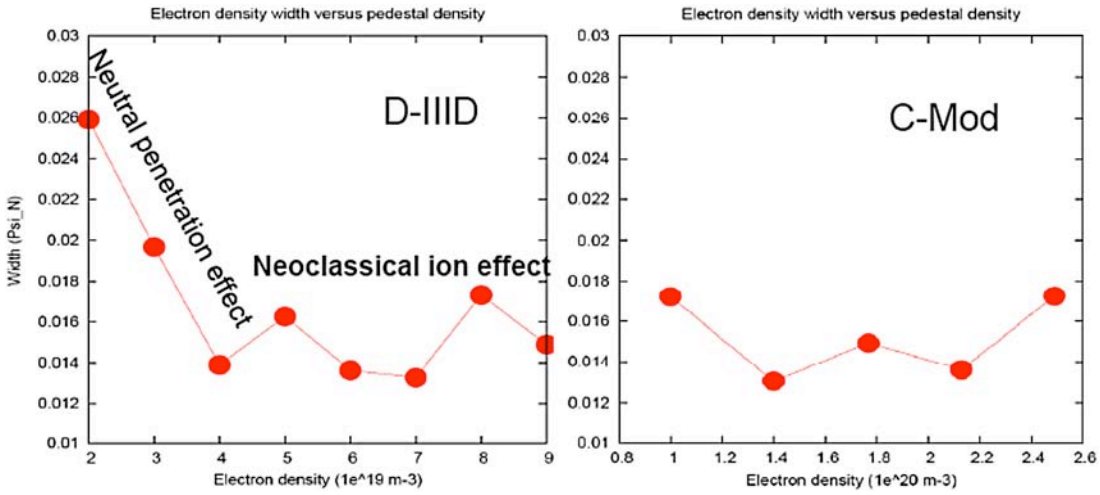

Fig. 6-1. Density pedestal width in ψ_N vs. pedestal density height.

From Fig. 6-2, it can be seen that the $T_i^{1/2}$ proportionality of the density pedestal width is common between DIII-D and C-Mod. Figure 6-3 shows that the density pedestal width has a $1/B_p$-like dependence on both devices. The high field device C-Mod has a more distinctive $1/B_p$ dependence than the low field

DIII-D machine. From Fig. 6-4, it can be seen that the high field device C-Mod does not show a B_T dependence at all. However, the low field device DIII-D begins to show a $1/B_T$-like dependence at a low field end $B_T(EFIT)/B_T(code)$ >1.6. Thus, it can be concluded that in a conventional range of B and q values, the neoclassical density pedestal width has $1/B_p$-like dependence, without an obvious B_T dependence, on both C-Mod and DIII-D pedestal.

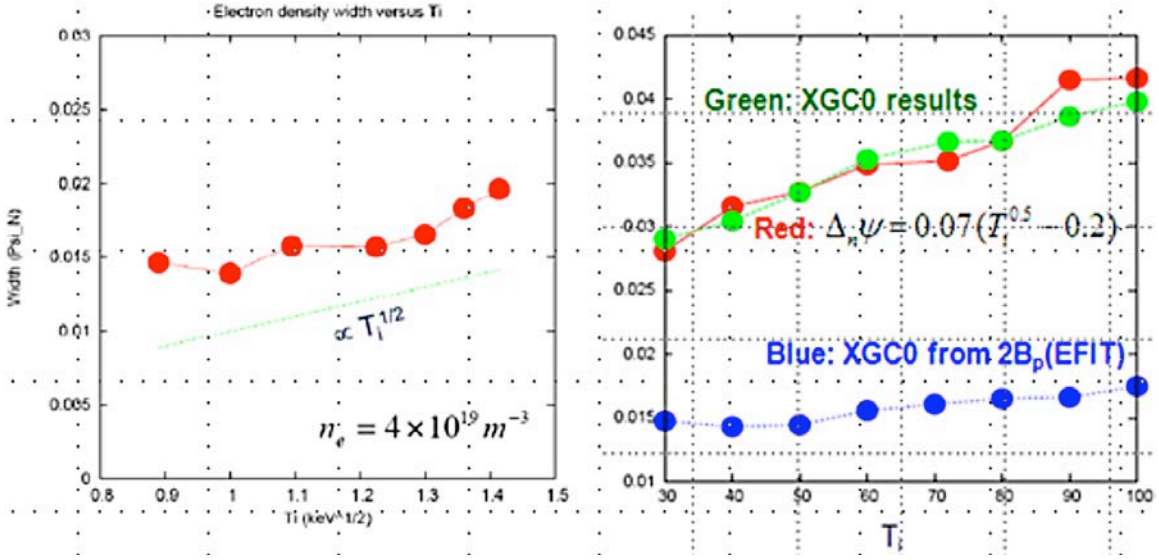

Fig. 6-2. Density pedestal width as function of $T_i^{1/2}$ in keV (left figure for DIII-D) or as function of T_i in eV (right figure for C-Mod). In the right hand side figure, the blue data is with the poloidal magnetic field B_p doubled from the EFIT value.

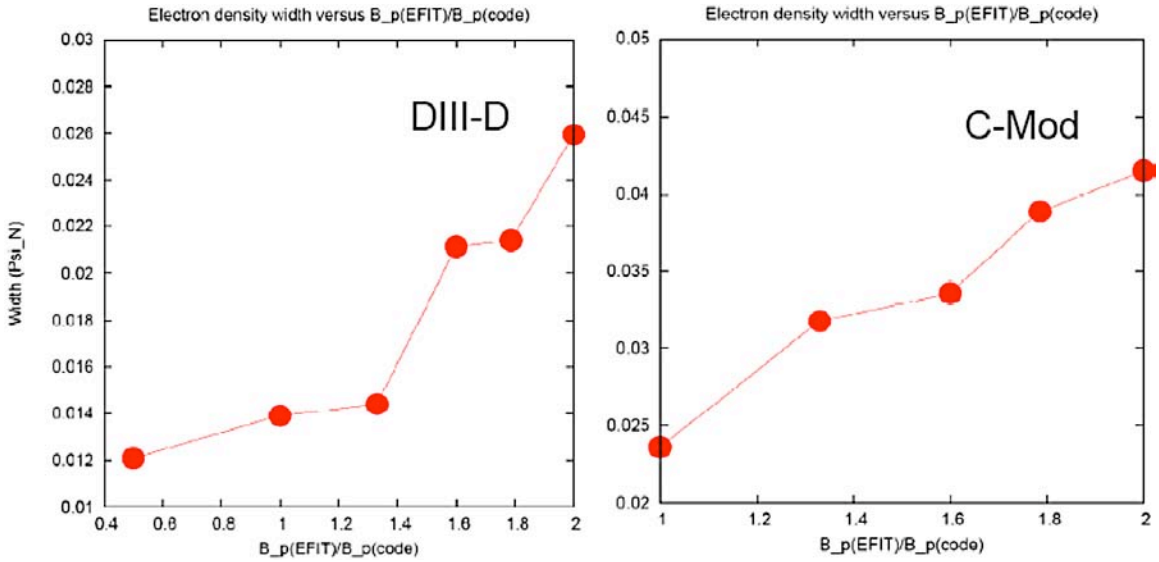

Fig. 6-3. Density pedestal width as function of B_p reduction ratio $B_p(EFIT)/B_p(code)$ for DIII-D (left) and C-Mod (right). Both devices show a $1/B_p$-like dependence.

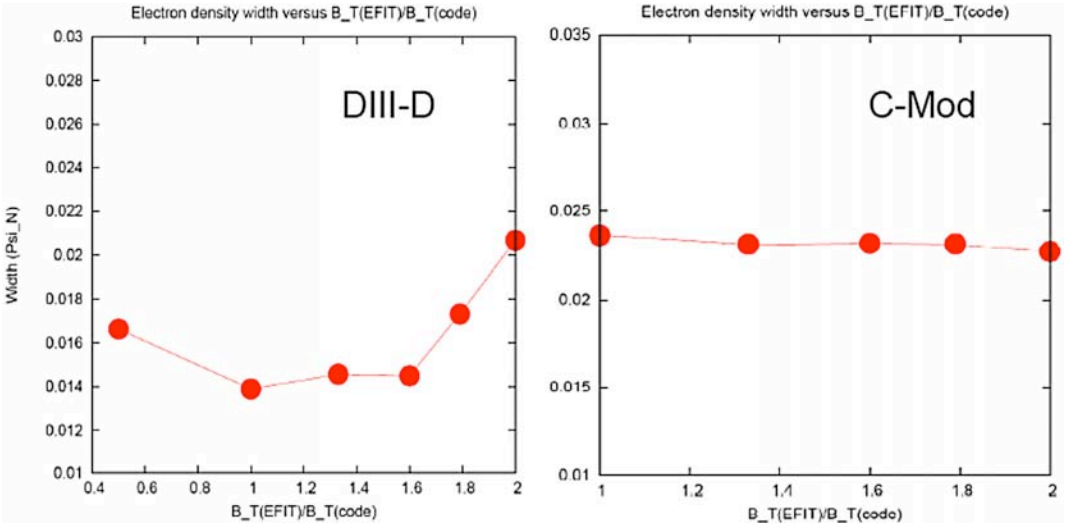

Fig. 6-4. Density pedestal width as function of $1/B_T$. The high field device C-Mod does not show the B_T dependence. The low field device DIII-D begins to show $1/B_T$-like dependence at the low field end $B_T(EFIT)/B_T(code)$ >1.6.

6.2. Difference in the Radial Location of Density Pedestal Between C-Mod and DIII-D

There is an indication that the radial location of edge density pedestal may be somewhat different between DIII-D and C-Mod. This observation could have an important implication to ITER since the edge localized instability physics can be different between the closed and open magnetic field regions, and since the higher density in the scrape-off region can mean less effective plasma fueling. In order to investigate this question, an XGC0 study has been performed between the higher field device C-Mod and the lower field device DIII-D. Plasma values at the pedestal top are imported, in the beginning of simulation, from JRT2011 standard discharge cases provided by each machine (g132014.03000 for DIII-D and g1110201023 for C-Mod). The rest of the edge plasma profiles are then allowed to evolve in XGC0. In C-Mod, the experimental ion temperature at the pedestal top is assumed to be equal to the electron temperature. Figure 6-5 shows comparison of neoclassical pedestal density profiles between DIII-D and C-Mod obtained from XGC0. Anomalous radial diffusion is turned off. It can be seen that the neoclassical electron density pedestal in C-Mod from XGC0 simulation is shifted toward the scrape-off layer, compared to the DIII-D case. Addition of radial anomalous transport did not change this trend, indicating that that the source of this phenomenon is neoclassical. Detailed physical origin of this difference is to be investigated.

6.3. Difference Between the Main and Impurity Ion Rotations in Edge Pedestal

Plasma rotation and its relation to pedestal structure have usually been investigated experimentally using the carbon impurity rotation. However, there is no guarantee that the carbon rotation is similar to the main ion rotation. We have investigated this question using XGC0 in DIII-D and C-Mod geometry in a purely neoclassical mode with neutral recycling rate of 0.99. The standard JRT discharges have been used. Figure 6-6 shows parallel rotation of deuteron and carbon species in the DIII-D (left) and C-Mod (right) edge plasmas, respectively. It can be seen that the carbon rotation profile in DIII-D pedestal is quite different from the deuteron. However, in C-Mod, the carbon rotation profile is found to be similar to the deuteron rotation due to the large collisional momentum exchange between the deuteron and carbons species.

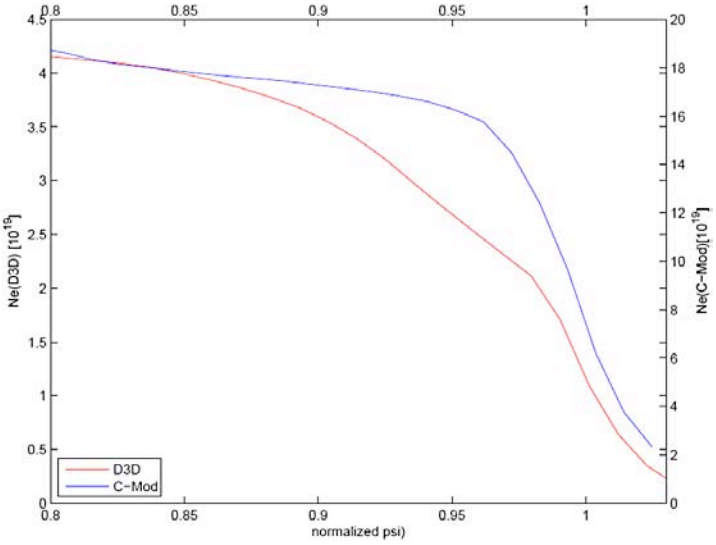

Fig. 6-5. Density pedestal profiles obtained from XGC0, with the neutral wall-recycling coefficients 0.99. Red curve is for DIII-D and the blue curve is for C-Mod.

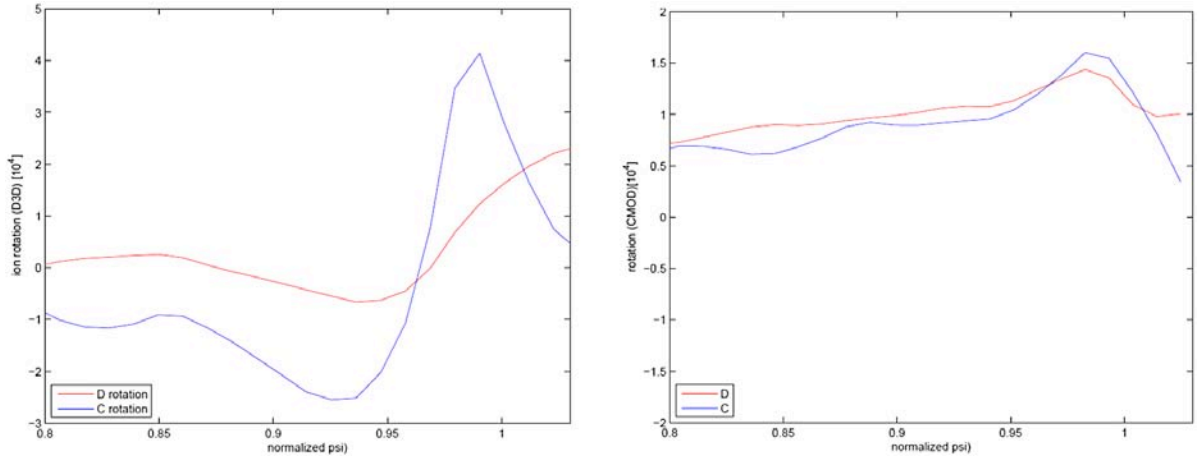

Fig. 6-6. XGC0 simulation results for radial rotation profiles of D^+ and C^{+6} in DIII-D (left) and C-Mod edge.

6.4. Bootstrap Current in the Edge Pedestal

Accurate evaluation of plasma bootstrap current in the steep edge pedestal is important in the physics of edge stability and equilibrium. Questions have been raised on the validity of existing theories and formulas when applied to the edge pedestal region, owing to the assumptions and approximations used in the analytic and numerical developments. In a tokamak edge pedestal, the gradient scale length becomes of the same order as the ion banana width. At the same time, the passing particle region in velocity space becomes smaller, and is no longer well-separated from the trapped-passing boundary layer. Analytic calculations become highly challenging, especially at higher collisionality. Trapped particles drive bootstrap current, but the trapped-passing boundary layer and the passing particle region play important roles in carrying the actual current. The XGC0 first-principles particle code has been used to investigate these important questions. It can be seen from Fig. 6-7 that the existing formulas and XGC0 results are well cross-verified when the edge pedestal is in the electron banana-plateau collisionality regime. This verification is true in both a conventional aspect ratio tokamak (DIII-D or C-Mod) and in a tight aspect

ratio tokamak (NSTX). However, in a collisional pedestal, the existing analytic formula by Sauter predicts about 15-20% higher bootstrap current than the XGC0 simulation results in a conventional aspect ratio tokamak. On the other hand, in a collisional pedestal in a tight aspect ratio tokamak (NSTX), XGC0 shows that the bootstrap current is about 30% higher than the Sauter formula prediction (Fig. 6-8).

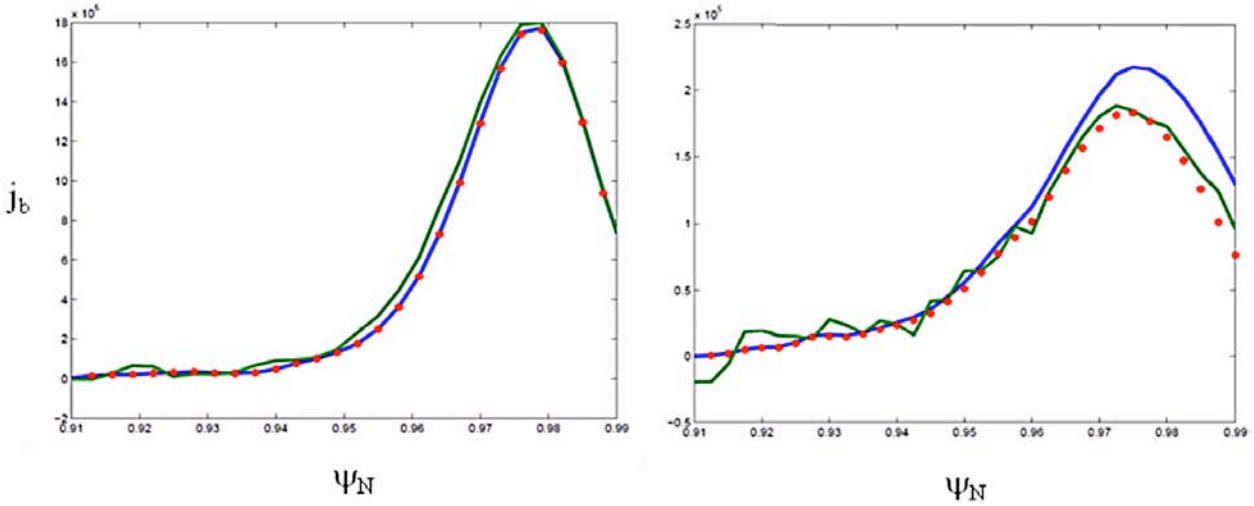

Fig. 6-7. Left: Bootstrap current evaluated from XGC0 when the edge pedestal is in banana-plateau regime of collisionality (green). Sauter formula result is shown in blue, and an improved analytic formula result is shown in red dots. The agreement is surprisingly good. The results shown here are in DIII-D geometry. C-Mod and NSTX shows similarly good agreement. Right: XGC0 evaluated bootstrap currents in collisional DIII-D plasma pedestal (green) is about 15-20% lower than the Sauter formula prediction. C-Mod shows a similar result.

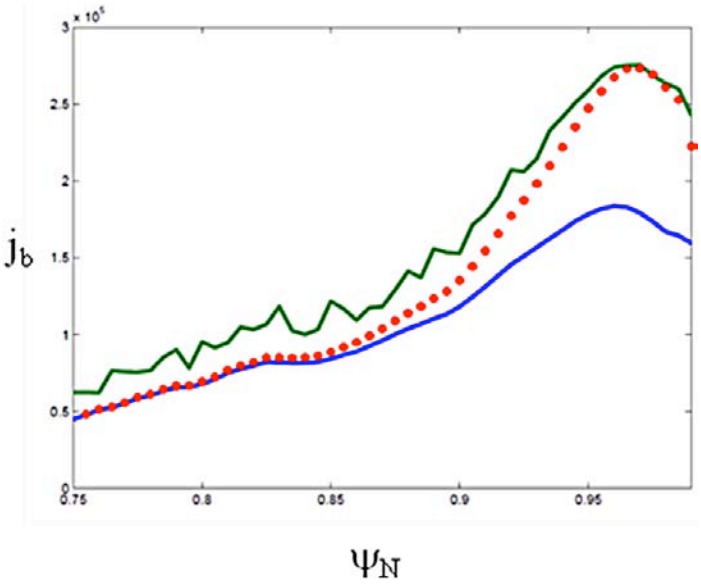

Fig. 6-8. XGC0 results (green) shows that the bootstrap current in a tight aspect ratio collisional tokamak pedestal is about 30% higher than the Sauter formula prediction (blue).

The overall conclusion from this study is that the existing analytic formulas are surprisingly good when the pedestal is in banana-plateau collisionality regime. However, when the pedestal electrons are in the collisional regime, the numerical simulation yields approximately 15-20% lower bootstrap current in a conventional tokamak, and approximately 30% higher bootstrap current in a tight aspect ratio tokamak.

The edge peeling mode may be somewhat more stable in DIII-D and C-Mod, and more unstable in NSTX and MAST compared to the stability analysis based upon the Sauter model bootstrap current formula. A new analytic formula has been developed, as a modification to Sauter formula, which can approximately reproduce the numerical result (red dots in the figures).

6.5. Impurity Effect on Pedestal Structure

Carbon impurity particles are added to the D ions in XGC0 in DIII-D-like plasma. It is found that the impurity particles do not make much difference to the structure of the electron density and Te pedestal. The most noticeable changes are in the broadening of the Ti pedestal and in the reducing the depth of the Er well. We have also noticed that the toroidal rotation of deuterons can be quite different from that of carbon impurities.

6.6. RMP Effect on Pedestal Structure

XGC0 has also been used to study the RMP penetration effect on pedestal structure. With the self-consistent evaluation of the external n=3 component RMP penetration, simulated profiles of pedestal density, temperature, E_r, and the toroidal rotation at 4ms after the RMP turn-on begin to resemble the experimental profiles of shot number 126006 (Fig. 6-9).

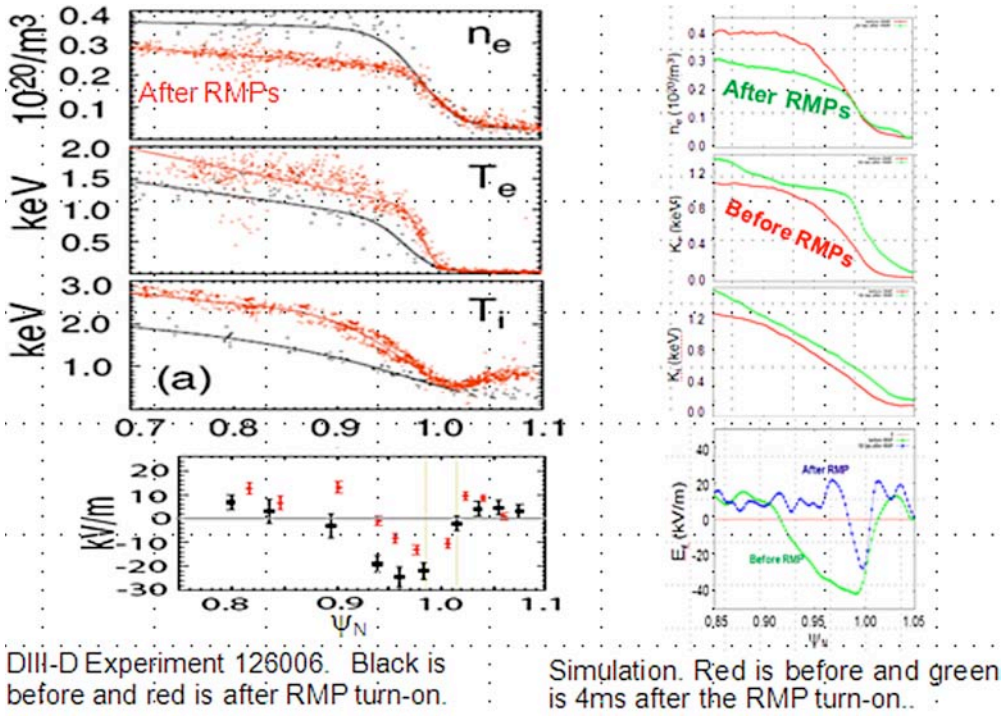

Fig. 6-9. Comparison of the RMP-affected pedestal profiles between experiment (left) and XGC0 kinetic modeling (right). Excellent qualitative agreement can be seen. The RMP penetration is evaluated self-consistently with the pedestal transport.

7. FY11 JRT CONTRIBUTION FROM U. WISCONSIN (J.D. Callen)

The context for transport modeling studies of pedestal structure in FY 2011 was provided by the H-mode Edge Pedestal (HEP) Benchmarking Exercise (BE) group's paper on a comprehensive analysis of plasma transport properties in an H-mode pedestal that was published in mid 2010 (J.D. Callen, R.J. Groebner, T.H. Osborne, J.M. Canik, L.W. Owen, A.Y. Pankin, T. Rafiq, T.D. Rognlien and W.M. Stacey "Analysis of pedestal plasma transport" Nucl. Fusion 50, 064004 (2010)). Two major conclusions from this paper were:

1. A large, inward density pinch is likely operative in the pedestal. Subsequent work this past year has explored:
   a. The temporal development of the pinch between ELMs (W.M. Stacey, Nucl. Fusion 51 (2011) 063024)
   b. FACETS modeling of the pedestal density profile using a pinch-diffusion model. (Pankin, A.Y., et al., "Stress Tests of Transport Models Using FACETS Code" – Submitted for publication to AIP Proceedings for CNR-Chalmers workshop (July 2011, Varenna, Italy)). This work is also discussed in the contribution by A.Y. Pankin to this report.
2. Paleoclassical plasma transport may provide the minimum level of density and energy transport in pedestals. Thus, a comprehensive paleoclassical-based pedestal structure model was developed. In point and some profile shape comparisons, it has been shown to yield predictions that are within about a factor of two of DIII-D experimental data. Two reports have been submitted to journals for publication:
   a. J.D. Callen, J.M. Canik and S.P. Smith, "Pedestal Structure Model", Report UW-CPTC 11-3, July 11, 2011 available via http://www.cptc.wisc.edu (submitted to Physical Review Letters

      In this paper, predictions are developed for the plasma profiles in H-mode pedestals that are in transport quasi-equilibrium in tokamaks. They are based on assuming paleoclassical radial plasma transport processes dominate throughout the pedestal. Model predictions are given for gradients and profiles of the electron density and temperature in the pedestal. The predictions agree quantitatively (within less than a factor of two) with properties of an extensively studied H-mode pedestal and some other recent pedestal experimental results.

      This paper includes comparisons of the model with experimental data from NSTX, discussed in the contribution for NSTX to this report.

   b. J.D. Callen "Model for pedestal structure", Report UW-CPTC 11-4, 11 July 2011 available via http://www.cptc.wisc.edu (submitted to The Physics of Plasmas)

      In this paper, predictions are developed for the structure of plasma parameter profiles of high-confinement (H)-mode pedestals in transport quasi-equilibrium in tokamaks. They are based on assuming paleoclassical radial plasma transport processes dominate throughout the pedestal. The key physical process in this model is that the electron temperature gradient increases to the magnitude required for paleoclassical electron heat transport to carry the large conductive radial electron heat flow from the hot core through the pedestal to the separatrix. The intrinsic level of paleoclassical density transport is typically large in the pedestal compared to local fueling due

to neutral recycling from outside the separatrix. Thus, in this model the electron density profile is determined mainly not by edge fueling but rather by a combination of the density boundary condition at the separatrix and the pedestal density profile needed for the outward paleoclassical diffusive flux to be nearly balanced by the inward paleoclassical pinch flux. Model predictions are given for the electron density and temperature gradients, profiles and magnitudes in the pedestal. Transition into electron-temperature-gradient (ETG) driven anomalous radial electron heat transport in the core plasma is proposed to limit the initial, transport-limited height of the electron pressure pedestal. Characteristics of the ion temperature and plasma toroidal rotation profiles in the pedestal are also predicted. All the model predictions are found to agree quantitatively (within a factor of about two or less) with the properties of an extensively studied H-mode pedestal. Other model comparisons and applications to some outstanding H-mode pedestal structure and evolution issues in tokamaks are also discussed. Finally, a hierarchy of experimental and modeling validation tests are suggested.

c. The paleoclassical-based pedestal structure model predictions for the electron density and temperature gradients and profiles have been compared using an extensive statistical analysis of the pre-2011 DIII-D pedestal database and of the DIII-D pedestal experimental results in the 2011 campaign. This work is discussed in the DIII-D contribution to this report and will be reported by S.P. Smith at the H-Mode Workshop in Oxford. The preliminary conclusion from this analysis is that the paleoclassical model seems to provide the irreducible minimum level of electron density and heat transport. The predicted electron temperature profiles are usually closest to the experimental data; the electron density profiles are often somewhat wider than predicted indicating that some additional density transport may be operative in most pedestals.

8. FY11 JRT CONTRIBUTION FROM ORNL (J.M. Canik)

An experiment in DIII-D to measure the pedestal characteristics at several densities has been modeled using the SOLPS code [8-1], which uses a fluid model for plasma transport (with classical transport parallel to the magnetic field, and user-specified cross-field transport) coupled to a Monte-Carlo neutral transport model. This modeling is constrained by several experimental measurements, and yields a calculation of the pedestal transport coefficients that includes the effects of impurity radiation and neutral fueling, as well as the 2D distribution of neutral sources. Two H-mode discharges have been compared, with pedestal densities that differ by a factor of ~1.7. The 2D modeling indicates that in the higher density discharge, the neutral penetration lengths into the pedestal decrease by ~30%, whereas the pedestal density width increases slightly. These penetration lengths are calculated for various sources of neutrals, with the divertors and main chamber recycling considered separately. The modeling indicates that a large fraction of the neutral flux from main chamber recycling is able to penetrate through the SOL to fuel the pedestal, and that neutrals from this source penetrate farther into the pedestal than neutrals from the divertor. As a result, the total neutral penetration length could show an additional change with density if this source were to dominate in one case. Although the modeling suggests that the main chamber is not the dominant pedestal fueling source in either case, and therefore that the total neutral decay length has the opposite dependence to the pedestal density width, this highlights the need to constrain the modeling with more direct measurements of this possible neutral source.

References for Section 8

[8-1] R. Schneider et al., Contrib. Plasma Phys. **46**, 3 (2006).

9. FY11 JRT CONTRIBUTION FROM Tech-X (A.Y. Pankin)

The paleoclassical density transport model [9-1] is verified using the FACETS code for a set of three DIII-D discharges that represent a plasma current scan [9-2]. The particle source parameters and effective diffusivities that are in addition to the paleoclassical density diffusivity are found by minimizing the rms deviations, which varied from 0.4% to 5.7% for the DIII-D discharges studied in this research. Figure 9-1 shows the experimental and simulated plasma density profiles and the paleoclassical particle fluxes computed with the FACETS code. The convective components of the paleoclassical density flux are found to be larger than the diffusive components of particle fluxes for all three DIII-D discharges. The total paleoclassical fluxes are found negative in the pedestal region. The additional positive diffusive fluxes, which are introduced through the additional anomalous diffusivity D^{add}, are expected to compensate this imbalance. The additional diffusivity D^{add} is found to be about 0.27 m^2/sec for higher plasma current discharges 132014 and 131416 and 0.17 m^2/sec for the lower plasma current discharge 132017. The effective magnetic diffusivity D_η in the pedestal center is found in the range from 0.08 m^2/sec to 0.14 m^2/sec. The level of additional diffusivity is comparable to or exceeds the paleoclassical (magnetic field) diffusivity in the H-mode pedestal region. The hypothesis that the paleoclassical particle transport is a dominant channel of density transport in the H-mode pedestal region of DIII-D discharges requires additional studies. Future directions for this FACETS modeling of pedestal plasma profiles include: most importantly a more precise paleoclassical pinch model using the full parallel neoclassical resistivity, using the improved FACETS solver which will facilitate a more complete paleoclassical transport model including its non-standard electron heat transport model, increased radial resolution, more direct neutral modeling using the FRANTIC code and additional transport models such as MMM71 and TGLF.

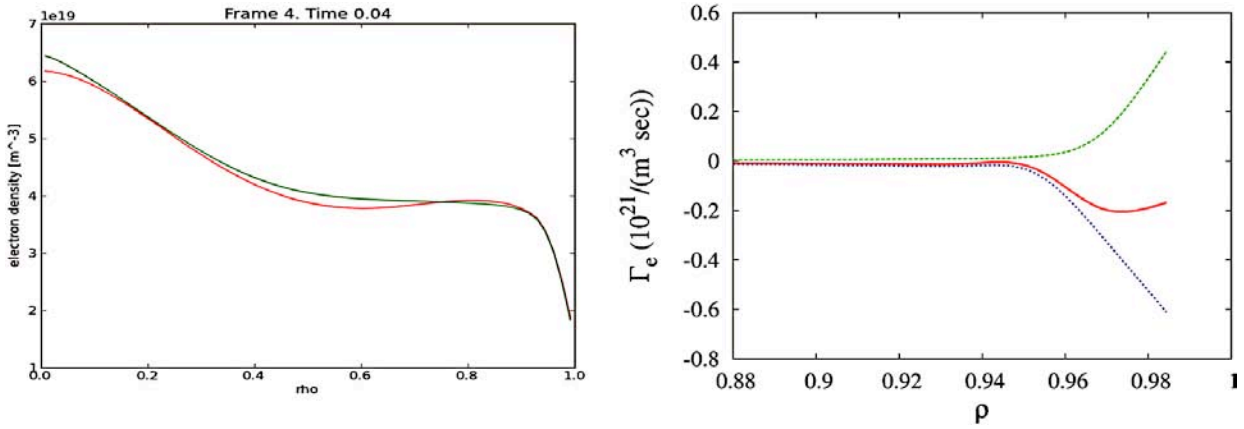

Fig. 9-1. The electron density profile computed with the FACETS code (green solid curve) is compared with the experimental density profile (red solid curve) for the DIII-D discharge 132017 on the left panel. The total electron paleoclassical particle flux (red solid curve), as well as diffusive (green dotted curve) and convective (blue dotted curve) contributions to the paleoclassical particle flux are shown in the right panel.

ETG anomalous thermal transport has been investigated for a set of DIII-D equilibria that were constructed using the equilibrium TOQ code to mimic experimental conditions in a recent DIII-D experiment. The ETG modes that are driven by the electron temperature gradient are typically characterized by the ratio η_e of electron density gradient scale length, L_{ne}, to the electron temperature gradient scale length, L_{te}. Plasma temperature and density profiles and critical parameter η_e for five

different equilibria are shown on Fig. 9-2(a-c). Several reduced models for anomalous transport have been tested in the FACETS code. These models include the Horton-Jenko model, GLF23, and TGLF models. Fig. 9-2(c) shows the effective diffusivities computed with these models for equilibria that have minimum and maximum values of η_e. All models predict that ETG modes are unstable at the top of the H-mode pedestal. The effective diffusivities are found in the range from 1 m^2/sec to 3 m^2/sec for the Horton-Jenko model, from 2.5 m^2/sec to 3 m^2/sec for the GLF23 model, and from approximately 0.3 m^2/sec to 0.5 m^2/sec for the TGLF model. The Horton-Jenko and GLF23 models predict that the ETG modes become unstable at ρ=0.45 and ρ=0.5, while the TGLF model predicts that the ETG modes become unstable at approximately ρ=0.35. The models' stiffness is found rather different as well. The analysis of experimental data and comparison with experimental results will help to discriminate between different reduced models for ETG anomalous thermal transport.

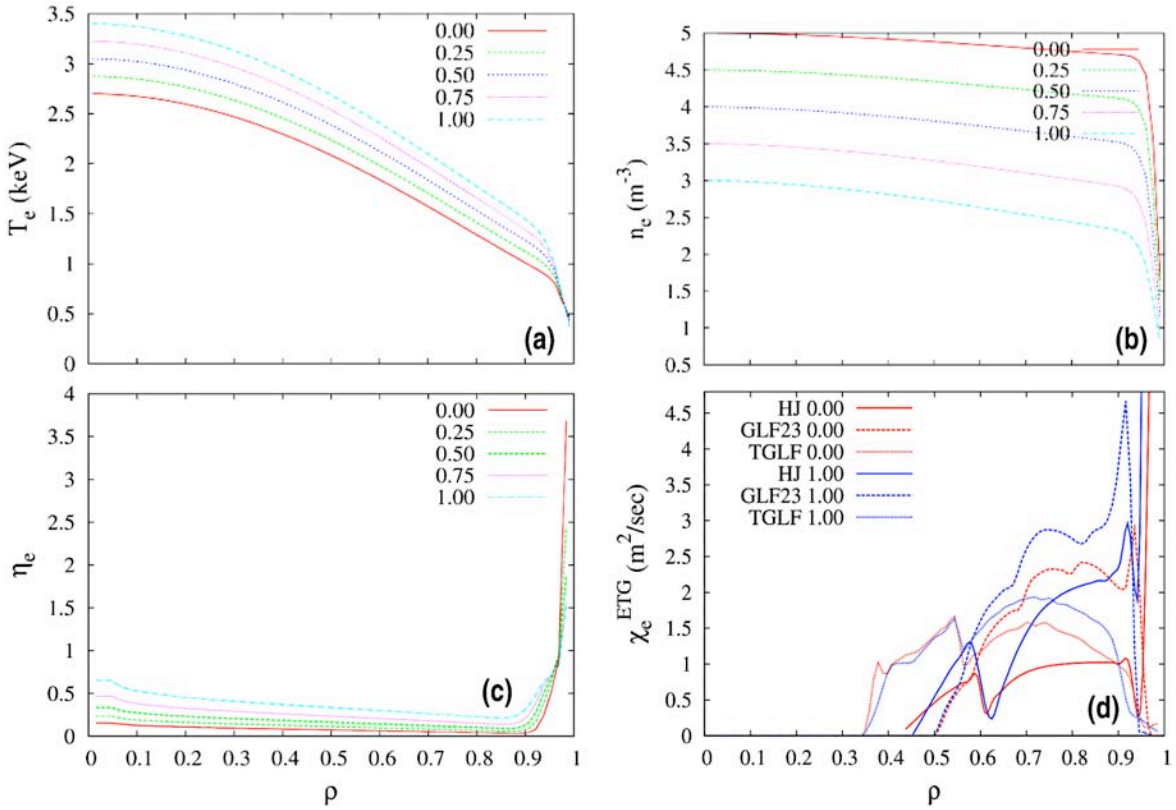

Fig. 9-2. The electron temperature and density profiles are shown on the top two panels. The profiles of critical ETG parameter η_e are shown on the left bottom panel. The effective diffusivities profiles computed with Horton-Jenko (HJ), GLF23, and TGLF models are shown on the right bottom panel. The profiles on the right bottom panel shown in red correspond to the equilibrium with lower values of η_e, while the profiles shown in blue on the right bottom panel correspond to the equilibrium with higher value of η_e.

References for Section 9

[9-1] Callen J.D., Phys. Plasmas **12**, 092512 (2005); J.D. Callen, Nucl. Fusion **45**, 1120 (2005); J.D. Callen et al. Phys. Plasmas **16**, 082504 (2009).

[9-2] Snyder P.B. et al., Phys. Plasmas **16** 056118 (2008); R.J. Groebner et al., Nucl. Fusion **49**, 085037 (2009).

10. FY11 JRT CONTRIBUTION FROM GEORGIA TECH. (W.M. Stacey)

Is the edge pedestal structure determined by the particle, momentum and energy balances and the heat conduction relation?

W. M. Stacey (Georgia Tech), R. J. Groebner (GA) and T. E. Evans (GA)

The possibility that the density, temperature and pressure profiles in the edge pedestal are determined by the first four fluid moments of the Boltzman transport equation, with appropriately determined constitutive relations, has been investigated on DIII-D.

The first moment is the continuity, or particle balance equation for the main ion species "j"

$$\frac{\partial\left(n_j V_{rj}\right)}{\partial r} = -\frac{\partial n_j}{\partial t} + n_e n_o \left\langle \sigma \upsilon \right\rangle_{ion} + S_{nb} \quad , \tag{1}$$

which determines the radial particle flux $\Gamma_j = n_j V_{rj}$, where V_{rj} is the radial ion particle flux, the second term on the right is the ionization of recycling neutrals and the last term is the neutral beam source.

The toroidal and radial components of the second moment, or momentum balance, equation can be combined to obtain an equation that determines the pressure profile

$$-\frac{1}{p_j}\frac{\partial p_j}{\partial r} = \frac{V_{rj} - V_{rj}^{pinch}}{D_j} \quad , \tag{2}$$

where the "diffusion coefficient"

$$\hat{D}_j \equiv \frac{m_j T_j \nu_{jk}}{\left(e_j B_\theta\right)^2}\left(1 + \frac{\nu_{dj}}{\nu_{jk}} - \frac{e_j}{e_k}\right) \quad , \tag{3}$$

and the "pinch velocity"

$$V_{rj}^{pinch} \equiv \frac{\left[-M_{\phi j} - n_j e_j E_\phi^A + n_j m_j \left(\nu_{jk} + \nu_{dj}\right)\left(f_p^{-1} V_{\theta j} + E_r / B_\theta\right) - n_j m_j \nu_{jk} V_{\phi k}\right]}{n_j e_j B_\theta} \quad , \tag{4}$$

is a collection of normalized forces associated with the electric field, $V \times B$ forces and beam momentum input. The quantity ν_{dj} is a toroidal angular momentum transfer frequency which represents the combined effect of viscosity, inertia, atomic physics, and other "anomalous" processes, which can be inferred from experiment. (These equations are written for the main ion species "j" in a two-species plasma with impurity species "k".)

The third moment, or energy balance equations for the main ion and electron species

$$\frac{\partial Q_j}{\partial r} \equiv \frac{\partial}{\partial r}\left(q_j - \frac{3}{2}\Gamma_j T_j\right) = -\frac{\partial}{\partial t}\left(\frac{3}{2} n_j T_j\right) + q_{nbj} - q_{je} - n_e n_o^c \left\langle \sigma \upsilon \right\rangle_{cx} \frac{3}{2}\left(T_j - T_o^c\right) \quad , \tag{5}$$

and

$$\frac{\partial Q_e}{\partial r} \equiv \frac{\partial}{\partial r}\left(q_e - \frac{3}{2}\Gamma_e T_e\right) = -\frac{\partial}{\partial t}\left(\frac{3}{2}n_e T_e\right) + q_{nbe} - q_{je} - n_e n_k L_k\left(T_e\right) \quad , \tag{6}$$

determine the main ion and electron total energy fluxes, $Q_{j,e}$, from which the conductive heat fluxes, $q_{j,e}$, can be determined. The q_{nb} terms represent neutral beam (or other) heating, q_{je} is the ion-to-electron collisional energy transfer, and the last terms in Eqs. (5) and (6) represent charge-exchange cooling of the ions and radiation cooling of the electrons, respectively.

Finally, the heat conduction relations

$$q_{j,e} = -n_{j,e}\,\chi_{j,e}\frac{\partial T_{j,e}}{\partial r} \quad , \tag{7}$$

can be used as a surrogate for the fourth moment, or energy flux, equation to determine the temperature profiles.

If the viscous component of the angular momentum transfer frequencies $\nu_{dj,k}$ and the thermal diffusivities $\chi_{j,e}$ were known, from kinetic theory or fluctuation theory or experiment, it should be possible to solve Eq. (2) for the pressure distribution and Eq. (7) for the temperature distribution, then construct the ion distribution from $n=p/T$. We have investigated this conjecture for a variety of DIII-D shots by using measured rotation velocities, electric fields and other quantities to evaluate the RHS of Eq. (2). Figure 10-1 shows the radial velocity calculated from Eq. (1) and the pinch velocity evaluated from experimental data for an ELMing H-mode discharge that has been much analyzed. When these "velocities" were used to integrate Eq. (2) and the resulting pressure was divided by the experimental ion temperature and then corrected for impurities, the electron density shown in Fig. 10-2 was obtained. The measured electron density profile is shown for comparison.

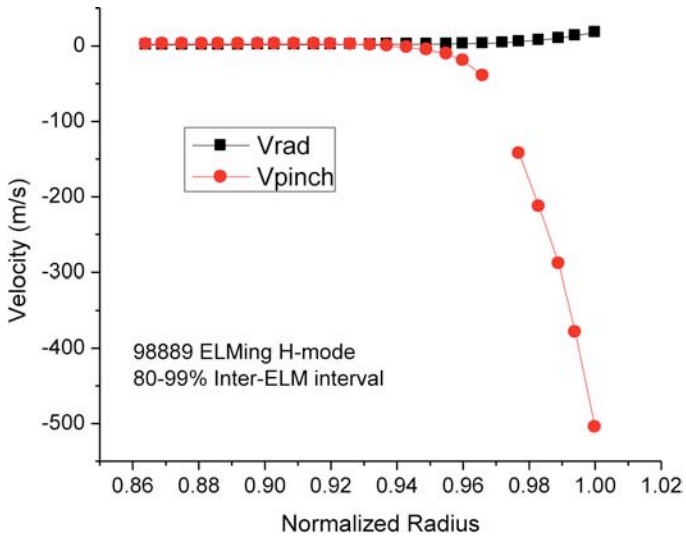

Fig. 10-1. Comparison of the effects of recycling neutrals (V_{rad}) and *VxB* and *Erad* (*Vpinch*) in determining the pressure gradient in the edge pedestal.

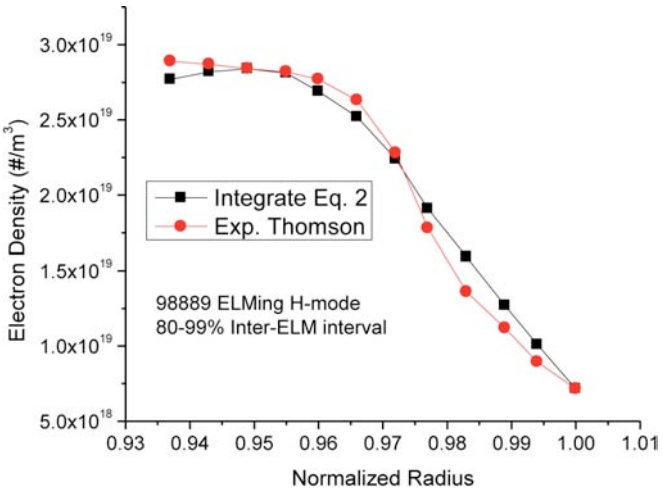

Fig. 10-2. Comparison of measured and calculated ion density profile in edge pedestal.

The effect of the *VxB, Erad* and other "physics" forces on the determination of the pressure profile from Eq. (2) enters through the term V_{rj}^{pinch}, which was evaluated mostly from experimental data. The effect of recycling neutrals on the determination of the pressure profile from Eq. (2) enters through the term V_{rj}, which is evaluated by solving Eq. (1). Thus, comparing these two terms in Fig. 10-1 provides an appreciation of the relative importance of recycling neutrals and *VxB, Erad* and other forces on the determination of the pressure profile. Similar results have been found in other discharges.

This same type of analysis has been applied to understand (in terms of differences in the edge radial electric field rotation velocities and the resulting differences in particle pinch) the differences in density profiles between "matched" H-mode and RMP discharges [10-1], the evolution of density and temperature profiles between ELMs [10-2], and the difference in density and temperature profiles across an L-H transition [10-3].

Recently, it has become evident that the ion particle and energy fluxes calculated from Eqs. (1) and (5) must be corrected for ion orbit loss [10-4] and X-transport [10-5] (outward drift in the vicinity of the X-point).

References for Section 10

[10-1] Stacey W.M. and T.E. Evans, Nucl. Fusion **51**, 013007 (2011).

[10-2] Stacey W.M. and R.J. Groebner, Nucl. Fusion **51**, 063024 (2011).

[10-3] Stacey W.M. and R.J. Groebner, Phys. Plasmas **17**, 112512 (2010).

[10-4] Stacey W.M., "The effect of ion orbit loss on the interpretation of ion energy and particle transport in the DIII-D edge plasma," Phys. Plasmas (Sept. 2011).

[10-5] Stacey W.M. "X-transport of ions in diverted tokamaks, with application to DIII-D," Phys. Plasmas (submitted).

11. FY11 JRT CONTRIBUTION FROM U. COLORADO (W. Wan and S. Parker)

The Summary of GEM Results

In flux tube simulations we have found the dominant instability at r/a=0.94, near the pedestal top, is ITG. As we scan across the minor radius, the linear growth rate is higher into the steep gradient region, around r/a=0.975. At 0.975 the dominant instability is driven by density gradient and electron temperature gradient, and the growth rate is higher with higher k_θ. The real frequency there is positive, meaning the wave propagating in the electron direction, for smaller k_θ, while it becomes negative for larger k_θ. In simulations with Er, however, the real frequency is positive for all k_θ due to a Doppler shift.

12. FY11 JRT CONTRIBUTION FROM UC IRVINE (D. Fulton and Z. Lin)

EM GK Pedestal Summary – GTC

The first step in beginning gyrokinetic pedestal simulations of DIIID shot 131997_3011 was to obtain magnetic equilibrium and plasma profile in a usable form. Using mex2eqs (Alex Pletzer, PPPL), EFIT g files were converted to GTC-usable magnetic spline information (including B, toroidal and poloidal flux values, q profiles, minor radius, etc.). The plasma profiles (n, T) were obtained from p files using an in house Matlab script, which resamples the profiles so data points are even spaced in poloidal flux (psi). Gradients are recalculated and splined inside GTC. Density, temperature, and q-profiles were compared to GYRO output, and found to be in agreement.

In order to avoid numerical instabilities, initial simulations were carried out as flux tube runs off of the peak gradient region, at psi=0.945. GTC has no default flux tube mode, so flux tube style profiles were created manually. This was done by calculating the values of the gradient (1/f * df/dr for quantity f) at the psi location, and then producing profiles with a constant value of that gradient. This was done for both density and temperature profiles. The magnetic equilibrium and q-profiles are left unchanged. The simulations were linear and electrostatic, and the flux tube extends from psi=0.7 to psi=1.0.

In order to identify/find dominant instabilities, the first run included all n and m modes, finding a peak in the poloidal spectrum around m=38-42. Based on a q-value of 2.5 in the middle of the fluxtube region, we chose n=16 for subsequent filtered runs.

The latest run includes only n=16, but still contains all m-modes. The poloidal spectrum shows, m=41 as the dominant poloidal mode. The measured growth rate of this mode is 2.2x10^5 1/s and the real frequency is 5.36x10^5 rad/s. See Fig. 12-1 for growth of the n=16, m=41 mode.

Based on the poloidal mode structure (Fig. 12-1) the mode extends from major radius of 123 to 220 cm, giving minor radius of 48.5 cm. An m value of 41 would then correspond to $k_\theta \sim 0.845$ 1/cm.

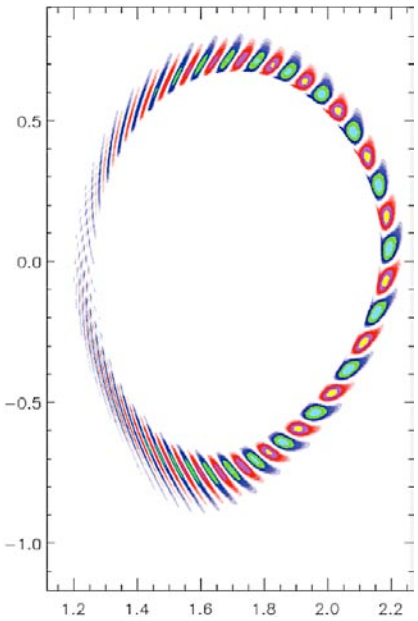

Fig. 12-1. The poloidal mode structure calculated from GTC code with n=16 and m=41.